Methods for Detection of Small Molecule-Protein Interactions

by

Yan Guan

A Dissertation Presented in Partial Fulfillment
of the Requirements for the Degree
Doctor of Philosophy

Approved August 2015 by the
Graduate Supervisory Committee:

Nongjian Tao, Chair
Joshua LaBaer
Michael Goryll
Shaopeng Wang

ARIZONA STATE UNIVERSITY

December 2015

ABSTRACT

Detection of molecular interactions is critical for understanding many biological processes, for detecting disease biomarkers, and for screening drug candidates. Fluorescence-based approach can be problematic, especially when applied to the detection of small molecules. Various label-free techniques, such as surface plasmon resonance technique are sensitive to mass, making it extremely challenging to detect small molecules. In this thesis, novel detection methods for molecular interactions are described.

First, a simple detection paradigm based on reflectance interferometry is developed. This method is simple, low cost and can be easily applied for protein array detection.

Second, a label-free charge sensitive optical detection (CSOD) technique is developed for detecting of both large and small molecules. The technique is based on that most molecules relevant to biomedical research and applications are charged or partially charged. An optical fiber is dipped into the well of a microplate. It detects the surface charge of the fiber, which does not decrease with the size (mass) of the molecule, making it particularly attractive for studying small molecules.

Third, a method for mechanically amplification detection of molecular interactions (MADMI) is developed. It provides quantitative analysis of small molecules interaction with membrane proteins in intact cells. The interactions are monitored by detecting a mechanical deformation in the membrane induced by the molecular interactions. With this novel method small molecules and membrane proteins interaction in the intact cells can be detected. This new paradigm provides mechanical amplification of small interaction signals, allowing us to measure the binding kinetics of both large and small molecules with

membrane proteins, and to analyze heterogeneous nature of the binding kinetics between different cells, and different regions of a single cell.

Last, by tracking the cell membrane edge deformation, binding caused downstream event – granule secretory has been measured. This method focuses on the plasma membrane change when granules fuse with the cell. The fusion of granules increases the plasma membrane area and thus the cell edge expands. The expansion is localized at the vesicle release location. Granule size was calculated based on measured edge expansion. The membrane deformation due to the granule release is real-time monitored by this method.

DEDICATION

To my beloved parents and grandparents for nurturing and their selfless support.

ACKNOWLEDGEMENTS

I would like to give special thanks to my advisor, Dr. Nongjian Tao, for his ongoing guidance, encouragement and support. I've learnt not only how to become an excellent researcher but also how to be an extraordinary person from him.

Also, I have received a great deal of tutelage from Drs. Xiaonan Shan, Shaopeng Wang, Kyle Foley, Wei Wang, Erica Forzoni on different projects. Thank them for discussing with me on the projects, and showing me how to solve problems. They have led me step by step to become an independent engineer and scientist.

It has been a great time to work in Dr. Tao's group with so many excellent people. Group members always tried their best to help me. I enjoyed working with all the group members. I would like to explicitly thank Drs. Francis Tsow, Hui Yu, Xianwei Liu, Yixian Wang, Linliang Yin, Rui Wang, Lihua Zhang, Shaoyin Guo and Christopher MacGriff, as well as Mr. Yunze Yang, Ms. Fenni Zhang, Mr. Karan Syal, Mr. Zixuan Chen, Mr. Limin Xiang, Ms. Yueqi Li, Ms. Yue Deng. I will always remember the time working with you.

Finally, I would like to thank all my committee members for their valuable time and advices: Drs. Michael Goryll, Joshua LaBaer, Shaopeng Wang and Lina Karam.

TABLE OF CONTENTS

Page

CHAPTER Page

CHAPTER Page

LIST OF TABLES

Table Page

LIST OF FIGURES

Figure Page

Figure Page

Figure Page

Figure Page

CHAPTER 1

INTRODUCTION AND BACKGROUND

1.1 Introduction

Small molecules play an important role in biological system, as they have a variety of biological functions, serving as cell signaling molecules, as drugs in medicine and etc. Protein-protein interactions have a key role in biological functions and thus provide chances for small molecule drugs modulating the protein-protein interaction as a therapeutic intervention to treat the disease [1, 2]. Small molecules are the most popular form of drugs. According to US FDA's Orange Book (for primarily small-molecule drugs) and the Center for Biologics Evaluation and Research (CBER) website (for biological drugs), among the 1,357 unique drugs, 1204 are 'small-molecule drugs' which account for about 88%, and only 166 are 'biological' drugs [3]. The number of newly approved 'small-molecule drugs' every year also exceeds the 'biological' drugs. Accurate, efficient evaluation of biomolecular interactions is critical in the drug screening and development. Screening for a drug is likened to searching for a needle in a haystack [4]. Nowadays it is taking, on average, 13.5 years to discover a drug from target identification to approval [5]. From this point, in order to shorten the drug discovery time and reduce cost, instrumentation advances and experimental design improvement are necessary.

The receptor theory of drug action posits that a drug works only when it binds to its target receptor [6]. To study this binding process, usually binding affinity and kinetics are employed. Binding affinity, quantified by equilibrium dissociation constant K_D, measures the extent to which a drug is bound to its receptor at equilibrium. Binding affinity could not quantify the rates at which a drug associates with or dissociates from its receptor, which

directly impact drug efficacy and safety. The rates are the binding kinetics. Obviously, it is important to directly measure the binding kinetics of a drug and its receptor in order to optimize drug efficacy [7].

To date, the most widely used technology uses labels, such as radio- or enzymatic- or fluorescent-labeling to report the binding of a ligand to its receptor. While popular and useful, the labeling step requires additional time and cost, and even worse, labeled approach can be problematic, especially when applied to the detection of small molecules, because the dye molecules can significantly alter the activities of small molecules, leading to inaccurate conclusions [8]. Various label-free techniques, such as surface plasmon resonance technique and micro- and nanomechanical biosensors have been developed, but their sensitivities diminish with the size of the molecule, making it extremely challenging to detect small molecules.

In this chapter, first detailed binding kinetics is discussed. Second current small molecule detection methods are briefly reviewed.

1.2 Binding Kinetics

Binding kinetics which is quantified by association rate constant (k_{on}), dissociation rate constant (k_{off}) describes how fast a ligand binds to its receptor and how quickly it dissociates from its receptor. Consider a simple binding reaction between a ligand (L) and its receptor (R) to form a biomolecular complex (LR):

$$L + R \underset{k_{off}}{\overset{k_{on}}{\rightleftharpoons}} LR \tag{1.1}$$

This reaction comprises a single elementary step - the binding (or unbinding) of drug without any intermediate states which is the first order binding kinetics.

The binding affinity is described by the dissociation constant, K_D, a ratio of the relevant concentrations at equilibrium:

$$K_D = \frac{[L][R]}{[LR]}. \tag{1.2}$$

At equilibrium, the ligand concentration at which half of the receptor binding sites are occupied is equivalent to K_D(both in unit of moles per liter). K_D is directly related to the free energy difference, ΔG_d, between the bound and unbound states [6]. By measuring the ratio of the three concentrations of ligand, receptor and the formed complex, the equilibrium dissociation constant can be determined. The stronger the molecular binding, the smaller the dissociation constant. K_D is mostly used quantification of non-covalent binding. However, some information is missing to have an overall picture of molecular interaction if we only depend on measuring K_D, because it is the ratio of two rates given as:

$$K_D = \frac{k_{off}}{k_{on}}, \tag{1.3}$$

where k_{on} and k_{off} are the association rate constant and dissociation rate constant respectively.

To understand the importance of measuring binding kinetics in order to comprehensively study a molecular interaction, let's consider two drugs (L_1 and L_2) binding to the same receptor (R) with the same equilibrium dissociation constant K_D. We could not assess which drug is better in terms of efficacy and safety if we solely measure K_D. It is possible that both on- and off-rates are slow for L_1, while that are fast for L_2. Notably, changes in k_{off} can result in no measurable effect on K_D if there is compensatory changes in k_{on}. The average time that a ligand stays bound to its receptor, the residence time, $t_R \equiv 1/k_{off}$. We lose at least the information that how long the ligands keep bound

to the receptors if we only measure K_D while the residence time is important in affecting the efficacy of drugs [7].

1.3 State of the Art

Currently most used assay methods are reviewed in this part. The methods fall into two catalogs: labeled and label-free methods. Labeled methods, including enzyme linked immunosorbent assay (ELISA), radioimmunoassay and etc. require some fluorescent labeling, radiolabeling or enzyme linking to report the ligand and receptor binding. The labeled detection strategy arises a lot issues. First, the labeling step makes the detection take more time and work. Second, the labeled tag may intervene with the interaction between ligand and receptor which leads to false negatives. Third, the hydrophobic fluorophores may have strong nonspecific adsorption on the background which causes false positive results. However, the labeled detection, i.e. fluorescence based detection or ELISA, is principally used in the high-throughput screening 'hits'. It is mainly because these methods have high sensitivity (for example, ELISA has a sensitivity in the range of pM in antibody-antigen detection) and are easy to be operated parallel by automated robot system.

In contrast, in label-free detection, target molecules are not labeled or affected and are detected in their natural forms. This detection method allows for not only affinity measurement as fluorescence-based detection, but also real-time quantitative and kinetic measurement of molecular interaction. As discussed in section 1.2, binding kinetics is indispensable when we comprehensively study a reaction. There are many label-free approaches, including surface plasmon resonance (SPR) biosensors that translate mass into refractive index, microcantilevers that transduce biomolecular interactions into mechanical

bending, and silicon nanowire field effect transistors that measure intrinsic biomolecular charge. SPR and mechanical biosensors will be reviewed in section 1.3.2 and 1.3.3.

1.3.1 Enzyme Linked Immunosorbent Assay (ELISA)

Enzyme labels in immunoassay was invited in the 1960s with the reporter label to be enzyme rather than radioactivity [9]. Nowadays ELISA is a gold standard for protein study. There are different strategies used in ELISA: direct, indirect, sandwich and competitive/inhibition ELISA (Figure 1.1). The direct ELISA uses an enzyme labeled primary antibody directly binding to the antigen for detection. Detected antigen can be non-covalently adsorbed on the substrate or captured by the capture antibody immobilized on the assay plate. However the direct ELISA is not widely used though it requires less procedures. The reasons are multifold. First, primary antibodies may be adversely affected by the labeled enzymes. Second, labeling primary antibody for each detected antigen is time and cost consuming. Indirect ELISA uses an enzyme labeling secondary antibody to generate signal while primary antibody for the binding. In the indirect assay, the immunoreactivity of the primary antibody is retained because it is not labeled. And sensitivity is increased because each primary antibody contains several epitopes that can be bound by the labeled secondary antibody, allowing for signal amplification. However, extra incubation and washing steps are required. Sandwich assays—the biomolecule to be detected is sandwiched between the surface bound capture antibody and detecting antibody followed by enzyme linked secondary antibody—is mostly used in the protein detection. The sandwich assay provides high specificity in detection because the capture assay format excludes many nonspecific adsorbed proteins on the substrate. With a first antibody that has 1 nM affinity, an ELISA assay can detect proteins within a few pM concentration range

[10]. The advantages of ELISA are obvious that ELISA has high sensitivity and selectivity which can be used to detect proteins in physiological fluid like serum, blood. Simplicity to be automated makes ELISA well suitable in the HTS application.

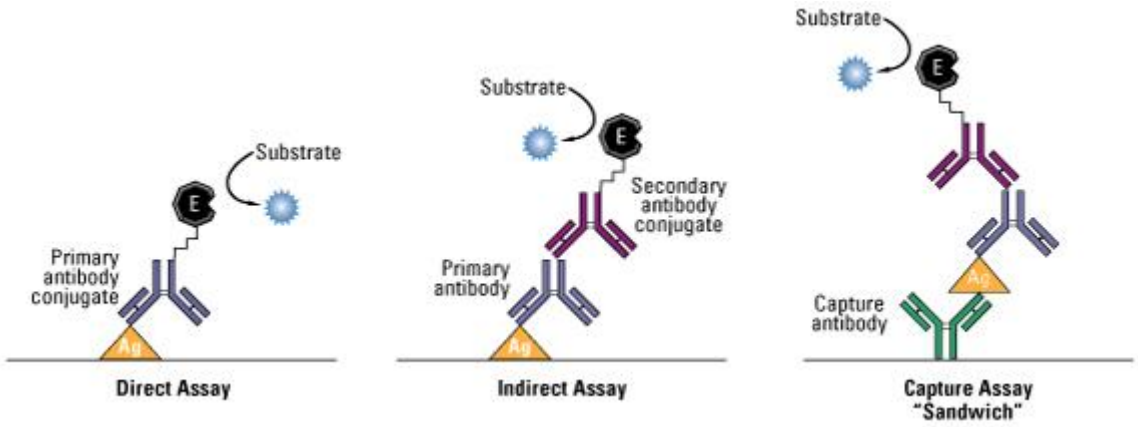

Figure 1. 1 Common ELISA formats. The antigen of interest is directly adsorbed on the assay plate or captured by the immobilized capture antibody. The antigen is detected by enzyme linked primary antibody (direct assay) or a matched set of unlabeled primary and conjugate secondary antibodies (indirect assay). [From Thermo Scientific at http://www.piercenet.com]

However, the limitations of ELISA are multifold. First, the secondary antibody detection makes ELISA usually take a few hours. The washing between every steps increases the repetitive labor. Second, as a labeled method, ELISA is an endpoint detection assay which is hard to get the binding kinetics. Third, for the study of interaction between small molecules and protein, the direct detection is difficult mainly because the small size limits the secondary antibody selection. Usually two antibodies binding to one antigen can be found while hard for a small molecule. Also it is not feasible to link an enzyme to small molecules for direct ELISA. Not mentioning the difficulty in chemical conjugation, the big enzyme will greatly affect the interaction between the small molecule and the protein which

gives inaccurate information. In the study of low molecular weight inhibitor of protein-protein interaction, ELISA is used in the competitive/ inhibition assay. Chen et al. reported several active compounds were identified inhibiting MDM2-p53 binding in an ELISA assay with IC_{50} of 10 to 20 μM [11].

1.3.2 Surface Plasmon Resonance

Surface plasmon resonance (SPR) biosensor nowadays is prevalent in label-free detection. SPR biosensors detect the binding molecules induced refractive index change within around 200nm range above the sensor surface. Neither target nor biorecognition molecules need to be labeled. SPR biosensor plays an important role in high content screening because it can offer real-time monitoring of molecular interaction and accurate kinetics of biomolecules binding. The study of small molecules with carbonic anhydrase II that compared SPR with the traditional measurement of stopped-flow fluorescence and isothermal titration showed that the kinetic parameters determined by SPR are in agreement with those solution-based measurement [12].

Most of the SPR sensors developed to date use Kretschmann configuration to generate surface plasmon resonance [13] (Figure 1.2). A p-polarized light is incident upon a metal film through a prism. When the incident angle reaches resonant angle, the surface plasmons, which are collective oscillations of free electrons in a metallic film, are excited. The reflective light intensity goes to minimum because the excited surface plasma adsorb the incident light energy. The resonance angle is highly dependent on the refractive index of the medium near the metal film. When binding happens, the bound molecules change the refractive index which gives a resonance angle shift. By measuring angle shift, the binding events can be detected. Another measurement strategy is to fix the incident light angle, and

measure the reflective light intensity. According to the light intensity change, the molecular interaction can be monitored.

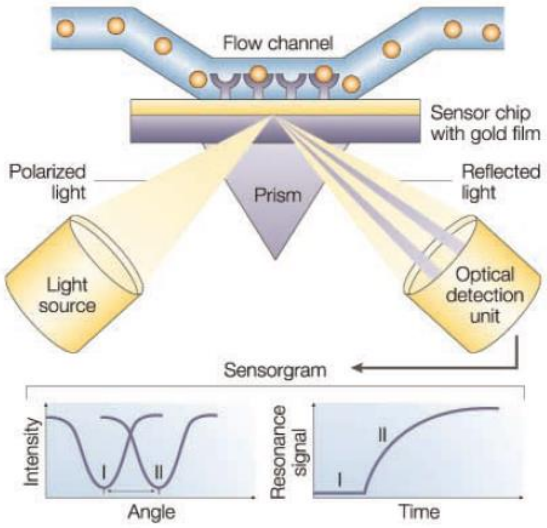

Figure 1. 2 Kretschmann configuration. A p-polarized light is incident on the metal film through a prism. The reflected beam is collected and analyzed [14]. When binding event happens, the resonant angle shifts (i.e. from I to II).

The commercialized SPR sensors, taking the instrument from Biacore (http://www.biacore.com) as an example, are typically based on prism coupling and have a detection limit between 1×10^{-6} to 1×10^{-7} RIU and a mass surface density detection limit around 1 pg/mm^2 [15].By using a bi-cell photodetector, the detection limit is improved an order of magnitude, i.e. 1×10^{-8} RIU [16]. With the improvement of experimental design, instruments and data processing, SPR-based biosensor can be used for routinely studying the direct binding of small molecules (<500 Daltons) to macromolecular targets [17, 18]. Drug screening by SPR also has been explored [19]. However, because of its limited throughput, SPR has been mainly used for focus-deck screening or secondary confirmation screening [20]. A small library of 47 compounds against a cellular prion protein generated

6 hits that have shown activity in a cell-based assay [21]. SPR has been applied to fragment-based drug design (FBDD), a novel strategy. Fragment-based screening involves the selection, screening, and optimization of fragments. In FBDD, diverse set of very small, less complex compounds (molecular weight < 300) is tested by affinity-based methods. Perspicace et al. applied SPR technology to screen a library of 2226 molecules (fragments having low molecular weight between 100 and 300 Da) for binding to chymase, a serine protease. And 80 compounds showed up as positive screening hits [22]. The results demonstrated that the application of SPR technology as a filter in fragment screening can be achieved successfully.

One major challenge for applying SPR technology to small-molecule drug discovery is the limit of detection. The change of refractive index depends on the mass change. When scaling down, it is hard to detect very low molecular weight molecules. Sometimes refractive index change is also due to conformational change of protein when binding to compounds. It can be used as another useful approach for small molecule detection, while it may not be broadly applied to a wide range of targets.

1.3.3 Mechanical Biosensors

Advances in micro- and nonafabrication technologies are enabling a wide range of new technologies, including fabricating a micro- or nanosized mechanical moving part. Generally, mechanical biosensors take advantage of the development of nanofabrication that the physical size of the mechanical part scales down to micro- or nano-range. First, the detection limit of added mass is proportional to the total mass of the device. Nanoelectromechanical system (NEMS) have achieved zeptogram-scale mass resolution when operating in vacuum [23], and nanogram resolution when operating in a fluid

environment [24]. Second, the mechanical compliance of a device – its ability to be displaced or deformed – greatly increases with uniform reduction of its dimensions. Third, with the scaling down of device size, the fluidic mechanical devices can exhibit fast response time. This allows the biological reactions to be observed more detailed with high time-resolution.

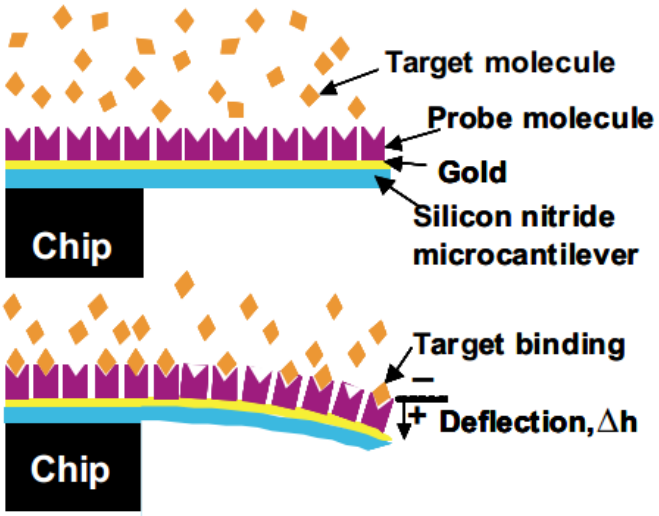

Figure 1.3 Surface-stress mechanical biosensors. Binding of target molecules generates surface stress, which makes the microcantilever deflect [25].

Surface-stress Mechanical Biosensors

In the mechanical biosensors, a small cantilever is usually a central part which is sensitive to the biomolecules of interest. Surface-stress mechanical biosensors measure the quasistatic deflection of a cantilever, caused by the biomolecules binding to the surface immobilized functional groups (Figure 1.3). When binding happens, surface stress is developed – owing to electrostatic attraction or repulsion, steric interactions, hydration and entropic effects. And the stress causes deflection of the mechanical element which can be measured by reflecting a laser beam off the cantilever. It has been reported the study of

DNA hybridization [26], binding of mRNA [27], and drug interaction [28] by measuring the surface stress change with cantilever. Reported sensitivities range from ~100 pM to few nM range. The limitation of this method is it cannot offer real-time information because what measures is the surface stress induced quasistatic deformation of the cantilever.

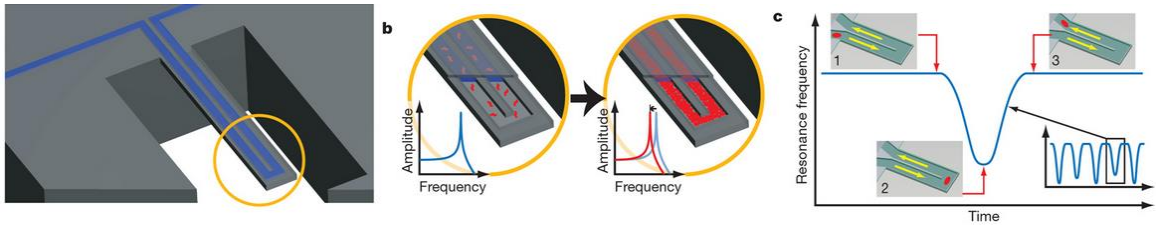

Figure 1.4 Illustration of two mass measurement modes enabled by a fluidfilled microcantilever. a, A suspended microcantilever transduces mass change to resonant frequency shift. Fluid continuous flows through the cantilever and transport biomolecules, cells, and nanoparticles passing through the channel. By scaling down the wall and fluid layer thickness to micrometer size and packaging it in the high vacuum, the microcantilever attained mass sensitivity of sub-fetomgram. b, While bound and unbound molecules both increase the mass of the channel, species that bind to the channel wall accumulate inside the device, and, as a result, their number can greatly exceed the number of free molecules in solution. This can be used for the real-time monitoring specific capture events happening in the channel. c, In another measurement mode, cells or nanoparticles are flowing through the channel without any binding to the surface, the observed signal is dependent on the position of cells or particles along the channel (insets 1-3). The cells or nanoparticles mass can be measured by the resonant frequency shift [29].

Dynamic-mode Mechanical Biosensors

These devices are not measuring the quasistatic deflection. They are oscillating with a resonant frequency and when the biomolecules of interest target on the cantilever, the resonant frequency shifts. Continuous operation allows continuous monitoring and fast detection molecular interaction. With the dynamic-mode mechanical biosensors immersed in the fluid, the detection limit goes to picomolar and the response time is a few minutes. Since it is a mass change based frequency shift method, the concentration sensitivity highly depends on analyte molecular weight. Subpicomolar sensitivity of detection bacterial virus T5 (molecular weight = 7×10^7 Da) was reported [24].For smaller peptides like ferrichrome (molecular weight = 687.7 Da), the sensitivity is typically micromolar. When the system has a high quality factor, Q, it is very sensitive in the frequency-shift based mass detection. However, for the continuous monitoring, the cantilever is immersed in the fluid, the quality factor, Q is susceptible to the fluid such as the damping which diminishes the Q and results in the sensitivity decreasing. A very clever way to solve the sensitivity deterioration is to embed the microfluid channels with the mechanical cantilever rather than immersing the whole mechanical sensor in the fluid. Burg et al. fabricated such suspension microchannel resonators (SMRs) (Figure 1.4) with 15,000 quality factor to measure single cells and single nanoparticles in the fluid [29].

CHAPTER 2

MEASURE KINETICS OF MOLECULAR INTERACTION BY REFLECTANCE INTERFEROMETRY

2.1 Introduction

Molecular interactions play a crucial and complicated role in biological systems. As a living biological system, all the components are interacting with each other via molecular interactions, and physiological function and disease progression are also relied on molecular interactions. To study these interactions is important for understanding biological activities, discovering biomarkers, and screening drugs. A lot of efforts have been made to study and measure these interactions. The further understandings on biomolecular interactions increases the need for high-throughput, sensitive, fast, and economic way to study them.

Graphene with several nanometers and even sub-nm thickness was imaged by optical microscope [30]. And based on this interference method, different thickness of graphite layers can be distinguished [31, 32]. This straightforward optical method can be applied to the biological study for detecting molecular interactions. The bound molecule changes the optical path length which results in interference phase change. Silicon is widely used in semiconductor industry and is easy to manufacture and process. The silicon based biosensor for molecular interaction is low cost.

In this chapter, the first part is to describe the biosensor, which is based on the fact that bound molecule increases the optical pathway and therefore shifts the interference phase as well as changes the reflectance. Second part is the real-time detection of IgG and anti-IgG interaction by this method. By fitting the data with the first order kinetics, the

association rate constant (k_{on}), dissociation rate constant (k_{off}), and dissociation constant (K_D) were found to be $k_{on} = 1.43 \times 10^4\ M^{-1}s^{-1}$, $k_{off} = 1.47 \times 10^{-3}\ s^{-1}$ and $K_D = 95.8\ nM$. These results are in good agreement with those obtained with plasmonic method. Last part is the improvement in image quality by pixel-to-pixel correction for the future microarray application.

2.2 Principle of Reflectance Interferometry Based Biosensor

The detection method is based on reflectance interferometry. Briefly, the optical path change introduced by the bound protein was measured. A 300 nm SiO_2 layer on top of silicon was used as the sensor surface. The binding process was monitored by a webcam with R, G, and B three channels.

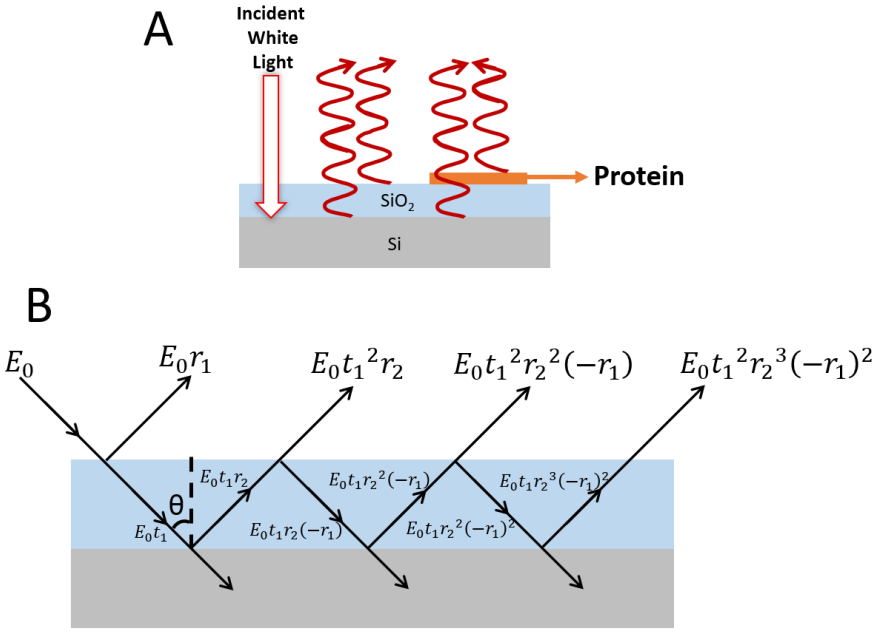

Figure 2. 1 Principle of the reflectance interferometry based biosensor. (A) The surface is vertically illuminated with white light, and the reflected light is imaged by a webcam. The additional height of the surface will change the optical path difference between the top surface and buried oxide-silicon surface which will change the reflected light. (B) Paths of

light rays in multiple reflection between two surfaces – top surface and buried oxide-silicon surface.

Figure 2.1A shows the geometry we used in the experiment. Let r be the coefficient of reflection and t the transmission coefficient. Then provided there is no absorption in protein, silicon dioxide and silicon, the amplitudes of the successive internally reflected rays are $E_0t_1, E_0t_1r_2, E_0t_1r_2(-r_1), E_0t_1{r_2}^2(-r_1), E_0t_1{r_2}^2(-r_1)^2, E_0t_1{r_2}^3(-r_1)^2, \ldots$, as indicated in Figure 2.1B, where E_0 is the amplitude of the primary ray, t_1, r_1, r_2 are the transmission coefficient at air/solution-SiO_2 interface, reflection coefficient at air/solution-SiO_2 interface and SiO_2-Si interface respectively. Consequently, the sequence $E_0r_1, E_0{t_1}^2r_2,\ E_0{t_1}^2{r_2}^2(-r_1),\ E_0{t_1}^2{r_2}^3(-r_1)^2,\ \ldots$, represents the amplitudes of the reflected rays. It is obviously shown that the geometric path difference between two adjacent rays coming out from top surface is

$$\Delta = 2d\ cos\theta \tag{2.1}$$

where d is the thickness of SiO_2 layer and θ is the angle between any two internally reflected ray and the surface normal as indicated in Figure 2.1B. The phase difference between any two successive rays is given by

$$\emptyset = 2kd\ cos\theta = \frac{4\pi}{\lambda_0} n_1 d\ cos\theta \tag{2.2}$$

where n_1 is the refractive index of SiO_2, λ_0 is the vacuum wavelength. Taking the phase difference into account as a factor $e^{-i\emptyset}$ and summing the amplitude of the rays coming out from top surface, we obtain

$$E_r = E_0r_1 + E_0{t_1}^2r_2e^{-i\emptyset} + E_0{t_1}^2{r_2}^2(-r_1)e^{-i2\emptyset} + E_0{t_1}^2{r_2}^3(-r_1)^2e^{-i3\emptyset} + \cdots \tag{2.3}$$

$$E_r = E_0 r_1 + E_0 {t_1}^2 r_2 e^{-i\emptyset} + E_0 {t_1}^2 r_2 e^{-i\emptyset}\left(-r_1 r_2 e^{-i\emptyset}\right) + E_0 {t_1}^2 r_2 e^{-i\emptyset}\left(-r_1 r_2 e^{-i\emptyset}\right)^2 + \cdots \tag{2.4}$$

This is a geometric series with ratio $-r_1 r_2 e^{-i\emptyset}$, and thus

$$\frac{E_r}{E_0} = r_1 + \frac{{t_1}^2 r_2 e^{-i\emptyset}}{1+r_1 r_2 e^{-i\emptyset}} = \frac{r_1+\left({r_1}^2+{t_1}^2\right) r_2 e^{-i\emptyset}}{1+r_1 r_2 e^{-i\emptyset}} = \frac{r_1+r_2 e^{-i\emptyset}}{1+r_1 r_2 e^{-i\emptyset}} \tag{2.5}$$

with ${r_1}^2 + {t_1}^2 = 1$, provided SiO_2 is lossless dielectric media. The reflectivity is then given by

$$R = \frac{I_r}{I_0} = |r|^2 = r r^* \tag{2.6}$$

and thus for the geometry used in the experiment,

$$R = \frac{\left(r_1+r_2 e^{-i\emptyset}\right)\left(r_1+r_2 e^{i\emptyset}\right)}{\left(1+r_1 r_2 e^{-i\emptyset}\right)\left(1+r_1 r_2 e^{i\emptyset}\right)} = \frac{{r_1}^2+{r_2}^2+2 r_1 r_2 \cos\emptyset}{1+{r_1}^2 {r_2}^2+2 r_1 r_2 \cos\emptyset}. \tag{2.7}$$

The angle (θ) and the polarization dependence of the Fresnel reflection coefficients vanish for perpendicularly incident light ($\theta = 0^\circ$), hence r_1, r_2 and $\emptyset$ are given by

$$r_1 = \frac{n_0 - n_1}{n_0 + n_1} \tag{2.8}$$

$$r_2 = \frac{n_1 - n_2}{n_1 + n_2} \tag{2.9}$$

$$\emptyset = \frac{4\pi}{\lambda_0} n_1 d \tag{2.10}$$

where n_0, n_1, n_2 are the refractive index of air/solution, SiO_2 and silicon respectively.

According to Eqs. (2.7) to (2.10), the reflectance depends on the thickness of SiO_2. To simplify the situation, we assume the protein accumulating on the surface have the same refractive index with SiO_2, therefore, the binding of another protein is accompanied by the change of SiO_2 thickness which results in the reflectance change.

2.3 Detection of Anti-IgG and IgG Interaction Based on Reflectance Interferometry

2.3.1 Surface Modification and Channel Preparation

A silicon wafer with 300 nm thick SiO_2 was used as the sensor surface. The silicon wafer was first cleaned with piranha solution (a mixture of 3:1 concentrated sulfuric acid to 30% hydrogen peroxide solution) and then dried with nitrogen. The cleaned silicon wafer was modified with amine group by soaking it into 50 mM 3-Aminopropyletriethoxysilane (APTES) in toluene for 30 min. The silicon wafer was rinsed with toluene and acetone in succession and then dried with nitrogen. Amine modified wafer was stored in desiccator filled with nitrogen for use.

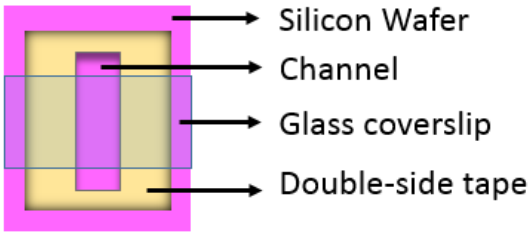

Figure 2.2 Schematic drawing of the double-side tape formed flow channel.

A flow channel was created by the double-side tape. A slot with 3 mm in width and 1 cm in length was cut by blade on the double-side tape as the flow channel. The double-side tape was attached to the silicon wafer on one side and a glass coverslip was covered on the other side (Figure 2.2). The total volume of the channel can be controlled very small as the thickness of the double-side tape is only 50 μm. Solution flew over the channel due to capillary action. A piece of paper napkin positioned at one end of the channel to suck the solution with solution added at the other end of the channel made switch between different solutions.

After modifying and making the channel, the wafer was positioned on an upright microscope (Olympus BX60) with a 4X objective and perpendicularly illuminated with a white light from top. The reflected light was imaged and recorded by the webcam with the frame rate of 15 fps.

2.3.2 IgG Online Modification

To demonstrate molecular interaction detection capability with the present method, we studied the binding of anti-human IgG with human IgG (To simplify, in the later content, IgG and anti-IgG mean human IgG and anti-human IgG if not mention specifically). The silicon wafer was modified with amine group and a flow channel was formed as described above. IgG was on-line modified on the silicon wafer and monitored by this method (Figure 2.3). First the channel was filled with 1X PBS buffer and then solution was switched to 100 μg/ml IgG (in 1X PBS) with 50 mg/ml bis(sulfosucinimidyl)suberate (BS^3). Upon the switch, the intensity in R component decreased rapidly (blue block in Figure 2.3 B). After 1X PBS was changed back, the intensity still remained the same, which showed the IgG was modified on the silicon wafer surface. IgG and BS^3 was in 1X PBS buffer with 5% DMSO. In order to confirm the decrease in intensity was not due to the refractive index change introduced by DMSO, we switched 1X PBS to 5% DMSO in 1X PBS (gray block in Figure 2.3B). There was only small increase in intensity which excluded the possibility that the decrease in intensity was due to refractive index difference between two solutions.

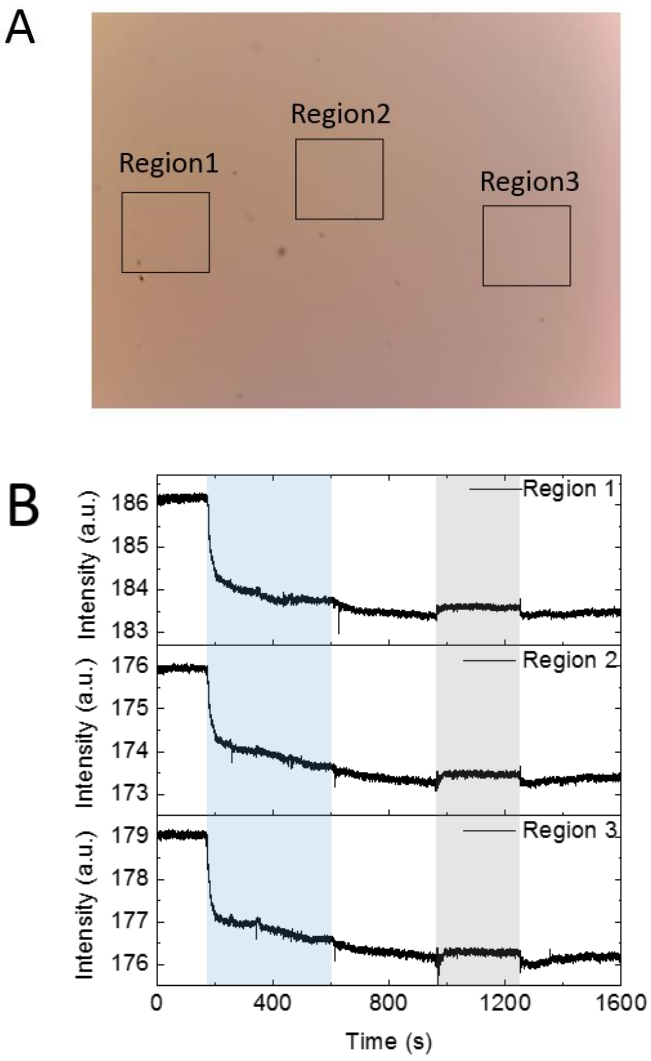

Figure 2.3 Online modification of IgG on surface. (A) One snapshot of channel taken by webcam. Three black boxes marked the regions for the intensity plot in (B). Intensity of R component in three different regions within the channel was plotted. (B) 1X PBS was flowing initially and then was switched to 100 μg/ml IgG with 50 mg/ml BS^3 (blue block). Intensity in R component decreased because of IgG binding on the surface. The solution was switched back to 1X PBS at 600 s (white block). The intensity stayed the same which suggested IgG was covalently bound on the surface. 5% DMSO in 1X PBS was flowing to exclude the possibility that the decrease in intensity was due to refractive index change

introduced by DMSO (gray block). A sudden increase when 5% DMSO was flowing over the surface which was due to the refractive index change. When the solution was changed back to 1X PBS, the intensity went back to stable.

2.3.3 Anti-IgG and IgG Interaction

After IgG was modified on the sensor surface, 1X PBS buffer was switched to 100 μg/ml anti-IgG. Figure 2.4A shows upon the switch, the intensity in R component decreased in the association phase and then stayed stable. When the solution was changed back to 1X PBS, the intensity went back a little due to the dissociation process. The surface was then regenerated by 10 mM HCl. After regeneration, 100 μg/ml BSA was flowing over the surface as a negative control to confirm the signal was due to the specific interaction between anti-IgG and IgG. No obvious change in intensity was observed when the solution was changed to BSA. The regeneration by 10 mM HCl was followed by the negative control. 100 μg/ml anti-IgG was flowing over the regenerated sensor surface for the second time. Similar amount of decreasing in intensity of R component was shown in the association phase and some anti-IgG dissociated from the surface when solution was changed to 1X PBS. The similar responses of the anti-IgG and IgG interaction before and after regenerating of sensor surface demonstrated that the regeneration did work and also the response was due to the specific binding between anti-IgG and IgG interaction. Figure 2.4B shows the experimental data (black dots) and fitted result with first order kinetics (red line) of anti-IgG and IgG interaction. From the fitting, the association rate constant (k_{on}), dissociation rate constant (k_{off}), and dissociation constant (K_D) were found to be $k_{on} = 1.43 \times 10^4\ M^{-1}s^{-1}$, $k_{off} = 1.47 \times 10^{-3}\ s^{-1}$ and $K_D = 95.8\ nM$. These results are in good agreement of that measured by plasmonic method [33].

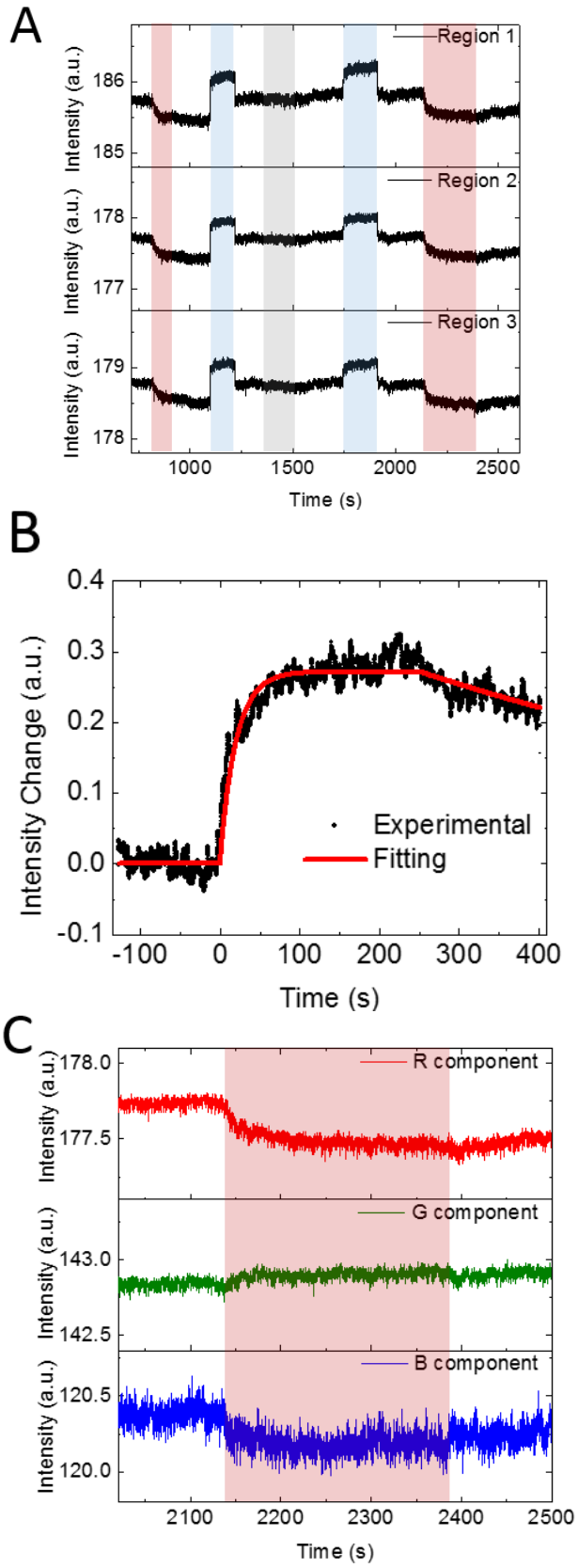
A
Region 1
Region 2
Region 3
Intensity (a.u.)
186
185
178
177
179
178
1000
1500
2000
2500
Time (s)
B
Intensity Change (a.u.)
0.4
0.3
0.2
0.1
0.0
-0.1
-100
0
100
200
300
400
Time (s)
Experimental
Fitting
C
R component
G component
B component
Intensity (a.u.)
178.0
177.5
143.0
142.5
120.5
120.0
2100
2200
2300
2400
2500
Time (s)

Figure 2.4 Anti-IgG and IgG interactions. (A) The intensity plots of R component within three regions marked in Figure 2.3A. During the time marked by red blocks, 100 μg/ml anti-IgG was flowing over the surface. 1X PBS was flowing over the surface within the time marked by white blocks. And the surface was regenerated by 10 mM HCl in the periods of time marked by blue blocks. (B) Sensorgram of anti-IgG and IgG interaction. The experimental data (black dots) was fitted with first order kinetics (red line). From the fitting, the association rate constant (k_{on}), dissociation rate constant (k_{off}), and dissociation constant (K_D) were found to be $k_{on} = 1.43 \times 10^4\ M^{-1}s^{-1}$, $k_{off} = 1.47 \times 10^{-3}\ s^{-1}$ and $K_D = 95.8\ nM$. These results are in good agreement of that measured by plasmonic method [33]. (C) Intensity of R, G and B components within region 2 marked in Figure 2.3A when anti-IgG interacted with IgG. Red block marks the time period when 100 μg/ml anti-IgG flew over the surface. White blocks represent the time block during which 1X PBS was flowing.

The intensity changes of R, G and B components for the anti-IgG and IgG interaction are shown in Figure 2.4C. R component shows obvious signal of anti-IgG and IgG association and dissociation, while no detectable changes is shown in G component and only smaller signal shown in B component compared to R component. Also for the B component, the signal noise ratio is obviously smaller than that of R component. Red light is more sensitive to protein thickness change by reflectance interferometry.

2.4 Image Correction for Protein Spot Recognition

Imagers are increasingly widely used in modern sciences and technologies. Images or a sequence of images (e.g. videos) also gain much broader scopes because of the growing importance of scientific visualization, which provides direct perception and high content

of big data. A variety of fields, including DNA microarray in genomics [34], super-resolution microscopy [35], single nanoparticle catalytic reactions mapping [36] and etc., are all relied on the imagers. The noise level of the imager highly affects the interpretation of scientific data. In 2-D images, the artifacts caused by variations in the pixel-to-pixel light sensitivity and the dark currents of the imager distort or blur the original patterns, which makes the pattern recognition difficult and detection unreliable. A technique called flat-field correction was invented to compensate the different pixel sensitivities and dark current in the detector [37]. Seibert *et al.* constructed a flat-field image by acquiring multiple images under a uniform illumination over a range of incident exposures [38]. In order to extend the application of reflectance interferometry to high-throughput detection, microarray should be employed. And in order to achieve this goal, we first need to clearly recognize protein arrays. Here we use similar flat-field correction method to obtain a reliable and accurate flat-field correction on both CCD camera and webcam. After correction, the unfavorable pattern due to the artifacts were removed and the intensity variation in space was also reduced by at least two times. The protein spot was clearly recognized.

2.4.1 Calibration Method and Result

The calibration is based on the fact that the imager is a linear system to the incident exposures within the dynamic range. The variable pixel gains and dark currents of the camera are corrected at the same time, pixel by pixel. A number of images were taken under uniform illumination over different incident intensities (Figure 2.5B). The exposure time of the camera was set the same. The acquired images show uneven intensity over the view due to pixel-to-pixel variations in sensitivity and dark current. The average intensity

over the whole image was set as the "real intensity" for certain incident intensity. For each pixel, the measured intensity is linearly proportional to the "real intensity" as the camera is a linear digital system (Figure 2.5C). And thus by linearly fitting the measured intensity in the function of "real intensity", the fitting parameters, slope k and intercept b are obtained, which corresponds to the sensitivity and dark current for certain pixel respectively. The relation is shown as

$$I_{ij}^{M} = k_{ij} I^{R} + b_{ij}, \tag{2.11}$$

where I_{ij}^{M}, k_{ij}, and b_{ij} are the measured intensity, slope and intercept for the pixel in i^{th} row j^{th} column respectively and I^{R} is the "real intensity" for certain illumination. By doing the linear fitting for each pixel, the sensitivity correction matrix K and dark current correction matrix B are obtained. For a given raw image (I^{raw})which is taken with the same camera exposure time as that of uniform illumination image, the corrected image ($I^{correct}$) is obtained by

$$I^{correct} = (I^{raw} - B)/K, \tag{2.12}$$

where B and K are the dark current and sensitivity correction matrices respectively. Comparing to the conventional flat-field correction method which only acquires one flat field image and one dark image [37], this method suppresses random noises by taking multiple images and statistic fitting.

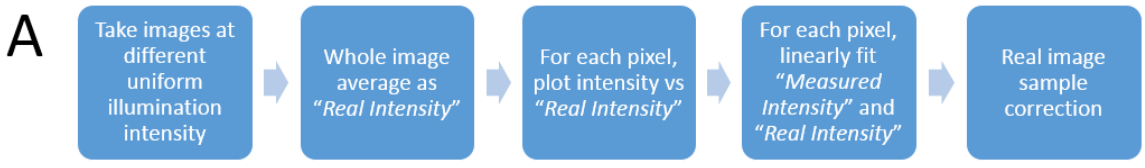

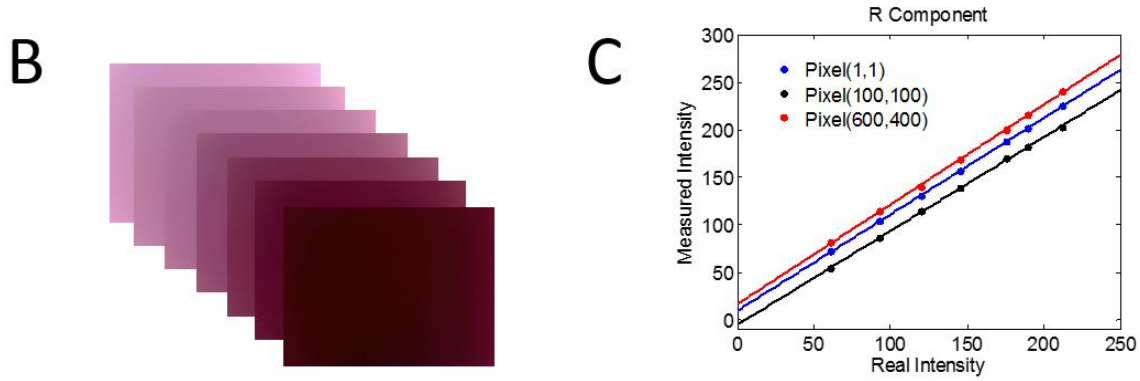

Figure 2.5 Procedure of calibration method. (A) Flow diagram shows the calibration method. (B) A sequence of images with different illumination intensities. (C) The relation between measured intensity and "real intensity" of R component for different pixels.

2.4.2 Image Correction with Protein Spot

To demonstrate the feasibility of the correction method, a clean silicon wafer with 300 nm SiO_2 was imaged by a webcam under an upright microscope with a 4X objective. The illumination light intensity was adjusted and seven images were obtained at different incident light intensities for obtaining the correction matrices (Figure 2.5B). Figure 2.5C plots the measured intensity of three different pixels vs the real intensity which is the average intensity of the whole image. It is shown a good linear relation between the measured intensity and the real intensity. The slope and intercept which represent the sensitivity and dark current respectively were obtained by the linear fitting. The sensitivity and dark current correction matrices were formed by repeating the fitting pixel by pixel (Figure 2.6). The sensitivity of each pixels are similar with only ± 6% variations (Figure 2.6A), while the dark current of each pixels varies a lot (Figure 2.6B). Figure 2.6 also shows that there is similarity in the pattern of sensitivity map and that of offset map,

however two patterns are not completely overlapped. The sensitivity and dark current are not necessarily correlated.

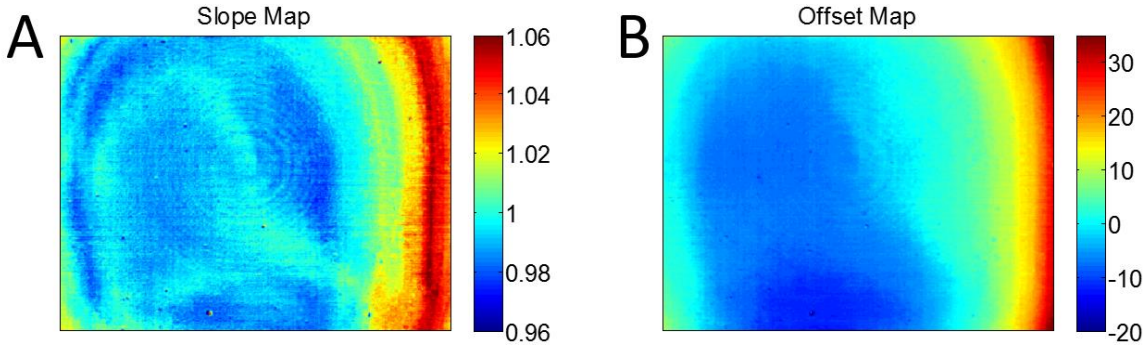

Figure 2.6 Slope map (A) and offset map (B) obtained by the method described above for the sequence of images in Figure 2.5B.

A drop of 1 mg/ml BSA solution (in 1X PBS) with 50 mg/ml bis(sulfosucinimidyl)suberate (BS^3) was dripped on the amine modified silicon wafer (modification see section 2.3.1) for 10 min. The silicon wafer was rinsed with DI water with water flowing from one direction. Then the silicon wafer was dried with nitrogen and imaged with an upright microscope (Olympus BX60) with a 4X objective. The red component of the raw image is shown in Figure 2.7A. The artificial pattern which shows dimmer in center while brighter at the edge makes the protein droplet difficult to recognize. After correcting the red component of the raw image by the correction matrices according to Eq. (2.12), very clear boundary between the silicon wafer background and protein droplet is shown in Figure 2.7D. Figure 2.7D also shows obvious difference between the silicon wafer (left) and the protein droplet (right). An extra layer of protein layer on top of silicon wafer reduces the reflection of red light because of the additional optical path length according to Eq. (2.7). Figures 2.7 B and E show the intensity along the black lines in Figures 2.7 A and D respectively. The global variation was removed and the intensity

difference between the silicon wafer and protein layer is larger after correction. Figures 2.7 C and F are the zoom in plots of the red portions in Figure 2.7 B and E respectively. The standard deviation over the 70 pixels in Figure 2.7C was 0.482 while it was only 0.232 in Figure 2.7E. The variation in pixel-to-pixel intensity was also reduced at least 2 times by the flat-field correction.

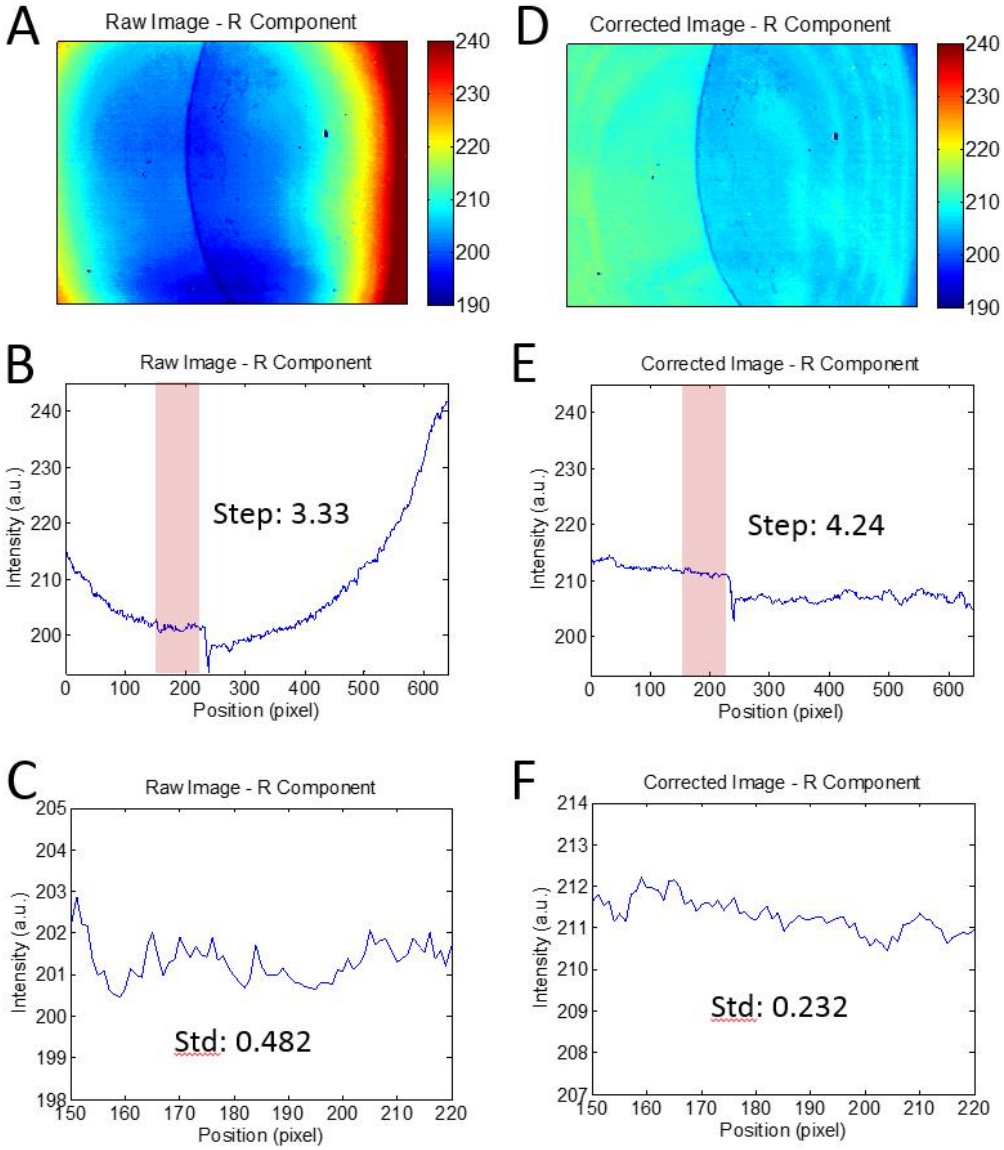

Figure 2.7 Results of calibrated webcam image with protein on silicon wafer. (A) R component of raw image. (B) Intensity plot along the black line in (A). (C) Zoom in of the

region marked by red block in B. (D) Calibrated image of (A). (E) Intensity plot along the black line in (D). (F) Zoom in of the region marked by red block in (E).

To demonstrate that the correction matrices are stable, a raw image (Figure 2.8A) was taken 2 hours after taking the uniform illumination images. Using the correction matrices obtained 2 hours ago, the corrected image (Figure 2.8B) shows similar quality compared to Figure 2.7D.

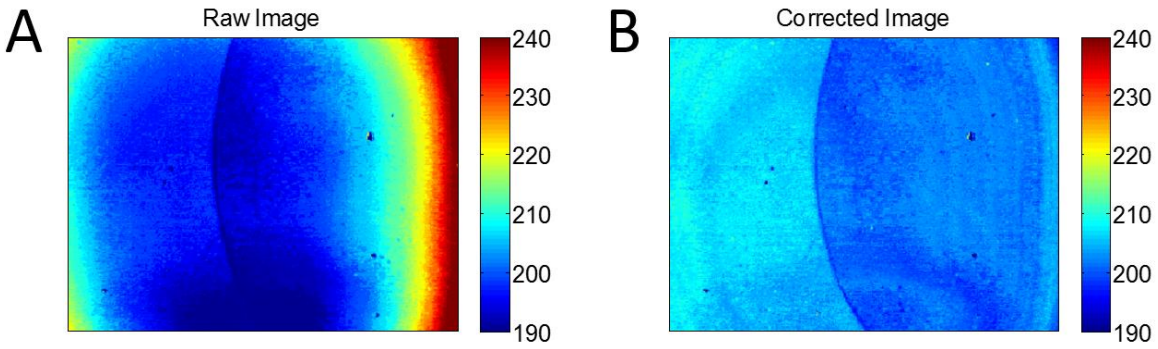

Figure 2.8 Result of calibrated webcam image which was taken 2 hours after taking the uniform illumination images. (A) R component of the raw image. (B) Calibrated image of raw image in (A).

This flat-field correction method can also be used for CMOS research camera. A CMOS research camera (Pike Guppy) was used to take image of a clean silicon wafer under the upright microscope with a 4X objective. The black dots in Figure 2.9A came from the dirt in the optical path or on the camera. Figure 2.9A also shows non-uniformity in intensity that center is brighter than the corners. After correction, all these artifacts were removed and the image became very uniform (Figure 2.9B). Figure 2.9C shows the intensity plots (red lines) along the white lines in Figures 2.9 A and B. the intensity of pixel-pixel variation was reduced by 30 times after correction compared to the raw image (black line in Figure

2.9 C). With the same correction matrices, a raw image of silicon wafer half covered with protein layer was taken by the CMOS camera (Figure 2.9D). The ghost dots were still in the image because of the same camera and optical path. It is obvious that after correction, the image became more uniform and the difference between silicon wafer and the part with protein layer was more pronounced. This CMOS camera is monochromic and the silicon wafer was illuminated by the white light. A layer of protein on the silicon wafer generally reduced the reflection of white light. The line profiles in Figure 2.9F clearly show the big improvement in pixel-pixel intensity variation as well as overall non-uniformity reducing due to the correction. A pronounced step in intensity at the boundary between silicon background and protein layer is shown in the line profile after flat-field correction (red line in Figure 2.9E).

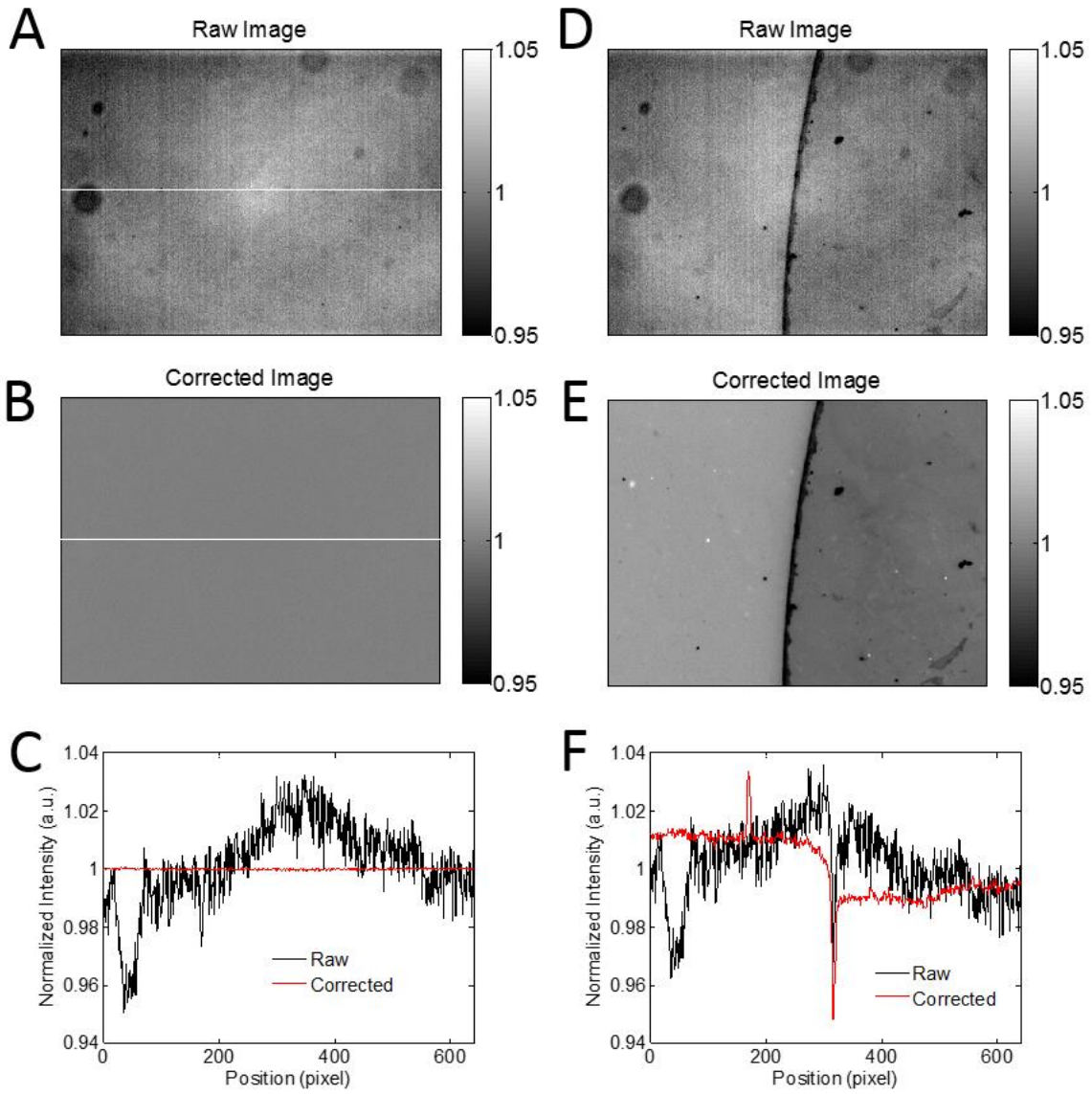

Figure 2.9 Results of calibrated CMOS research camera images. (A) Normalized raw image of a clear silicon surface. (B) Corrected image of (A). (C) Normalized intensity plots along the white lines in (A) (black) and (B) (red). (D) Normalized raw image with protein on silicon wafer (right half). (E) Corrected image of (D). (F) Normalized intensity plots along the white lines in (D) (black) and (E) (red).

2.5 Conclusion

In this chapter, we have shown the successful kinetics measurement of anti-IgG and IgG by the reflectance interferometry. This method is simple and based on silicon wafer which is widely used in semiconductor industry and thus is low cost. We have also shown the flat-field correction with each pixels removes both image's overall non-uniformity and artifacts due to dirt in optical pathway. This method also reduces the pixel-to-pixel variations to obtain 30 times lower spatial noise level than that before correction. This method is applied to all type of cameras from webcams to high quality research cameras. With this method, a thin layer of proteins on silicon wafer was obviously detected. The correction benefits pattern recognition, objective tracking and can be used for the future microarray measurement of reflectance interferometry.

CHAPTER 3

DETECTION OF MOLECULAR BINDING VIA CHARGE-INDUCED MECHANICAL RESPONSE OF OPTICAL FIBER

3.1 Introduction

High-throughput detection of molecular interactions is critical for understanding many biological processes, for detecting disease biomarkers, and for screening drug candidates [5]. To date the most widely used detection technique uses labels, such as fluorescence dyes. While popular and useful, the fluorescence-based approach can be problematic, especially when applied to the detection of small molecules, because the dye molecules can significantly alter the activities of small molecules, leading to inaccurate conclusions [8]. Various label-free techniques, such as surface plasmon resonance (SPR) technique [13, 39-41] and micro- and nanomechanical biosensors,[23, 29, 42, 43] and Quartz Crystal Microbalance [44] have been developed, but their sensitivities diminish with the size of the molecule [45]. Electrochemical impedance analysis [46-49] is also label free, but it detects interfacial capacitance or charge transfer taking place on an electrode surface, which is not universally applicable to the detection of different molecules, and its results are often difficult to quantify [50, 51]. A label-free method to detect small molecules still presents a technical challenge. On the other hand, small molecules are the most popular form of drugs, and play important roles in many biological processes [1], including post-translational modification of proteins (e.g., phosphorylation), metabolism (e.g., ATP production and consumption), and cellular signaling processes (involving hormones, neurotransmitters and other small molecules). A capability of detecting small molecules

will have large impacts on the understanding of these processes, detecting of diseases, and discovery of drugs.

In this chapter, we report a new optical technique for detecting of both large and small molecules. The technique is based on that most molecules relevant to biomedical research and applications are charged or partially charged. Even if for neutral molecules, they are expected to alter the charge distribution on a sensor surface upon binding. The sensor is an optical fiber, which is dipped into the well of a microplate. It detects the surface charge of the fiber by converting the charge into an optical signal, which does not decrease with the size (mass) of the molecule, making it particularly attractive for studying small molecules, and biochemical interactions that involve small mass changes. In addition, it is compatible with the standard microplate technology for liquid sample handling, which promises high throughput screening and analysis. We describe below the working principle, experimental setup, validation of the working principle, detection of large and small molecules, as well as fundamental detection limit of the technique.

3.2 Detection Principle and Experimental Methods

3.2.1 Detection Principle

The basic principle of the detection technique is illustrated in Figure 3.1A, showing a single optical fiber or a bundle of individually detectable optical fibers dipped in a well of a standard 96, 384 or 1536-well microplate. An alternating electric field is applied in a direction perpendicular to the fiber. If charge is present on the fiber surface, each fiber will be driven into oscillation by the applied field. The oscillation amplitude is detected optically by tracking the tip position of the fiber using a differential optical detection method detailed later. To study molecular binding, the tip is functionalized with molecular

probes. Upon binding of a target molecule onto the molecular probes, the surface charge of the fiber changes, which is detected by monitoring the oscillation amplitude.

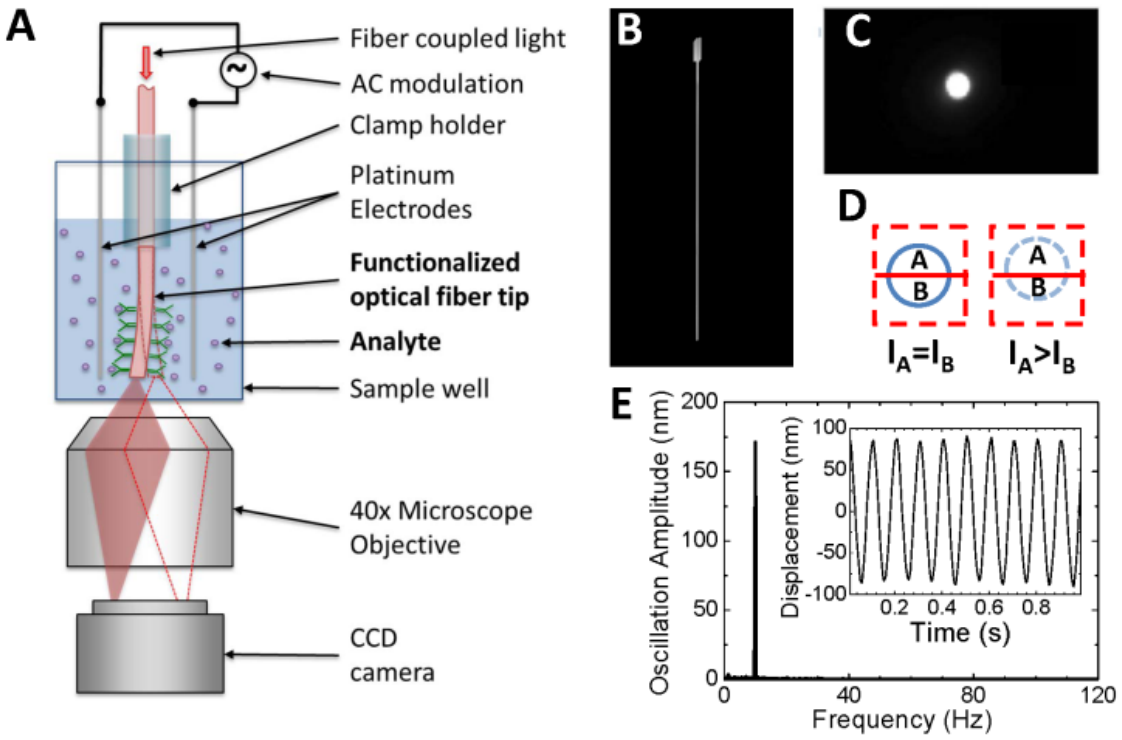

Figure 3.1 Overview of CSOD. (A) Schematic illustration of CSOD setup. (B) A typical optical fiber with etched tip viewed from side. (C) Image of the fiber tip viewed from the bottom of the microplate well. (D) Differential optical detection for accurate determination of the fiber oscillation amplitude. (E) Fast Fourier transform (FFT) of the fiber oscillation. Inset: Oscillation displacement signal in time domain before FFT. The amplitude and frequency of the applied voltage were 1 V and 10 Hz, respectively. The length and diameter of the fiber were 8.5 mm, and 11 µm, respectively. The buffer was 40 times diluted 1X PBS.

The key measurable parameter of the technique is the oscillation amplitude of the fiber tip, x_s, at frequency ω, which is proportional to the effective surface charge density, σ, of the fiber, given by

$$x_s = \frac{2\pi\left|\overrightarrow{E(\omega)}\right|\sigma r l}{\sqrt{\left(k_{eff}-m_{eff}\omega^2\right)^2+(c\omega)^2}}, \tag{3.1}$$

where $|\overrightarrow{E(\omega)}|$ is the electric field strength, c is the damping coefficient, and k_{eff}, m_{eff}, r and l are the effective spring constant, mass, radius and length of the optical fiber (Figure 3.1 B), respectively. The fiber was usually etched to around 10 μm in diameter. The etched optical fiber probe is considered as a cylindrical shape. Figures 3.2 B and C show the distal and upper parts of the fiber. They are of similar diameter which supports the assumption that the etched fiber tip is a cylinder. The effective spring constant, k_{eff}, of the cylindrical optical fiber probe is given by[52]

$$k_{eff} = \frac{3\pi E r^4}{4l^3}, \tag{3.2}$$

where E, r and l are the Young's modulus, radius and length of the optical fiber, respectively. $\overrightarrow{E(\omega)}$ is generated by applying a voltage between two electrodes inserted in the solution of the well, which is frequency dependent and given by

$$\left|\overrightarrow{E(\omega)}\right| = \left|\overrightarrow{E_0}\right|\frac{R_S}{\sqrt{R_S^2+\frac{1}{\left(\omega C_{eff}\right)^2}}}, \tag{3.3}$$

where R_S and C_{eff} are the solution resistance and effective interfacial capacitance respectively. In order to determine the resistance and effective capacitance, we measured the impedance ($|Z(\omega)|$) at different frequencies. $|Z(\omega)|^2$ is given by

$$|Z(\omega)|^2 = R_S^2 + \frac{1}{\left(\omega C_{eff}\right)^2}. \tag{3.4}$$

By fitting $|Z(\omega)|^2$ and frequency (ω), R_S and C_{eff} can be extracted. Figure 3.3 shows the fitting of $|Z(\omega)|^2$ and frequency (ω), from which we obtain R_S = 1.68 kΩ, and C_{eff} = 22.11 μF. From Eqs. (3.1) and (3.3), the frequency at which the oscillation amplitude reaches maximum is at

$$\omega_p = \sqrt[4]{\frac{k_{eff}^2}{(C_{eff}{}^2 c^2 - 2k_{eff} m_{eff} C_{eff}{}^2) R_S^2 + m_{eff}^2}} \quad . \tag{3.5}$$

We measured the oscillation amplitude of fiber at different frequencies, from which we determined the maximum frequency, ω_p. m_{eff} can be calculated from the diameter and length of the fiber, and c can be obtained from the frequency dependent amplitude. From the measured oscillation amplitude, x_s, we can determine the surface charge density of the fiber according to Eq. (3.1), which allows us to monitor the binding of molecules onto the fiber surface.

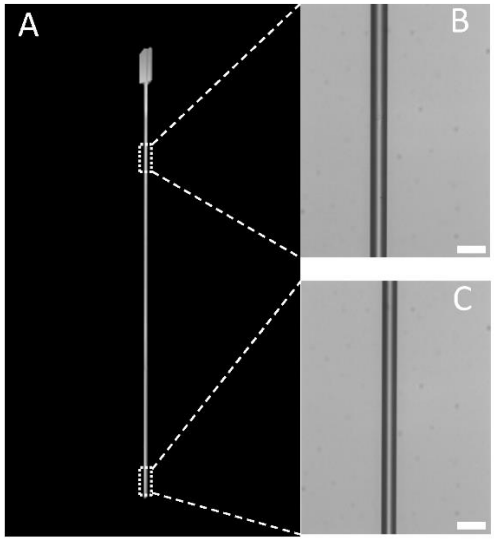

Figure 3.2 A typical optical fiber with etched tip viewed from side. (a) Side view of the entire fiber. (b) Zoom in image of the upper part of the fiber. (c) Zoom in image of the lower part of the fiber. Scale bar: 20 μm.

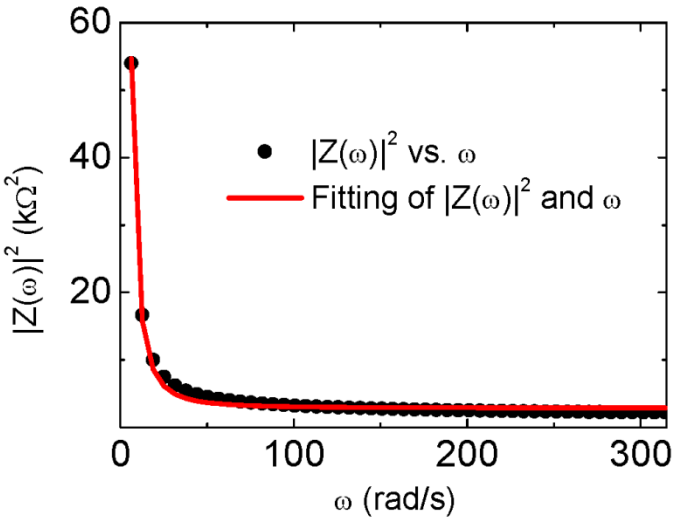

Figure 3.3 $|Z(\omega)|^2$ vs. frequency, where the black dots are experimental data, and red line is a fit to Eq. (3.4).

3.2.2 Differential Detection of Fiber Oscillation Amplitude

Accurate measurement of the oscillation amplitude is a key task in the present detection technique, which is achieved by a differential optical detection method that tracks the position of the optical fiber tip via optical imaging. The image of the tip from the bottom of the well, as obtained with an optical microscope, appears as a bright spot (Figure 3.1C). The differential optical detection method determines the oscillation amplitude of the optical fiber by dividing the bright spot into two regions, A and B, with a line perpendicular to the oscillation direction (Figure 3.1D). The division line is selected such that the intensities in regions A and B are similar initially, and $(I_A-I_B)/(I_A+I_B)$ is monitored continuously with the camera, where I_A and I_B are the intensities of regions A and B, respectively. The displacement of the optical fiber was determined precisely from the differential optical detection method, which requires calibration. We calibrated the detection method using the

following procedure. A region of interest (ROI) including the image of the fiber tip was selected as shown in Figure 3.4A. The ROI was divided into A and B, marked by red and blue boxes, respectively, and then shifted vertically by different numbers of pixels to mimic the fiber movement (Figure 3.4A). One pixel was determined to be 0.74 μm from the optical system and physical size of CCD camera. The differential intensity at each position was determined from the image. Figure 3.4B plots the differential intensity vs. pixel position, which shows a linear relation and serves as a calibration curve. It has been shown that $(I_A-I_B)/(I_A+I_B)$ is proportional to the oscillation amplitude of the fiber with a calibration factor determined experimentally.

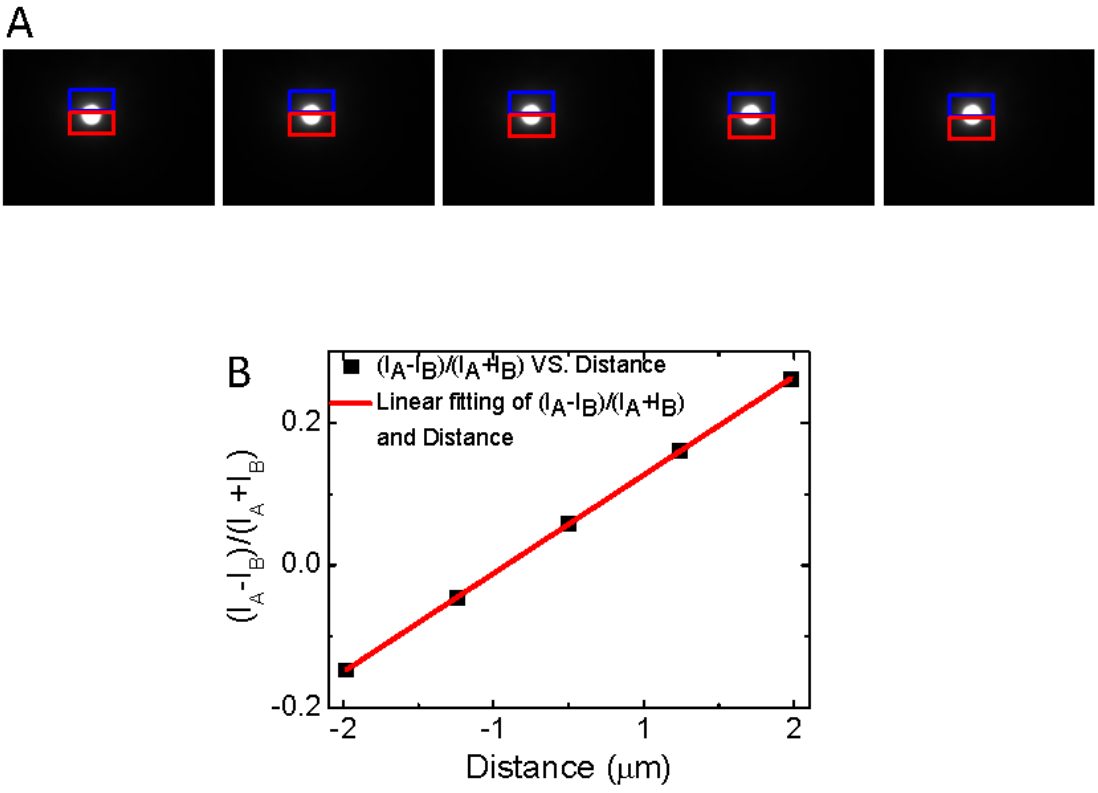

Figure 3.4 Calibration of oscillation amplitude. (A) Shifting ROI (red and blue boxes) to mimic fiber movement. From left to right, the ROI is shifted by -2, -1, 0, +1, +2 pixels, where "-" and "+" indicates moving the ROI upward and downward, respectively. (B)

Relationship between differential intensity $(I_A-I_B)/(I_A+I_B)$ and fiber movement (shifting of ROI), where the red line is a linear fit to the experimental data (black square).

This detection method is accurate because it rejects common noises in regions, A and B. It is clear that the sharper the fiber tip, the more sensitive the detection of the oscillation amplitude. For this reason, the fiber tip is etched into a sharp point to create a small bright spot in the image. With the differential optical detection principle we have determined the displacement of a fiber in response to an applied electric field. The inset of Figure 3.1E shows the oscillation of a fiber driven by a sinusoidal potential with frequency 10 Hz and amplitude 2 V. In addition to the use of the differential optical detection method, Fast Fourier Transform (FFT) filter is used to further remove noises at frequencies different from that of the applied electric field. Figure 3.1E is the FFT of the time domain data plotted in the inset of Figure 3.1E, which shows a sharp peak. From the peak height in the FFT spectrum, we determine the oscillation amplitude of the fiber. Using the combined differential detection method and FFT filter, we achieved a detection limit of 0.25 nm for the oscillation amplitude, corresponding to an effective charge detection limit of ~0.25 electron charge/μm^2. We will return to the discussion of detection limit later. Note that peak quality in the FFT spectrum increases with time duration, and we used a typical time duration of 1 second, which is fast enough for most molecular binding processes.

3.2.3 Materials and Methods

Preparation of optical fiber probes: A 125 μm diameter optical fiber from Thorlabs, Inc. was first soaked in acetone for 1 minute, then rinsed with deionized (DI) water, and finally dried out with N2. The polymer coating of the fiber was stripped off to expose the glass surface of the fiber with an optical fiber stripping tool. The bare optical fiber was

dipped in 47% Fluoric Acid (HF) for 30 minute, which etched the fiber down to ~12 μm in diameter. The etched fiber was thoroughly rinsed with DI water and then dried out with N2. To minimize surface contamination, the fiber was stored in a desiccator filled with N2 before using it.

The electric field was created with a two-electrode setup. A sinusoidal voltage wave generated by a function generator was applied between the two electrodes via a potentiostat (Pine, model AFCBP1). The applied voltage was controlled with a Matlab program.

Surface functionalization of optical fibers: The etched fiber was first modified with APTES ((3-Aminopropyl)triethoxysilane) to allow crosslinking of APTES to the probe molecules. Before surface functionalization, each etched optical fiber was cleaned with oxygen plasma for 3 minutes. The surface functionalization of the fiber took place in a desiccator, which was first purged with argon for 3 minutes before adding 30 μl of APTES and N,N-Diisopropylethylamine each into two small containers placed inside the desiccator. The desiccator was purged with argon for 3 more minutes and then sealed to allow surface reaction overnight. After the surface functionalization procedure, the optical fiber was placed in an oven heated to 110 °C for 30 minutes before each experiment.

For the detection of BSA, the amine-coated optical fiber was incubated in NHS-Biotin (N-hydroxysuccinimidobiotin) solution for 1 hour. The NHS-Biotin solution was prepared by dissolving 0.2 mg NHS-Biotin in 59 μl DMSO (dimethyl sulfoxide) and then adding it to 1.5 ml of PBS. After incubation, the fiber was rinsed with DI water and dried out with N2 before experiment. For the detection of imatinib, kinase c-Abl (or c Kit or myelin basic protein) was immobilized on the fiber with 1, 5-Glutaraldehyde by incubating amine-coated fiber in 2.5% 1, 5-Glutaraldehyde for 40 minutes. The fiber was rinsed with DI

water and then placed in the 0.8 μg/ml c-Abl solution (or 25 μg/ml c-Kit protein solution or 25 μg/ml myelin basic protein solution) immediately for 1 hour. The c-Abl (or c-Kit or myelin basic protein) modified fiber was rinsed with 1X PBS.

Experimental setup: An inverted optical microscope (Olympus IX70 with 40x objective) was used for the differential optical detection method. A 96-well microplate was placed on the microscope stage. Each optical fiber was placed between two platinum electrodes (1 cm × 0.5 cm) separated with a distance of 3 mm, and the assembly was mounted on a manipulator so that it could be moved in and out of the wells of the microplate easily. A CCD camera controlled by a homemade Matlab program was used to record the image of the optical fiber tip.

Data processing: The oscillation amplitude of the fiber was monitored by the CCD camera at 247 frames per second with the differential optical detection method. The relationship between the oscillation amplitude and the measured differential intensity from the differential optical detection method was determined before each experiment with the following method. The distance for one pixel of the image was known to be 0.74 μm from the optical system and CCD camera. The region of interest (ROI) containing the image of the fiber tip was shifted by different numbers of the pixels manually, and the corresponding changes in the differential intensity were determined from the images. The relationship between the differential intensity and the fiber movement (pixels) was found to be linear, from which the calibration factor of the differential detection method was determined (section 3.3.2).

3.4 Results

3.4.1 Validation of Detection Principle

In order to validate the working principle, it is essential to examine the predictions of Eq. (3.1). According to Eq. (3.1), the oscillation amplitude of the optical fiber is proportional to the applied electric field. To verify this, we measured the oscillation amplitude vs. applied voltage (Note: The voltage is proportional to the electric field.). The result is plotted in Figure 3.5A, which shows that the oscillation amplitude is indeed proportional to the applied field, as predicted by Eq. (3.1).

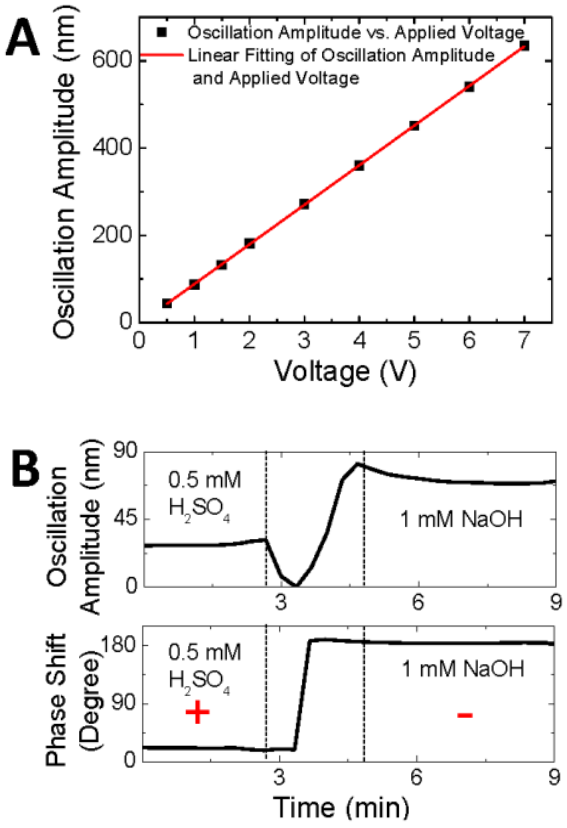

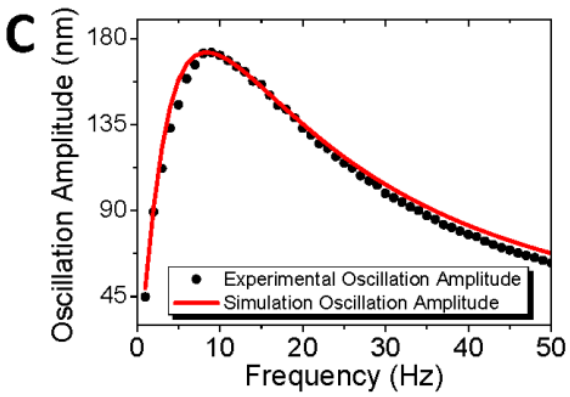

Figure 3.5 Theory validation of CSOD. (A) Fiber oscillation amplitude vs. applied voltage at 40 Hz, where the square dots are the experiment data, and the red line is the linear fit. Fiber diameter: 8 μm, length: 7.5 mm. (B) The oscillation amplitude (top panel) and phase (bottom panel) of an amine-modified fiber recorded during the change of the solution from low to high pH values. Fiber diameter: 20 μm, length: 10 mm. (C) Fiber oscillation amplitude vs. frequency, where the black dots are experimental data and the red line is the prediction of Eq. 1. Fiber diameter: 11 μm, length: 8.5 mm.

Equation (3.1) also predicts that the oscillation amplitude is proportional to the surface charge density, and the oscillation phase changes by 180 degrees when the charge changes polarity. To validate these predictions, we coated the fiber surface with amine-terminated silanes. The amine group has a pKa value between 10-11. When pH << 7, the amine group is protonated, resulting in a positive surface charge. In contrast, when pH >> 7, the amine group is neutral, but since the background silica is negatively charged, the surface is negatively charged. We measured the oscillation amplitude and phase in 0.5 mM H_2SO_4, then replaced the acidic solution with 1 mM NaOH. In 0.5 mM H_2SO_4, the phase shift is close to 0 degree, indicating that the oscillation is in phase with the applied electric field, which is consistent with the positively charged fiber surface (top panel, Figure 3.5B). After

replacing acidic solution with 1 mM NaOH, the amplitude decreases because of the de-protonation of the amine group, resulting in a decrease in the surface charge. When the amplitude decreases to zero, the phase changes by 180 degrees, indicating the change in the charge polarity (bottom panel, Figure 3.5B). The amplitude then increases as the surface becomes more and more negatively charged.

Another important prediction of Eq. (3.1) is the characteristic frequency-dependence of the oscillation amplitude. Figure 3.5C plots a typical frequency response of the oscillation amplitude, which shows a broad peak near 10 Hz. The frequency response can be fitted with Eq. (3.1) (red line) with calculated $k_{eff} = 7.6\times10^{-4}$ N/m, $m_{eff} = 1.8$ ng and fitting parameter $c = 7.5\times10^{-6}$ N·s/m, and the frequency dependent electric field. As indicated by the broad peak in Figure 3.5C and the parameters above, the oscillation is heavily damped, so that the amplitude is insensitive to mass changes associated with molecular binding.

3.4.2 Detection of Large Molecules

To demonstrate the detection of large molecules, we modified the fiber surface with streptavidin and studied the binding of biotinylated BSA to streptavidin (Figure 3.6A). Initially, we dipped the fiber into a microplate well filled with 350 µl of PBS buffer, and drove it into oscillation with an applied electric field. We then injected 10 µl of buffer (black arrow) into the well as a control, and observed no detectable changes in the oscillation amplitude, indicating that the injection of solution did not introduce significant mechanical perturbation. We then added 10 µl of 250 µg/ml biotinylated BSA (red arrow) into the microplate well, and found that the amplitude increased and then reached a stable level. The increase in the oscillation amplitude is expected because of the following

considerations. The isoelectric point (pI) of streptavidin is 5-6 [53], so the streptavidin-coated fiber was negatively charged in PBS buffer, which was confirmed from the phase of the oscillation. BSA was also negatively charged in the buffer because its pI is around 5 [54], therefore, the binding of biotinylated BSA onto streptavidin added more negative charges onto the fiber surface, causing an increase in the oscillation amplitude.

We further studied the binding of anti-BSA onto the BSA-coated fiber by adding 10 µl of 0.5 µg/ml anti-BSA into the well, which led to a final concentration of 0.2 nM anti-BSA. Figure 3.6B shows that the amplitude increased initially and then reached a stable value. This observation is consistent with that anti-BSA with a pI between 5.2-6.0 [55] is also negatively charged in the PBS buffer. Note that before adding anti-BSA into the well, 10 µl of buffer solution was added, and the change of amplitude was within the noise level, which again rules out the possibility that the observed oscillation amplitude change was due to mechanical perturbation by the introduction of the sample solutions.

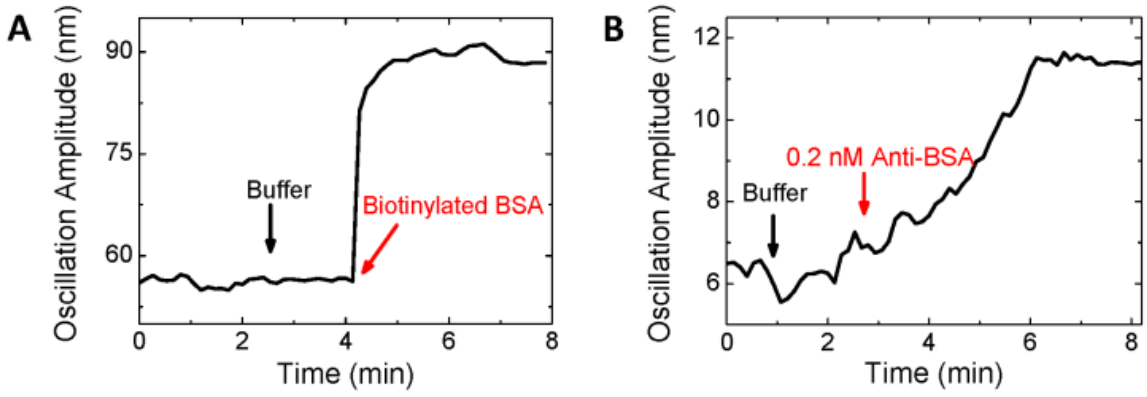

Figure 3.6 Protein detection by CSOD. (A) Biotinylated BSA binding onto streptavidin-coated fiber. The black arrow marks the addition of 10 µl buffer and the red arrow marks the addition of 10 µl 250 µg/ml biotinylated BSA (resulting in a final concentration of 100 nM biotinylated BSA). Fiber diameter: 11 µm, length: 7 mm. Buffer: 40 times diluted 1X

PBS buffer. (B) Anti-BSA binding onto BSA-modified fiber surface. The black arrow marks the addition of 10 µl buffer, and the red arrow marks the addition of 10 µl 0.5 µg/ml anti-BSA leading to a final concentration of 0.2 nM. Fiber diameter: 18 µm, length: 7.5 mm. Buffer: 40 times diluted 1X PBS buffer.

3.4.3 Detection of Small Molecules

To demonstrate the small molecule detection capability of the present detection technique, we studied the binding of imatinib to c-Abl (Figure 3.7A). c-Abl is a nonreceptor tyrosine kinase linked to the growth factor receptor signaling in human[56], and imatinib is an anticancer drug that inhibits the enzyme activity of c-Abl via binding to the ATP site of the protein[57]. The molecular weight of imatinib is 493 Da, which is difficult to detect by traditional label-free detection methods, especially when the surface coverage of c-Abl is low.

The optical fiber coated with c-Abl was first dipped into a microplate well containing 350 µl of 2.5 mM Tris-HCl buffer (pH=7.5) and 1 mM $MgCl_2$. Then 10 µl of the same buffer was injected into the well, and followed by repeated additions of 10 µl of 510 µM imatinib in 2.5 mM Tris-HCl buffer (pH=7.5) with 1 mM $MgCl_2$. Each addition corresponded to a 15 µM increase in the imatinib concentration. Similar to the finding described above, the addition of pure buffer resulted in no detectable changes in the amplitude of the optical fiber. In contrast, upon the first addition of imatinib (red arrow), the amplitude decreased sharply, and then reached a stable level. The decrease in the amplitude is expected because imatinib is positively charged. The second addition of imatinib produced a smaller decrease in the amplitude, due to the depletion of the c-Abl binding sites for imatinib. The solution in the well was changed back to the buffer (blue

arrow), which led to recovery in the amplitude due to the dissociation of imatinib. The phase shift between oscillation and electric field (Figure 3.7B) remained constant during the binding process, indicating no change in the charge polarity during the measurement.

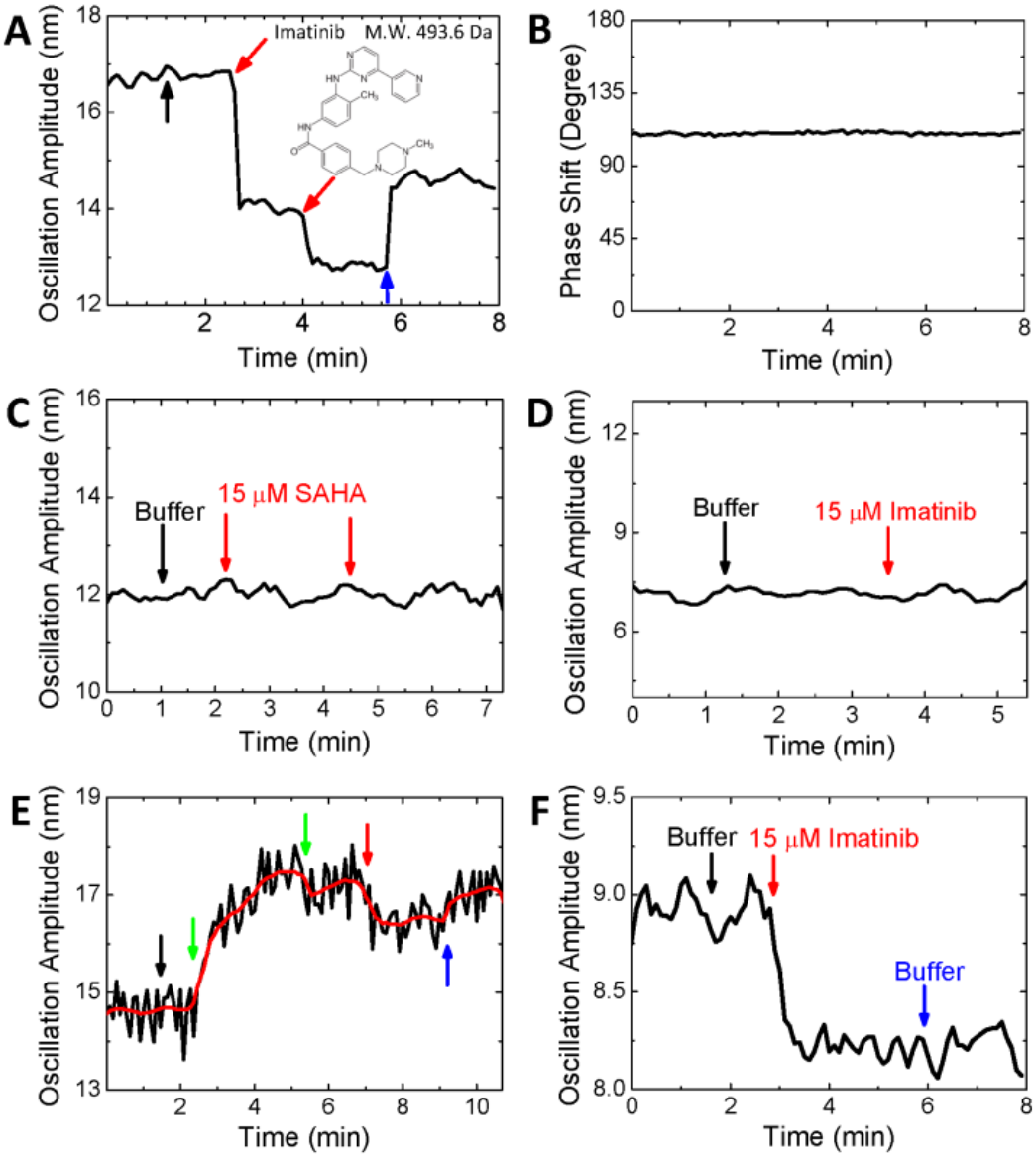

Figure 3.7 Small molecule detection by CSOD. The oscillation amplitude (A) and phase shift (B) of a c-Abl-modified fiber during the binding of imatinib onto c-Abl. The black arrow marks the addition of 10 µl buffer, the red arrows mark the additions of 10 µl 500

μM imatinib (final concentration of 15 μM), and the blue arrow indicates the change of the solution back to buffer. Fiber diameter: 11 μm, length: 7 mm. (C) Negative control. Two successive additions of 10 μl 500 μM suberoylanilide hydroxamic acid (red arrows) to the c-Abl-modified fiber. Fiber diameter: 12 μm, length: 7.5 mm. (D) Negative control. Response of a fiber modified with myelin basic protein to the addition of 10 μl 500 μM imatinib (marked by a red arrow). Fiber diameter: 10.4 μm, length: 7 mm. (E) Inhibition of c-Abl with AMP-PNP (green arrows), exposure of the inhibited c-Abl to imatinib (red arrow), and replacement of the solution with PBS buffer (blue arrow). Red line is the average of the raw data (black line). Fiber diameter: 10 μm, length: 7.5 mm. (F) Positive control. The fiber was modified with c-kit kinase, which interacts with imatinib. Additions of 10 μl buffer and 10 μl 500 μM imatinib (final concentration: 15 μM), and change of the solution back to buffer are marked with black, red and blue arrows, respectively. Fiber diameter: 16 μm, length: 8 mm. Buffer for above experiments: 2.5 mM Tris-HCl buffer (pH = 7.5) with 1 mM $MgCl_2$.

To further validate the observation above, we carried out several negative control experiments. The first negative control experiment was to expose a c-Abl coated optical fiber to suberoylanilide hydroxamic acid (SAHA). SAHA is a small molecule, and an inhibitor of pan-histone deacetylase, rather than c-Abl. The second negative control experiment was to coat an optical fiber with myelin basic protein, which does not bind to imatinib. In both cases, as shown in Figures 3.7 C and D, no changes in the oscillation amplitude were observed, which confirms that the observed changes in the oscillation amplitude in Figure 3.7A was due to the specific binding of imatinib to c-Abl, and non-specific binding of imatinib onto the areas that were not covered with c-Abl is negligible.

An additional control experiment was performed by first deactivating the binding sites of c-Abl with inhibitor, AMP-PNP, and followed by adding imatinib to the well. As shown in Figure 3.7E, upon the addition of AMP-PNP, the amplitude increased as AMP-PNP bound onto c-Abl and deactivated c-Abl. Note that the binding of AMP-PNP onto c-Abl caused an increase (green arrow), rather than a decrease in the amplitude as found in the case of imatinib. This is expected because AMP-PNP is negatively charged while imatinib is positively charged. Further addition of imatinib (red arrow) led to a small decrease in the amplitude. This control experiment provided extra evidence that the observed decrease in the amplitude shown in Figure 3.7A was due to specific binding of imatinib onto c-Abl.

Finally, we carried out a positive control experiment by immobilizing c-kit kinase. Like c-Abl, c-kit kinase can also be inhibited by imatinib[58]. Figure 3.7F shows the response of the oscillation amplitude of a c-kit kinase-coated optical fiber. Upon addition of 10 µl of 500 µM imatinib, the amplitude decreased as imatinib interacted with c-kit kinase, similar to the binding of imatinib onto c-Abl. This observation is consistent with the positive charge polarity of imatinib.

3.5 Discussion

3.5.1 Fundamental Detection Limit

The noise in the oscillation amplitude of the fiber is about 0.25 nm (averaged over 10 s) as shown in Figure 3.8A. In terms of charge density, the detection limit is 0.25 electrons/µm^2. This detection limit is excellent compared to FETs, including conventional silicon-based, nanotube-based [59-61] or nanowire-based FETs [62-64], which are also sensitive to charge changes. For example, assuming that a 10 nm diameter and 1 µm length silicon nanowire FET reaches detection limit a single electron charge, the corresponding

surface charge density detection limit is ~32 electrons/μm^2, 100 times less sensitive than that achieved with the present detection technique. In other words, FET can reach single electron detection limit in terms of total charge, but this detection limit is achieved at the expense of the effective detection area. The lowest analyte concentration that can be detected by a biosensor is determined by the number of detectable charges ***per unit area***, rather than by the total detectable charges.

The detection limit of the present detection technique is determined by many factors, including the light source, optical detector (CCD imager), and mechanical noise of the setup. These noises have been reduced by carefully designing the experimental setup, and by using the differential optical detection and FFT filter techniques, but the ultimate detection limit is determined by the following fundamental factors.

Brownian motion: One of the factors that determine the fundamental detection limit is thermal fluctuations or Brownian motion of the fiber. Based on the damped harmonic oscillator model described by Eq. (3.1), the thermal fluctuations of the fiber amplitude will lead to thermal noises in the surface charge density and given by [65]

$$\sigma_{thermal} = \frac{\sqrt{2k_B Tc\Delta\omega}}{2\pi|\vec{E}|rl}, \tag{3.6}$$

where k_B is the Boltzmann constant, T is temperature, $\Delta\omega$ is the bandwidth of detection. If integrating the signal over ~10 second, $\Delta\omega$ is about 0.2π, and the thermal noise limit on the detectable charge density is ~0.03 electron charges/μm^2 for an optical fiber with r=10 μm and l=1 cm, and electric field |E|=100 V/m at 10 Hz.

Surface charge fluctuations: In aqueous solutions, the surface charge density of the glass fiber is determined by the intrinsic surface properties but also by the balance in the adsorption and desorption of various molecular and ionic species in the solutions. The latter will result in surface charge fluctuations, leading to fluctuations in the oscillation amplitude of the fiber. If the total number of surface charges is N, then the fluctuation in the total surface charge is on the order of $\sqrt{N}$ e, and the corresponding fluctuation in the surface charge density is $\sqrt{N}$ e/2πrl. For a clean silica surface, the surface charge density is ~1 fC/μm^2 [66], the total number of surface charge is 2x10^9 electrons for a fiber of 10 μm in diameter and 10 mm in length, the surface charge density fluctuation according to above formula is ~0.14 electron charges/μm^2, close to the observed detection limit.

One way to examine the importance of the surface charge density fluctuation on the total noise of the measured oscillation amplitude is to study the noise vs. applied voltage. According to Eq. (3.1), the noise in the oscillation amplitude in the direction of the electric field caused by surface charge density fluctuations is proportional to the applied voltage. We measured the amplitude noise parallel to the electric field vs. the applied voltage, and found that it indeed increased linearly with the voltage (Figure 3.8B). We also determined the amplitude noise perpendicular to the electric field (Figure 3.8C), which shows only a weak dependence with the voltage. These observations indicate that the noises in the oscillation amplitude are primarily due to the fluctuations in the surface charge density of the fiber.

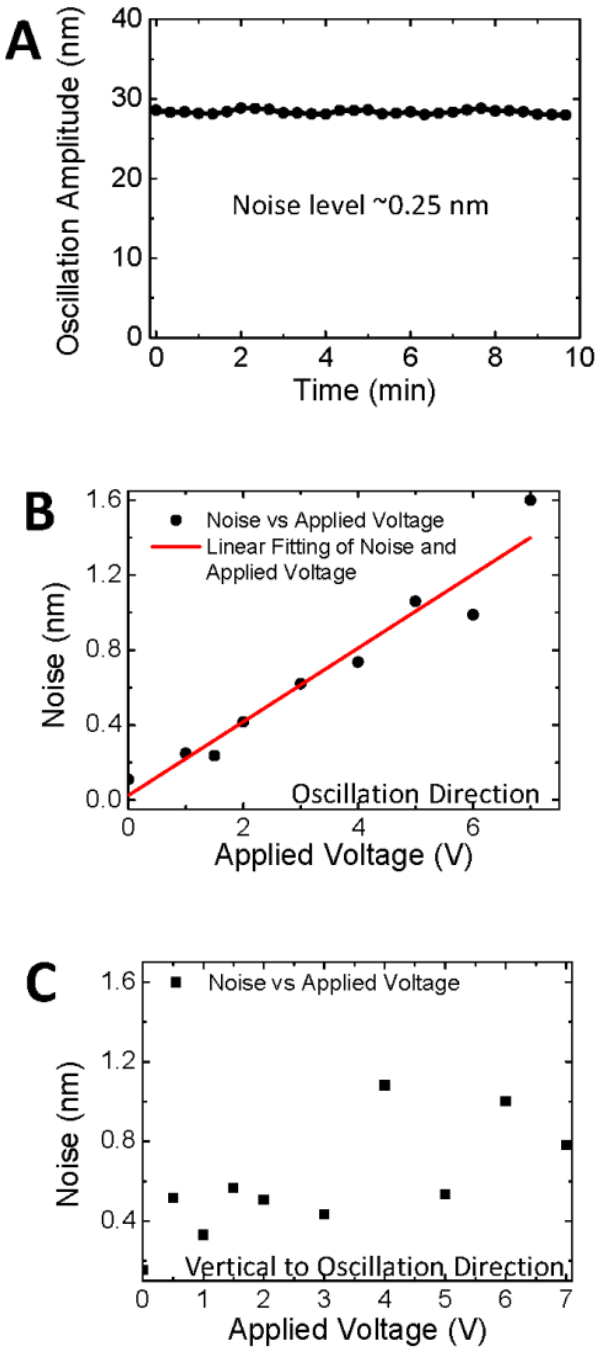

Figure 3.8 Detection limit and noise analysis of CSOD. The root-mean-square of the noise level in the amplitude is 0.25 nm (A). Fiber diameter: 20 μm, length: 10 mm. Dependence of noise in the oscillation amplitude on the applied voltage in the parallel (B) and

perpendicular (C) directions of the field. Fiber diameter: 10 μm, length: 7 mm. Buffer for above experiments: 40 times diluted 1X PBS buffer.

Charge screening: The detection limit for x_s in our preliminary experiments is 0.25 nm, corresponding to an effective charge detection limit of ~0.25 electron charge/μm^2. Ionic screening will reduce the effective charge, and thus affect the actual detection limit. The screening factor, defined as the ratio of the effective charge to the actual charge, is calculated as a function of ionic concentration with the Debye-Hückel theory. The screening factor depends on the non-slipping layer thickness (non –slipping layer defines a layer of water that moves with the fiber). The calculation shows that despite the ionic screening substantial effective charge remains even at relative high ionic concentration. Such screening depends on the ionic concentration as shown in Figure 3.9. For a 100 mM ionic solution, the ionic screening will reduce the effective charge to ~10% of the actual surface charge, leading to a detection limit of ~2.5 electron charges/μm^2.

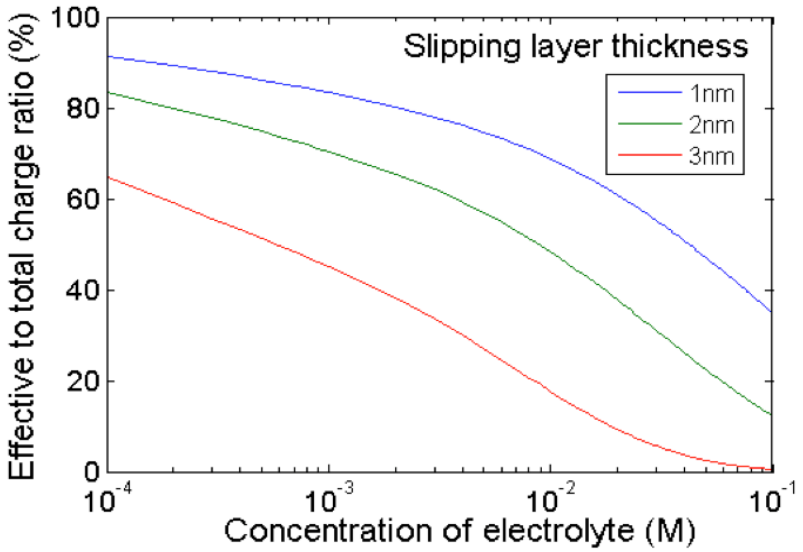

Figure 3.9 Ionic screening and effective surface charge density (presented as the ratio of the effective surface charge to the actual charge).

3.5.2 Dynamic Range

The dynamic range of a detection technology is determined by the ratio of the maximum to minimum binding signals it can measure. In the present detection technique, the minimum signal is determined by random charge fluctuations, which is about ~0.25 electron charge/μm^2. The maximum signal is limited only by the size of view of the optical imaging system. Since we can also lower the driving electric field (i.e., lower the gain), the estimated upper limit is ~2.5 x 10^7 electron charge/μm^2, leading to an extremely large dynamic range (~10^8). However, the actual upper limit in the signal is likely to be determined by how many molecules can pack to the surface of the fiber. Assuming a packing density of 10^6 molecules/μm^2, the dynamic range would be 10^6-10^7. This dynamic range is superior to other detection technologies, including FET and EIM mentioned above.

3.5.3 Immunity to Interference and Temperature Drift

Note that FETs mentioned above are sensitive to various processes other than charge, such as binding-induced capacitance changes, and ionic impurity trapping in the electronic materials and interconnections due to the complex biological media. In contrast, only the optical fibers are inserted in the media and the detection is performed optically outside of the solution well.

An additional benefit of the present detection technique is its temperature stability. The FETs and SPR are sensitive to temperature because the charged carriers in the FETs and refractive index measured by SPR are strongly temperature dependent. The technique measures the fiber oscillation, which is insensitive to temperature drift (Figure 3.10). To examine possible temperature effect on the performance, the temperature of solution in the well and the oscillation amplitude of the optical fiber were simultaneously measured.

Figure 3.10A plots the temperature of a solution well within 10 min, which shows ~0.2 °C of temperature drift of the setup. This temperature drift did not cause any detectable changes in the oscillation amplitude of the optical fiber. The buffer solution was heated up to 29 °C and then cooled down. This relative large temperature variation did not produce any detectable drift in the oscillation amplitude either (Figure 3.10B), which demonstrates excellent temperature stability of the detection platform. However temperature does affect the binding kinetics because of the fundamental thermodynamics of molecular binding processes.

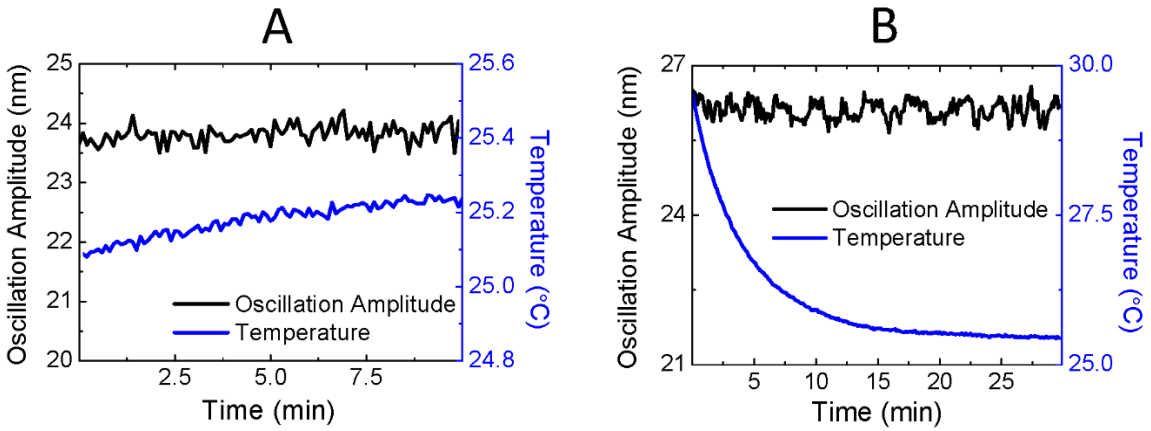

Figure 3.10 Temperature Effect. (A) Drift of ambient lab temperature did no effect the fiber oscillation amplitude. (B) Heating and cooling over a large temperature range (4 °C) did not cause a drift in the fiber oscillation amplitude either. Fiber length: 9 mm, diameter: 20 µm. Buffer: 40 times diluted 1X PBS buffer. Vpp = 6 V @ 55 Hz.

3.5.4 Repeatability

The technique shows good repeatability among different fibers for molecular interaction measurement. The repeatability is dependent on the repeatability of sample preparation, i.e. etching of fiber probe, surface modification of fiber probe. To demonstrate

the repeatability, both large and small molecule binding experiments were repeated three times on three different optical fibers respectively.

Anti-BSA and BSA

Three optical fibers were prepared following the same procedure (see Experimental Section for details). Briefly, amine coated fibers were incubated in 2.5% 1, 5-Glutaraldehyde for 15 min and then in 0.1 mg/ml BSA for 1 h 15 min. Figure 3.11 shows the responses of the three optical fibers to 10 µl 0.5 mg/ml anti-BSA (final concentration of 215 nM). The results are similar to each other, demonstrating the repeatability of the present detection technique.

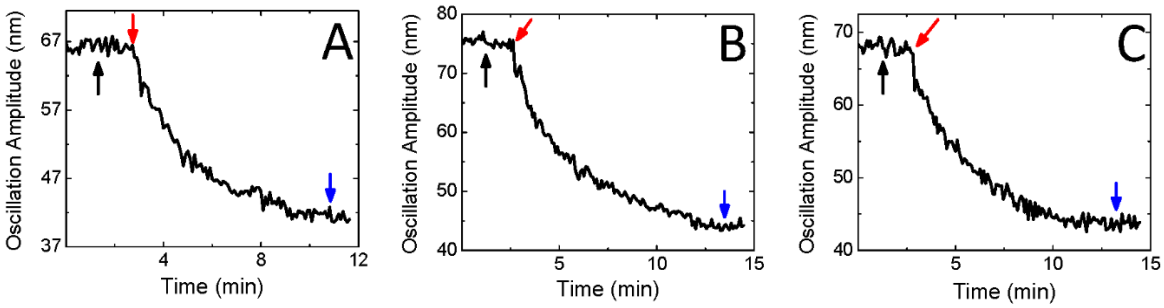

Figure 3.11 Measurements anti-BSA binding to BSA with three different optical fibers. The black arrows mark the addition of 10 µl buffer for control, the red arrows mark the additions of 10 µl 0.5 mg/ml anti-BSA (final concentration of 215 nM), and the blue arrows indicate the change of the solution back to buffer. Fiber length: 8.5 mm, diameter: 22 µm. Vpp = 4 V @ 20 Hz**.**

Imatinib and c-Abl

Figure 3.12 shows the binding of imatinib to c-Abl for three different optical fibers. Fibers were modified with c-Abl through 1, 5-Glutaraldehyde according to the procedure

described in the Methods part. The responses of the three optical fibers to 10 µl 500 µM imatinib (final concentration of 15 µM) are similar, further demonstrating good reproducibility of the setup.

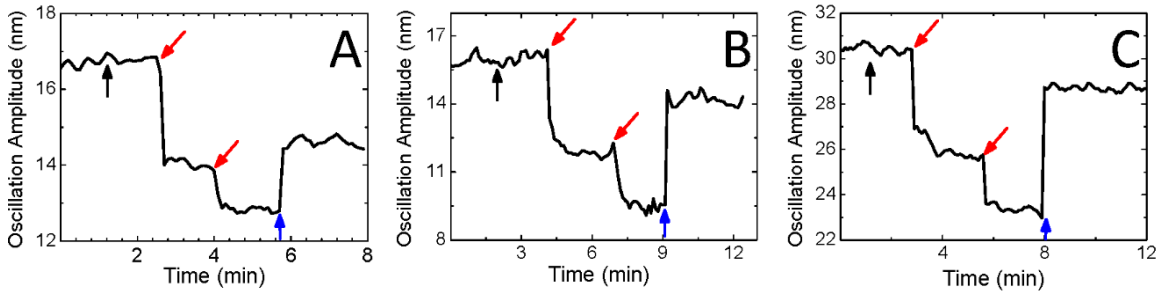

Figure 3.12 Measurements of small molecule (imatinib) binding processes with three different optical fibers (A, B and C). These fibers were modified with c-Abl. The black arrows mark the addition of 10 µl buffer, the red arrows mark the additions of 10 µl 500 µM imatinib (final concentration of 15 µM), and the blue arrows indicate the change of the solution back to buffer. Fiber length: (a) 7 mm, (b) 7.5 mm, (c) 7.5 mm. Fiber diameter: (a) 11 µm (b) 13 µm, (c) 12.6 µm. Vpp = 2 V @ 40 Hz.

3.5.5 Concentration Dependence

To demonstrate that the present detection technique can measure different concentrations of analyte, amine-coated optical fibers were modified with BSA via 1, 5-Glutaraldehyde to measure anti-BSA of different concentrations. The fibers were first coated with amine by APTES (see Methods part), and then BSA by incubating them in 2.5% 1, 5-Glutaraldehyde for 15 min and in 0.1 mg/ml BSA for 1 h. Right after the BSA modification, binding of the fibers to different concentrations of anti-BSA were measured and the oscillation amplitude change before and after anti-BSA addition vs. anti-BSA concentration was plotted in Figure 3.13. The experiment data (dots) were fitted with the

Langmuir isotherm, $y = \frac{y_{max} \cdot c}{K_D + c}$, where y, c, and K_D are the oscillation amplitude change, anti-BSA concentration and dissociation constant, respectively. K_D was found to be 2.5 nM from the fitting, which is in agreements with other studies.

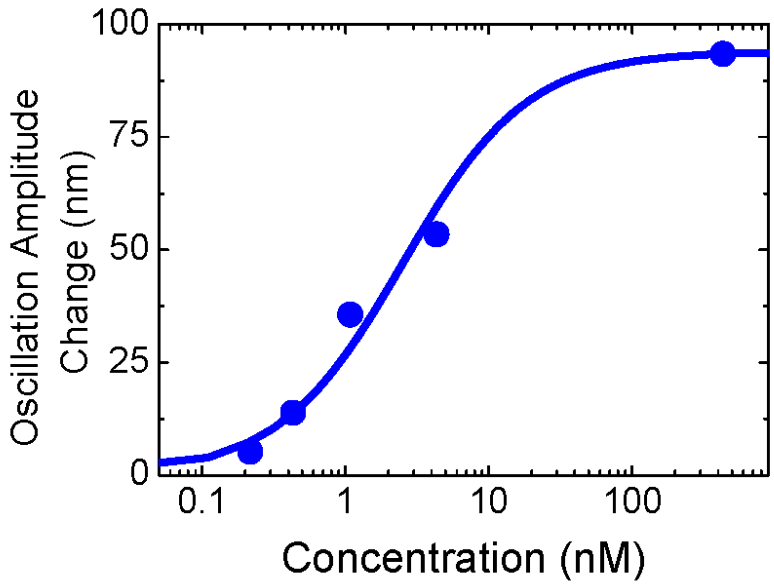

Figure 3.13 Response curve of BSA-coated optical fiber to different concentrations of anti-BSA, where the dots are experimental data, and solid line is a best fit of the data to the Langmuir isotherm.

3.5.6 Towards High Throughput Detection

One of the most important advantages of the present detection technique is its compatibility with the standard microplate platform, consisting of either 96, 384 or 1536 wells. Unlike most microarray platforms, each of the well is chemically isolated from other wells, preventing cross talking and cross contamination.

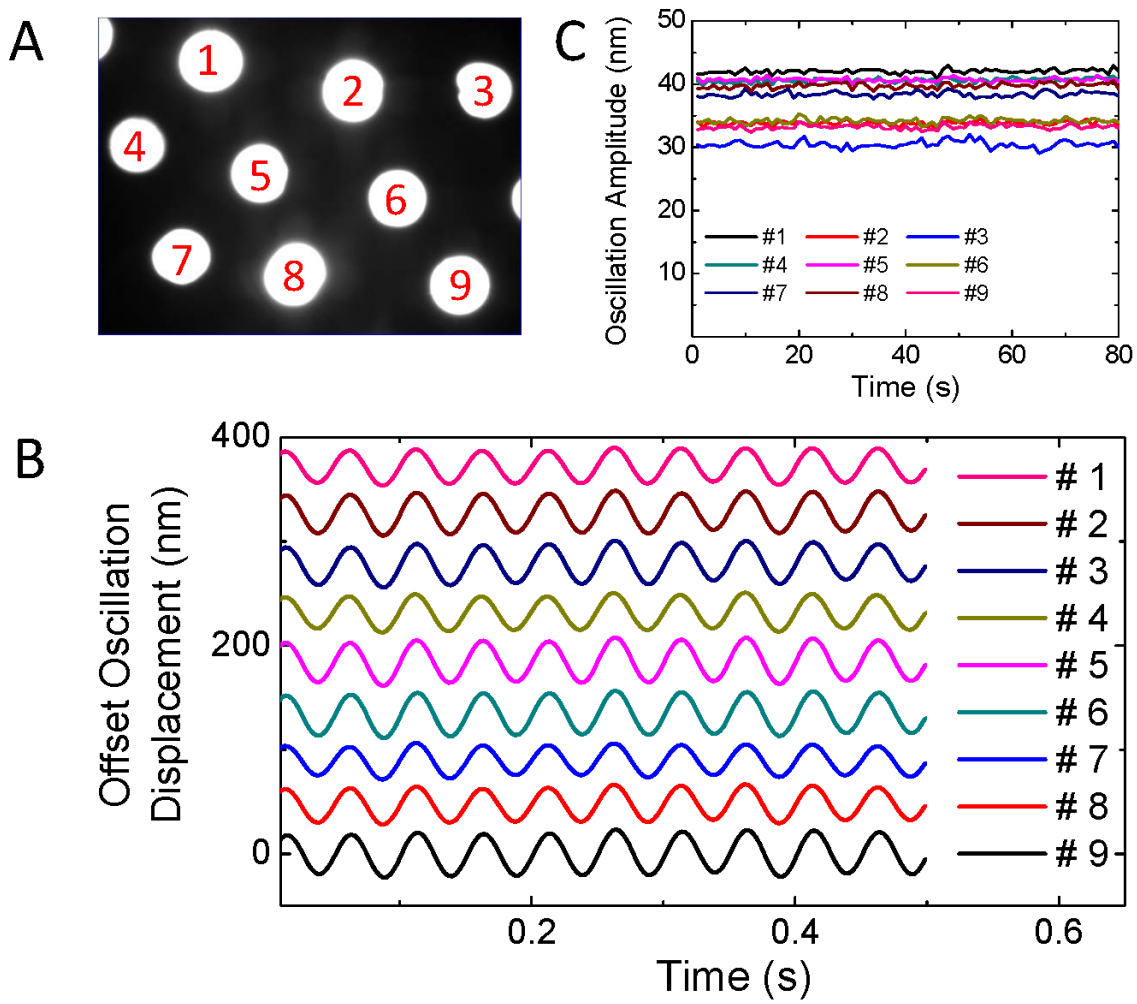

Figure 3.14 High throughput detection using an optical fiber bundle (A). Simultaneously measured oscillation displacement (B) amplitude (C) of each fiber over time.

Fiber bundles

In order to demonstrate high throughput capability, we created an optical fiber bundle consisting of 15 optical fibers manually. Each fiber is 1 cm long with its plastic coating stripped off to expose the silica cladding surface. The fiber bundle was used as a probe and dipped into a well of the 96-well plate containing 0.5 mM NaOH. Figure 3.14 shows the ends of 9 optical fibers from the bottom of the well through an inverted optical microscope

with a 4X objective. Figures S4 b and c show the oscillation displacement and amplitude of the individual fibers over time. The voltage applied was a sinusoidal wave with 20 V of amplitude and frequency of 20 Hz.

Automated system for multiple well analysis

The optical bundle probe can be moved from one well to another, controlled with a computer-controlled automation setup to perform high throughput screening tests The control system can be programmed, which moves the optical fiber probe vertically in and out a well, and horizontally from one well to another well for multiple step analysis. The time scale achieved with the setup is 2 s, limited by the motor used in the current setup. Figure 3.15 shows fast and reproducible amplitude signal as we switched the fiber probe in and out between two solution wells.

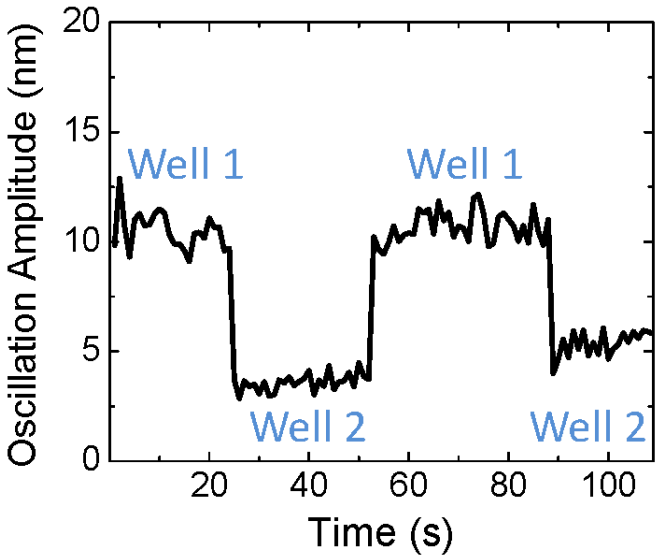

Figure 3.15 Automated switching of the optical fiber probe between two wells in a microplate.

3.6 Conclusion

We have validated the working principle of a detection technique based charge-induced mechanical response with optical fibers, demonstrated its application for the detection of both large and small molecules, and evaluated the detection limit. The method is based on the detection of the charge, so that the output signal does not decrease with the molecular mass. The optical fibers used here are commercially available fibers for optical communications, which are uniform, pure and inexpensive. The setup is based on the conventional microplate platform, making it suitable for high throughout applications, especially when multiple fiber probes are used and automatically switched among different wells. The detection system is based on the conventional optical microscope, which has been shown to be simple and low noise. Using a differential optical detection and FFT filters, the charge detection limit is only limited by the surface charge fluctuations associated with the fundamental molecular and ionic binding processes taking place on a surface. We anticipate that the optical fiber-based technique become a useful tool for high throughput study of molecular interactions, for detection of disease biomarkers and for discovery of drugs.

CHAPTER 4

KINETICS OF SMALL MOLECULE INTERACTIONS WITH MEMBRANE PROTEINS IN SINGLE CELLS MEASURED WITH MECHANICAL AMPLIFICATION

4.1 Introduction

Advances in structural biology have led to an exponential growth in the number of membrane proteins with determined 3D structures [67]. However, in order to understand the cellular functions of membrane proteins, it is also necessary to determine the interaction kinetics of the membrane proteins with various molecules. This is because cells perform many functions, including communication, via the interactions of their membrane proteins with molecules in the extracellular medium. A capability to quantify membrane protein interactions with molecules is also critical for discovering and validating drugs because most drug targets are membrane proteins [68, 69]. Despite the importance, developing such a capability that can measure the interactions of molecules with membrane proteins in the natural lipid environment has been a difficult task.

The traditional method for studying molecular interactions uses radioactive or fluorescent labels. These end point assays do not provide kinetic constants that are needed to quantify the membrane interactions and functions [70, 71]. To determine the kinetic information, the current practice involves extracting membrane proteins from cells, purifying them from the extracts, immobilizing the purified proteins on a solid surface, and then exposing them to a ligand for kinetic study [72]. The procedures are not only laborious, but also prone to alteration of the native functions of membrane proteins, especially integral membrane proteins that are permanently attached to the membrane. Furthermore, the

isolation of membrane proteins from their native cellular environment prevents one from studying the allosteric effect in the molecular interactions[73], and examining heterogeneous nature of cells [74, 75]. Measurement of binding kinetics of membrane proteins on cells [76] or lipid bilayers [77, 78] has been demonstrated with surface plasmon resonance (SPR) and SPR with novel nanostructures, such as nanoparticles and nanopores. However the limitation of these technologies is that the detection signal diminishes with the mass of the molecule, making them difficult for detecting small molecules, which play many important roles in cellular functions, and represent the vast majority of the existing drugs.

In this chapter we report an observation of mechanical deformation of cells upon interactions of the cellular membrane proteins with molecules in the extracellular medium, and demonstrate a capability of real time analysis of the interactions in single cells by analyzing the mechanical deformation with sub-nm resolution. We refer to this method as mechanically amplified detection of molecular interactions (MADMI). Using this capability, we have monitored the kinetics of both large and small molecule interactions with membrane proteins, including glycoproteins and ion channels in intact cells (fixed or live), and obtained the binding kinetic constants. For large molecules, the kinetic constants agree with those obtained with a plasmonic imaging technique. For small molecules, the present method represents the first kinetic measurement, and direct comparison with other techniques is not possible, but the equilibrium constants extracted from the present method are consistent with those obtained with endpoint radioactive labeling assay. The imaging capability allowed us to reveal cell-to-cell variability of difference cells, and region-to-region variability within the same cell.

4.2 Detection Principle

The principle to measure the mechanical deformation in the cellular membrane associated with the binding of molecules with the membrane proteins are illustrated in Figure 4.1. The mechanical deformation is expected because the law of thermodynamics predicts that when molecules bind to a surface, the surface tension changes, leading to a mechanical response in the cell membrane (Figure 4.1 E). According to thermodynamics, the surface concentration (Γ) of molecules bound on the membrane surface is given by

$$\Gamma = -\frac{d\gamma}{d\mu} \tag{4.1}$$

at a fixed temperature and pressure, where γ is the surface tension and μ is the chemical potential of the molecules. For ideal solutions, the chemical potential is related to the bulk concentration, c, according to

$$d\mu = RTd(\ln c), \tag{4.2}$$

where R is the gas constant, and T is temperature. From Eqs. (4.1) and (4.2), at given concentration of analyte, molecular binding is directly proportional to the surface tension change, and one can thus determine the molecular interactions with the membrane proteins by measuring the mechanical deformation in the membrane (Figure 4.1 C). Note that according to Eq. (4.1) the mechanical deformation detected here does not depend on the size of the molecule, so the method works for both large and small molecules.

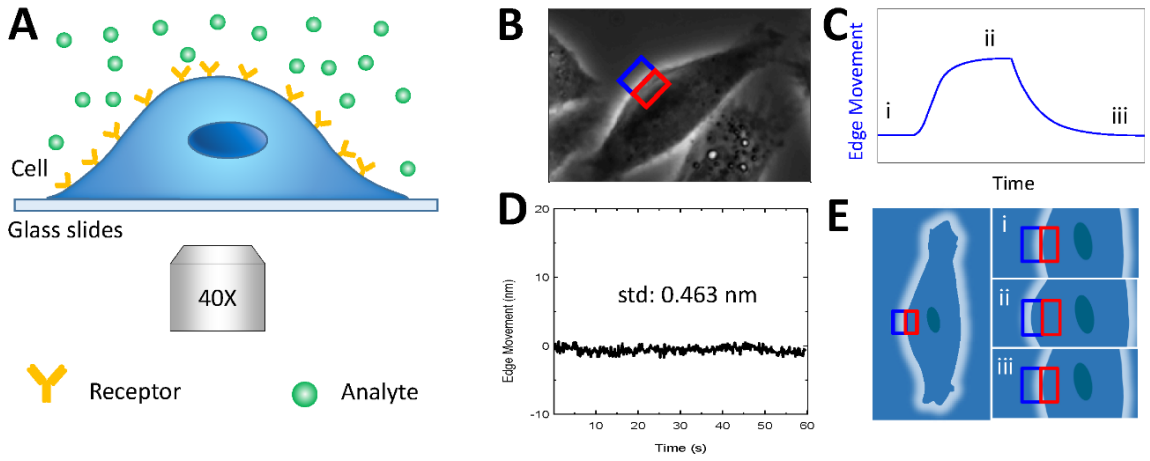

Figure 4.1 Detection of molecular interactions with membrane proteins in cells via mechanical amplification. (A) Schematic illumination of the setup based on an inverted phase contrast microscope with 40X phase 2 objective was used for detection. (B) Differential optical detection for accurate tracking of cell edge change induced by analyte receptor interaction. (C) Schematic of a typical binding curve as determined from the cell edge movement. (D) The root mean square of the fixed cell edge change is 0.46 nm. (E) Illustration of cell edge changes over time during the binding process, where i, ii, and iii correspond to the stages marked in (C). Blue and red rectangles in (B) and (E) are the regions of interest for differential detection.

4.3 Differential Optical Detection and Experimental Setup

To detect the binding of a small amount of molecules, it is critical to be able to measure a small mechanical deformation in the cell membrane. Although Atomic Force Microscope (AFM) could, in principle, be used to measure cell deformation [79-81], we developed a simple method by tracking the edge movement of a cell with an optical microscope using a differential detection algorithm. Compared to AFM, it is non-invasive and fast, allowing multiple cells to be measured simultaneously. The differential detection

algorithm allowed us to achieve a detection limit of 0.5 nm of cell edge movement, the size of an atom, with millisecond temporal resolution (limited only by the frame rate of the CCD camera).

Figure 4.1A shows a schematic illustration of the experimental setup based on an inverted optical microscope. An inverted microscope (Olympus X81) equipped with a phase 2 condenser and phase 2 40X objective was used with illumination from the top of the sample cells. The edge of a cell is clearly revealed with conventional phase contrast optical imaging, as shown in Figure 4.1B. A rectangular region of interest (ROI) is defined such that the edge of a cell passes through the center of the rectangle, dividing the ROI into two equal halves, one half is inside of the cell, and the second half falls outside of the cell. We denote the intensities of the two halves as A and B. If the cell expands upon molecular binding (Figure 4.1C), then A decreases and B increases (Figure 4.1E). We measure differential image intensity, (A-B)/(A+B), and use it to determine the movement of the cell edge at each location. The relation between the cell edge movement and (A-B)/(A+B) was determined and calibrated using the following procedure. The pixel density of each image was increased by 5 times by adding additional pixels with a bilinear interpolation approach. The distance between two pixels in the interpolated image was 37 nm (Pike F032B CCD, Allied Vision Technologies, Stadtroda, Germany). The edge of one cell was manually chosen and the centroid (O) of the cell was determined (Figure 4.2A). A polar coordinate system was set up with the centroid serving as the pole. The cell edge movement was calculated at every 1 μm starting from 0˚ (Figures 4.2 A and B). The ROI at a certain point of the cell edge (point A) was then shifted by different numbers of pixels outwards (perpendicular to the tangential line at point A), and the corresponding changes in the

differential image intensity was determined from the image. The relation between the differential image intensity and the cell edge movement (pixels) was found to be linear within a certain range, which served as a calibration curve to determine the cell edge movement (mechanical deformation) from the differential image intensity. By following the cell edge movement, we obtain the binding kinetics as illustrated in Figure 4.1C.

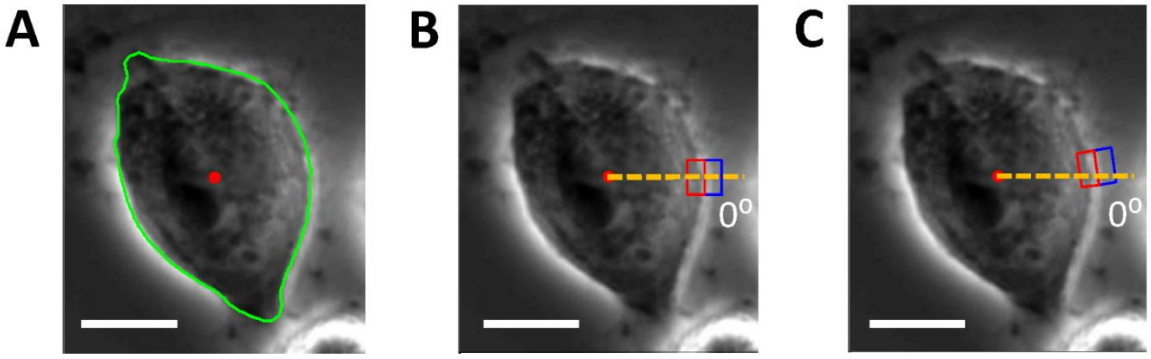

Figure 4.2 Calibration of the differential imaging intensity and cell edge movement. (A) The boundary (green line) of the cell was chosen manually and the centroid (red dot) of the cell was determined with an imaging-processing algorithm. (B) and (C) A region of interest (ROI) was chosen at every 1 μm along the cell boundary from 0˚ in the polar coordinate system where cell centroid was the pole. ROI in c is 4.6 μm away from that in B. Scale bar: 10 μm.

We refer to this method of edge tracking as differential optical detection. The differential optical detection subtracts out common noise in the optical system, thus providing superior detection limit. Figure 4.1 D plots the noise level over time, showing a standard deviation of 0.46 nm. Although we focus on phase contrast imaging in the present work, this optical detection algorithm can be readily applied to other optical imaging modes, such as bright field [82] and surface plasmon resonance.

4.4 WGA and Glycoprotein Interaction

To demonstrate the capability of the method for detecting and quantifying the interactions of molecules with the membrane proteins, we first studied molecular binding to glycoproteins. Glycoproteins are the most abundant membrane proteins with sugar groups extended into the extracellular space of the cells, which is critical in cell recognition and communication with various signaling molecules via specific interactions [83]. An important example of the specific interactions is between lectins, proteins that bind to and recognize specific sugar structures, and glycoproteins on the cell membranes. We studied wheat germ agglutinin (WGA), a lectin that can specifically recognize N-acetylglucosamine (GlcNAc) and sialic acid groups on Barrett's esophagus derived CP-D (CP-18821) cells. The CP-D cell were cultured in an incubator at 37˚C with 5% CO2 and 70% relative humidity. Cells were cultured in 25 cm^2 flask with 1x Keratinocyte-SFM (Life Technologies, Carlsbad, CA) and penicillin-streptomycin (BioWhittaker, Basel, Switzerland) as culture medium. When cells reached approximately 80% confluent, cells were passaged with 0.05% trypsin-EDTA (Life Technologies, Carlsbad, CA). For experiments, cells were cultured overnight on the bare glass slides (22×60 mm micro cover glass, VWR, Radnor, PA) in a silicone well (FlexiPERM, Greiner bio-one, Monroe, NC) placed on top of it in order to let cells attach on the surface. Cells on glass slides were also cultured in the incubator at 37 with 5% CO2 and 70% relative humidity. Cells were incubated in 4% paraformaldehyde for 10 min at room temperature for fixation and then ready for experiments. Before the measurement, the small silicone well was changed to a homemade PDMS well with 2 cm in length, 1 cm in width and 1 cm in height.

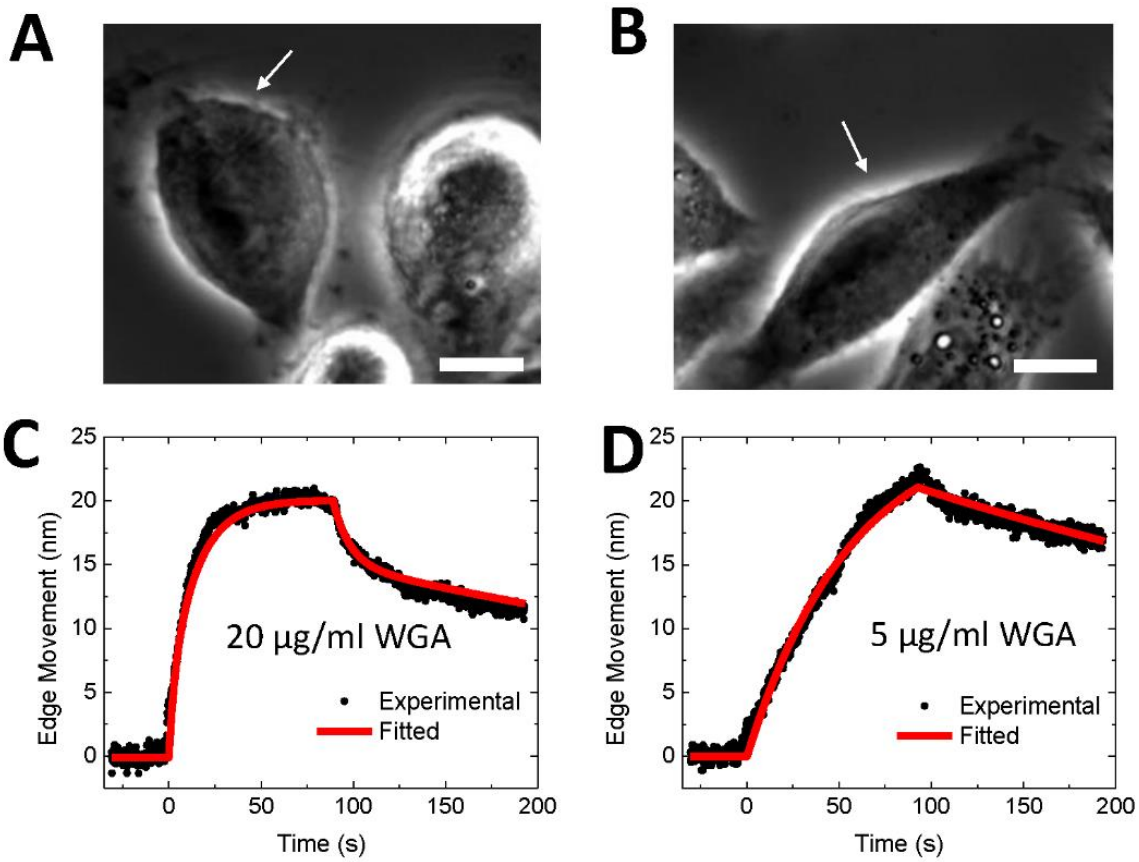

Figure 4.3 Large molecule interactions: WGA interaction with glycoproteins. Phase contrast images of fixed CP-D cells for 20 µg/ml (A) and 5 µg/ml WGA (B) binding, respectively. The white arrows mark the cells under analysis. The averaged cell edge movement over the whole cell (black dots) and global fitting (red curves) for 20 µg/ml (C) and 5 µg/ml (D) WGA, respectively. Scale bar: 10 µm.

Figures 4.3 A and B show the phase contrast images of CP-D cells attached to a glass slide. The measurement was carried out by first flowing 1X PBS over the cells with a flow rate of 350 µL/min for 30 s to obtain a baseline. WGA in 1X PBS was then introduced for 90 s to allow the binding or association of WGA with the glycoproteins on the cell surface. During the association process, the cell edge moved outwards as shown in Figures 4.3 C and D. After the association process, the flow of the WGA solution was switched to 1X

PBS to allow the bound WGA to dissociate from the cells. Figures 4.3 C and D show that the cell edge moved back to the original position during the dissociation process. By globally fitting the data with the first order kinetics, the association rate constant (k_{on}), dissociation rate constant (k_{off}), and dissociation constant (K_D) were found to be $k_{on} = 1.1 \times 10^5\ M^{-1}s^{-1}$, $k_{off} = 2.2 \times 10^{-3}\ s^{-1}$ and $K_D = 0.019\ \mu M$. WGA binding to glycoproteins on live cells was also detected with the same method (Figure 4.4). The results from both fixed and live cells are in good agreement with those obtained with plasmonic imaging method reported by us recently [76].

Another example is the binding of anti-EGFR antibody to EGFR on A431 cells. Epidermal growth factor receptor (EGFR) is a transmembrane receptor that is related to a variety of cancers and regulates cell proliferation, apoptosis and invasion. Monoclonal antibodies (mAb) targeting the extracellular domain of EGFR has shown good therapeutic efficacy for treatment of a number of cancers. The binding kinetics between mAb and EGFR is critical to determine the drug efficacy. We measured the mAb and EGFR interaction in fixed A431 cells with the present method. The association rate constant, dissociation rate constant and dissociation constant were obtained by fitting the experimental data with first order kinetics. The dissociation constant obtained from the kinetics study matches the reported value [84]. Unlike the plasmonic imaging method, which is difficult for measuring small molecules, the present mechanical amplification can detect both large and small molecules.

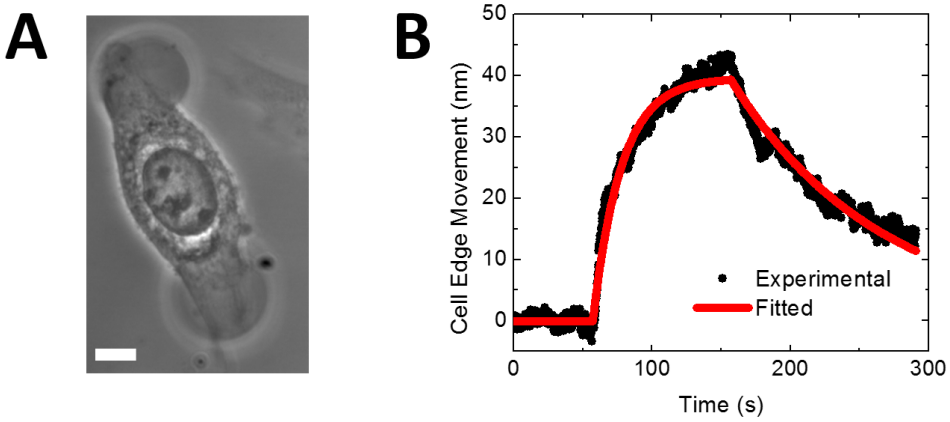

Figure 4.4 WGA and glycoprotein interactions in a live cell. (A) Phase contrast image of live SH-EP1 cell. Scale bar: 10 μm. (B) The average cell edge movement over the whole cell (black dots) and the fitting result (red curve) for 20 μg/ml WGA binding. By fitting the data with the first order kinetics, the association rate constant (k_{on}), dissociation rate constant (k_{off}), and dissociation constant (K_D) were found to be $k_{on} = 1.0 \times 10^4\ M^{-1}s^{-1}$, $k_{off} = 1.3 \times 10^{-3}\ s^{-1}$ and $K_D = 0.13\ \mu M$.

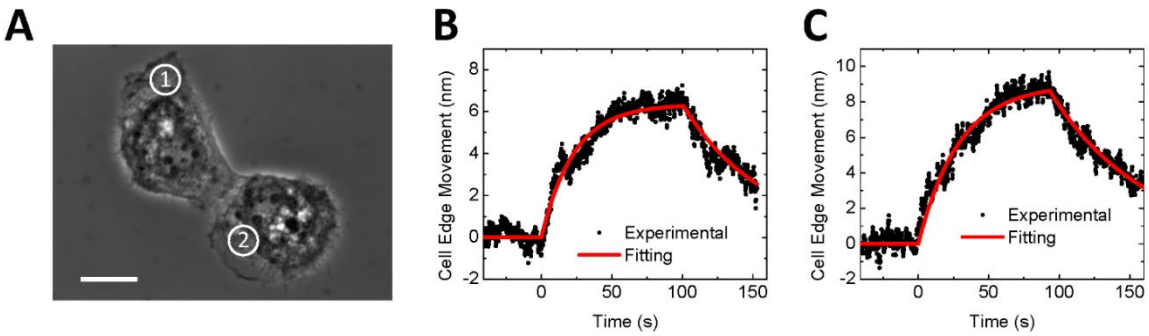

Figure 4.5 Anti-EGFR antibody interaction with EGFR in cells. (**A**) Phase contrast image of fixed A431 cells, where the numbers mark the cells under analysis. Scale bare: 20 μm. (**B**) and (**C**) Averaged cell edge movement over the whole cell (black dots) for cells 1 (**B**) and 2 (**C**) respectively (10 nM anti-EGFR antibody). The red curves are fitting results according to the first order kinetics. The association rate constant (k_{on}), dissociation rate constant (k_{off}) and dissociation constant (K_D) were found to be $k_{on} = 2.62 \times 10^6\ M^{-1}s^{-1}$,

$k_{off} = 1.73 \times 10^{-2}\ s^{-1}$ and $K_D = 6.6\ nM$ for cell 1, $k_{on} = 1.97 \times 10^{6}\ M^{-1}s^{-1}$, $k_{off} = 1.50 \times 10^{-2}\ s^{-1}$ and $K_D = 7.6\ nM$ for cell 2, respectively.

4.5 Acetylcholine and Nicotinic Acetylcholine Receptors (nAChRs) Interaction

In order to demonstrate small molecule binding detection capability with the present method, we studied the binding of acetylcholine with nicotinic acetylcholine receptors (nAChRs) using engineered SH-EP1 cells that expressed human α4β2 receptors. nAChRs are among the most studied membrane receptors because of their critical role in neurotransmission and nicotine addiction [85, 86]. Determining the binding kinetics of neurotransmitters, such as acetylcholine, with nAChR in neurons is important for basic neuroscience, and for the clinical evaluation of nicotine addiction [87]. The neurotransmitter-receptor binding affinity cited in textbooks and literature was obtained with the radioactive labeling method, which requires lysis of the neurons [88], and incubation with the neurotransmitters, which cannot measure the binding affinity of each individual cells. Because radioactive or other labeling methods are end point assays, they do not provide kinetic constants.

The human α4β2 transfected human epithelial SH-EP1 cells were cultured in a humidity incubator at 37˚C with 5% CO2 and 70% relative humidity. Dubelco's Modified Eagle's Medium (DMEM, Lonza, Walkersville, MD) with 10% Fetal Bovine Serum (FBS, Life Technologies, Carlsbad, CA) and penicillin-streptomycin (BioWhittaker, Basel, Switzerland) were used as culture medium. SH-EP1-h α4β2 cells were cultured in 25 cm^2 flask until approximately 80% confluence was reached for passage. 0.05% trypsin-EDTA (Life Technologies, Carlsbad, CA) was used for cell passage. For experiments, cells were treated same as CP-D cells described in section 4.4.

The image of SH-EP1-hα4β2 cells is shown in Figure 4.6A, where the white arrow marks the cell under analysis. 1X PBS buffer was first introduced to flow over the cell for 25 s, and then the buffer was switched to an acetylcholine solution in 1X PBS. After association, the acetylcholine solution at each concentration was switched back to 1X PBS to allow for dissociation. The above procedure was repeated for different acetylcholine concentrations. As shown in Figure 4.6B, the cell edge expands during the association phase and retracts during the dissociation phase. Figure 4.5B also shows that the amount of cell expansion during the association process increases with the acetylcholine concentration, which is expected for first-order binding kinetics. The association (k_{on}) and dissociation (k_{off}) rate constants were found to be $1.2 \times 10^{-6}\ M^{-1}s^{-1}$ and $2.2 \times 10^{-2}\ s^{-1}$, respectively, which represent the first direct measurement of the kinetic constants for the binding of the neurotransmitter to the nAChRs in intact cells. From k_{on} and $k_{off,}$ the equilibrium dissociation constant ($K_D = k_{off}/k_{on}$) was determined to be $18.1\ nM$. By plotting the equilibrium response versus acetylcholine concentrations (Figure 4.6C), the equilibrium constant (K_D) was found to be $\sim 26\ nM$, which is consistent with that obtained by kinetics measurement. As this is the first kinetic measurement of acetycholine binding to nAChRs, we cannot compare our findings to other reference technologies or prior data. However, the equilibrium dissociation constant determined here is in good agreement with the average K_i determined with radioligand binding assay, which involved centrifuge and formation of cell pellets [88, 89].

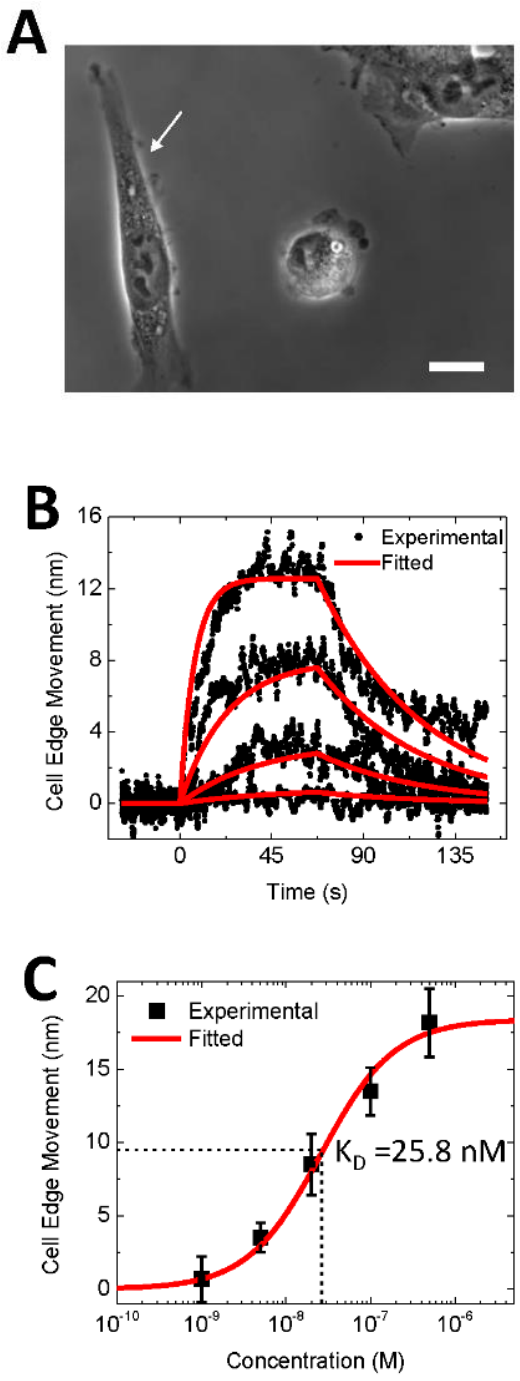

Figure 4.6 Small molecule interactions: Acetylcholine interaction with nicotinic acetylcholine receptors in cells. (A) Phase contrast image of the fixed human α4β2 transfected SH-EP1 cells, where the white arrow marks the cell under analysis. Scale bar: 20 μm. (B) Averaged cell edge movement over the whole cell (black dots) and global fitting

results (red curves) during the binding process for acetylcholine of different concentrations (from bottom to top: 1 nM, 5 nM, 20 nM, and 100 nM). (C) Cell edge movement at equilibrium vs. acetylcholine concentration. The equilibrium constant (K_D) was determined to be ~26 nM by fitting the data with the Langmuir isotherm.

As a control experiment, we carried out the measurement with wild type SH-EP1 cells, which do not have nAChRs expressed on the cell surfaces, and observed no deformation in the cell membrane (Figure 4.7). The expression levels of nAChRs in the engineered and wild type cells were confirmed with immunofluorescence imaging. The engineered cells were incubated with both primary and Alexa Fluor 488 labeled secondary antibodies. The typical phase contrast and immunofluorescence images of the engineered SH-EP1 cells are shown in Figure 4.8 A and D. Negative control was carried out by incubating the wild type SH-EP1 cells with primary and secondary antibodies (Figure 4.8 B and E). Another negative control was performed by incubating the engineered SH-EP1 cells with only secondary antibody (Figure 4.8 C and F). There are a little fluorescence signals in both negative controls, which confirms high coverage of nAChRs in the SH-EP1-hα4β2 cells. These results demonstrated that the mechanical deformation in the engineered SH-EP1 cells was indeed due to the specific binding of acetylcholine to the expressed nAChRs.

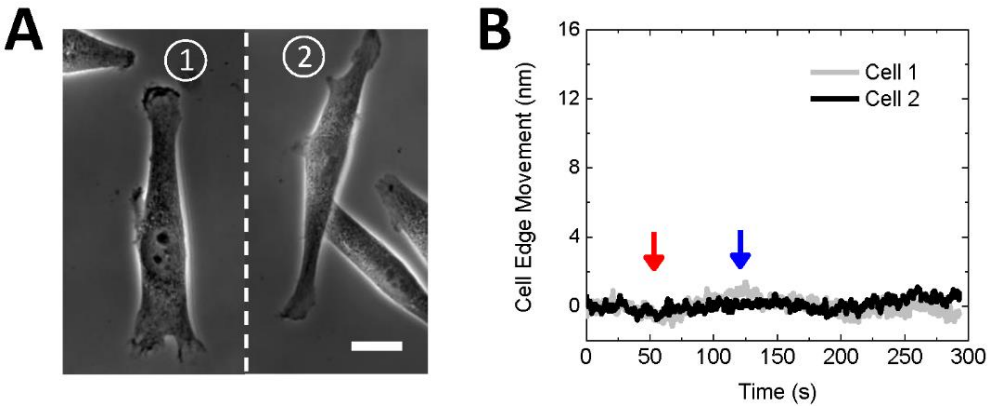

Figure 4.7 Negative control. (A) Phase contrast images of wild type SH-EP1 cells. Scale bar: 20 μm. (B) Response of wild type SH-EP1 cells to 500 nM acetylcholine. The red arrow marks the switch from 1x PBS to 500 nM acetylcholine and the blue arrow indicates the change of solution back to 1x PBS.

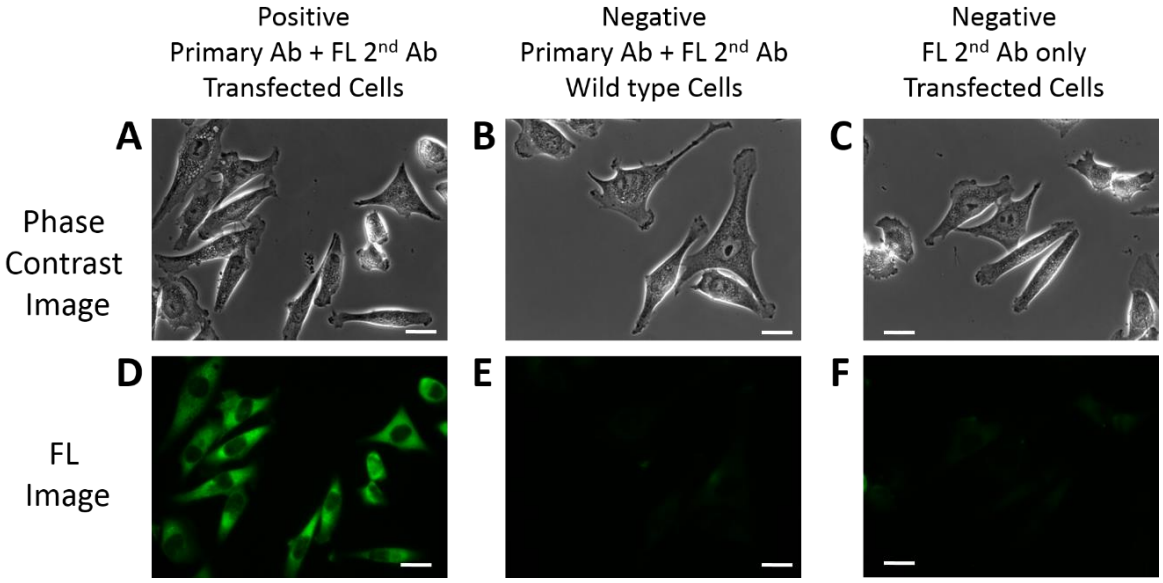

Figure 4.8 Phase contrast (A – C) and immunofluorescence (D – F) images of nAChRs positive and negative cells. Positive control was performed by sequentially incubating human α4β2 transfected SH-EP1 cells with primary and secondary antibodies (**A** and **D**). First negative control was followed the same procedure with the wild type SH-EP1 cells (**B** and **E**). Second negative control was performed by incubating the human α4β2 transfected SH-EP1 cells with secondary antibody only (**C** and **F**). Scale Bar: 20 μm.

Table 4.1 Association rate constants (k_{on}), dissociation rate constants (k_{off}), and equilibrium constants (K_D) for four cells as shown in Figures 4.9 A to D.

	k_{on} $(M^{-1}s^{-1})$	k_{off} (s^{-1})	K_D (nM)
Cell 1	7.32×10^5	0.0161	22.0
Cell 2	8.33×10^5	0.0217	26.1
Cell 3	3.42×10^5	0.0298	87.1
Cell 4	5.76×10^5	0.0172	29.9

The present method can not only to quantify the binding kinetics of small molecule interactions with membrane proteins in single cells, but also examine the cell-cell variations in the binding kinetics. Figures 4.9 A and C are the phase contrast images of SH-EP1-hα4β2, where the numbers in circles mark the cells under analysis. Cells 1 and 2 were cultured on one glass slide, and cells 3 and 4 on a second glass slide. The responses of these cells to 100 nM acetylcholine are shown in Figures 4.9 B and D, and the corresponding kinetic constants are given in Table 4.1, which show significant differences in the binding kinetics among the cells. The method also allows us to examine the binding kinetics at different regions of the same cell. Figure 4.9E plots the binding kinetic curves of acetylcholine to nAChRs at various locations of a cell, which shows large variations in the binding kinetics. Figure 4.9F shows the maximum membrane deformation along the edge of a cell, where the color represents the deformation in nm. Heterogeneous distribution of membrane protein receptors in cells play important roles in cellular functions, including interactions between different cells [74, 75].

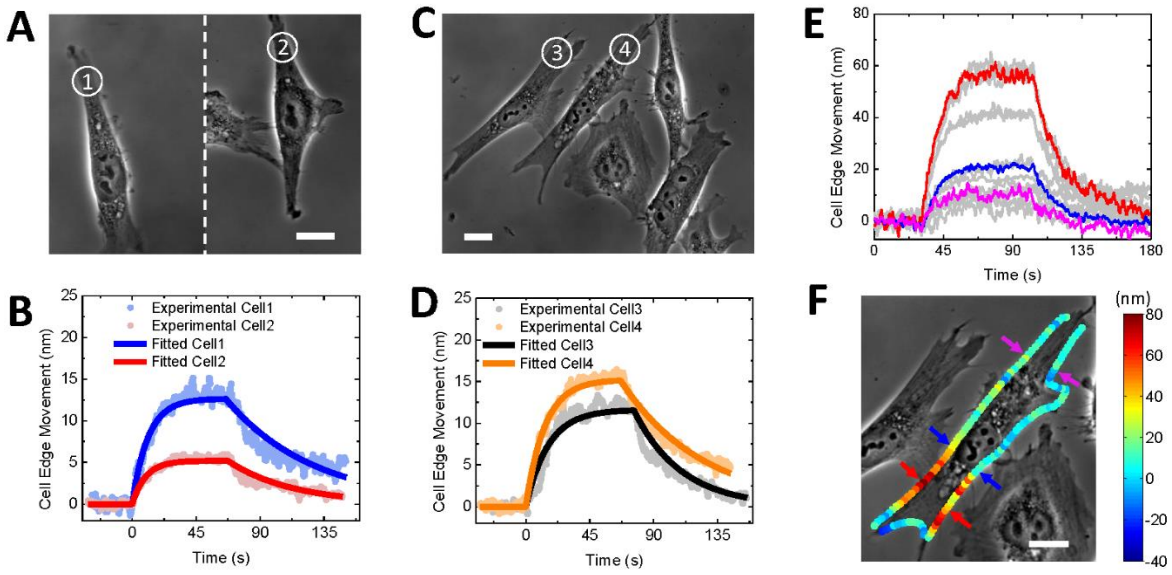

Figure 4.9 Heterogeneity of small molecule interactions with cell membrane receptors. (A and C) Phase contrast images of fixed human α4β2 transfected SH-EP1 cells, where the numbers mark different cells under analysis. Scale bar: 20 μm. (B) Binding kinetics of cells 1 and 2 (100 nM Acetylcholine). (D) Binding kinetics of cells 3 and 4 (100 nM Acetylcholine). (E) Binding kinetics at different locations of cell in f (100 nM Acetylcholine). (F) Phase contrast image of fixed human α4β2 transfected SH-EP1 cell. The color represents the amount of cell membrane edge deformation. Scale bar: 20 μm.

4.6 Discussion

The importance of studying molecular interactions with membrane proteins has motivated many efforts to develop label-free detection technologies for real time analysis of the interaction kinetics. Examples include quartz crystal microbalance [90] and surface plasmon resonance (SPR) techniques [76]. However, the signals of both methods are proportional to the mass of the molecule, making them difficult to measure the kinetics of small molecule interactions with membrane proteins. To our knowledge, this work is the first direct and real-time measurement of the binding kinetics of small molecules with

membrane proteins in intact cells without labeling. The method is based on the law of thermodynamics, which is general and applicable to analyzing the interactions of both large and small molecules with membrane proteins.

In addition, mechanical amplification and the sub-nm resolution offered by the differential detection algorithm provide sensitive detection of molecular binding in single cells. The sub-nm scaled detection limit can be further improved by removing noise from different sources. Figure 4.10 shows the noise power spectrum of the cell edge movement of a cell. At low frequencies (< 10 Hz), the power spectrum can be fitted with a linear function with a slope close to -2, indicating Brownian motion as the major source of noise. However at higher frequencies, it deviates significantly from the Brownian noise behavior, which shows noise from other sources, such as light source and camera, become important.

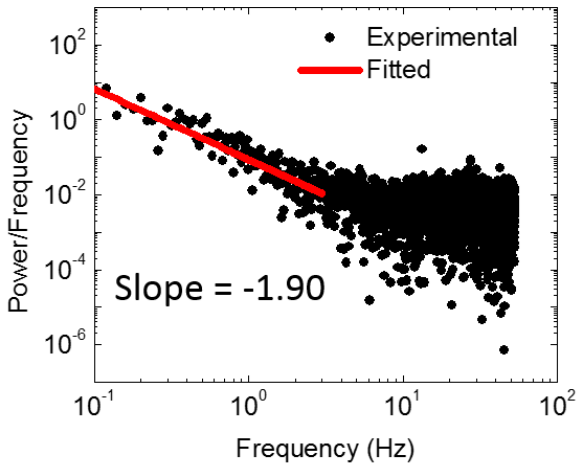

Figure 4.10 Noise power spectrum of cell edge movement of a fixed CP-D cell. The cell edge movement was measured with the differential detection algorithm. The slope at low frequencies is close to -2, as expected for Brownian motion.

The spatial resolution at single cell level allows us to quantify not only cell-to-cell variability in the binding kinetics (Figures 4.9 A to D), but also region-to-region difference

within a single cell. For example, Figure 4.9 F shows relative larger binding signals of a cell in the regions where the cell interacts with a neighboring cell (red color in Figure 4.9 F). Similarly, the corresponding regions of the neighboring cell also show larger binding signals then other regions (Figure 4.11 A). This phenomenon has also been observed in other cells (Figure 4.11 B).

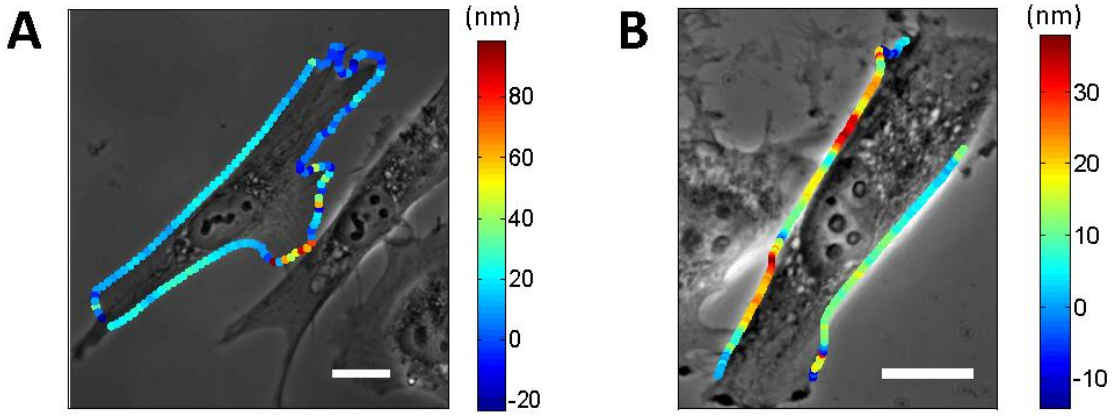

Figure 4.11 Molecular binding-induced membrane deformation along cell edges. (A) Phase contrast image of fixed human α4β2 transfected SH-EP1 cell adjacent to the cell in Fig. 4F. (B) Phase contrast image of fixed human α4β2 transfected SH-EP1 cell. Color represents the amount of cell membrane deformation after acetylcholine binding. Scale bar: 20 μm.

Finally, the method is based on optical microscopy, which is simple and compatible with various optical imaging techniques, including fluorescence imaging. These capabilities will benefit the screening of the drugs, and understanding of various cellular processes that involve membrane proteins. The latter is especially important because as the number of 3D structures of membrane proteins increases exponentially, studying the interaction kinetics of molecules with the membrane proteins becomes increasingly important.

CHAPTER 5

REAL TIME MONITORING GRANULE RELEASE BY MEASURING PLASMA MEMBRANE DEFORMATION

5.1 Introduction

One way of cellular communication is regulated exocytosis. In nerve systems, signals are transmitted from one neuron to another by the neurotransmitters released from pre-synapses to the post-synapses through regulated synaptic vesicles exocytosis. When an action potential depolarizes the presynaptic plasma membrane, Ca^{2+} channels open, and the influx of Ca^{2+} results in the elevation of Ca^{2+} concentration, thus triggering the exocytosis of synaptic vesicles [91, 92]. Vesicles release the neurotransmitters into the synaptic cleft, and then are captured by receptors on the post-synapses, thus initiating a sequence of downstream reactions [93]. Vesicle exocytosis mainly takes two forms, full fusion or "kiss and run" [94-96]. In full fusion, vesicles fuse with plasma membrane and fully collapse into plasma membrane, leading to an increase in plasma membrane area. Vesicles also transiently fuse with plasma membrane and release their neurotransmitter, after which the vesicles retrieve for reuse. In immune system, mast cells which contain granules rich in histamine, serotonin and heparin play an important role in a variety of allergic, asthmatic and inflammatory reactions [97, 98]. Mast cells express high affinity immunoglobulin E (IgE) receptors (FcεRI) on cell surfaces which can be sensitized after IgE binding [99]. Upon specific antigens binding to FcεRI bound IgE, a signaling cascade initiates including the degranulation, which is the secretory of characteristic granules of mast cells [100]. Granules dock at the plasma membrane and when degranulation is activated, granules fuse with plasma membrane which results in histamine, serotonin,

heparin and other inflammatory mediators releasing into extracellular solution which causes characteristic symptoms of an allergic reaction.

At present, exocytosis is mainly studied by electrophysiological recording and fluorescence imaging at the single cell level [101, 102]. Capacitance measurements by single cell patch clamp are based on the fact that exocytosis increases the plasma membrane because of fusion of vesicles or granules, which thus increases the plasma membrane capacitance [103, 104]. Capacitance measurements is limited by taking the overall effects of exocytosis on the whole cell and thus cannot pin out the exact release location. Another way is to record the oxidation current of electric active chemicals released from vesicles or granules. A carbon microelectrode a constant potential is placed close to the cell membrane to monitor exocytosis [105-108]. When there is exocytosis, the released chemicals, for example dopamine or histamine, are oxidized at the electrode and thus the oxidization currents are recorded showing spikes in the signal. Amperometric measurements monitor the release of secretory products and is limited on measuring vesicles or granules containing electric active compounds. Individual exocytosis has also been studied by fluorescence imaging [109]. Some pH sensitive dyes [110-112] (for example, Acridine Orange, FITC-dextran) accumulate inside the acidic vesicles. When the fusion between the vesicle membrane and plasma membrane happens during the exocytosis, the dyes inside the vesicles are exposed to the neutral pH extracellular medium. This exposure will relieve the low-pH quenching dyes in the lumen of secretory vesicles and thus resulting in bright spot in fluorescent image. Fluorescent styryl FM dye has been used to track exocytosis, endocytosis and label firing neurons [109, 113, 114]. FM dye is virtually nonfluorescent in aqueous solution, while it is intensively fluorescent when inserted in plasma membrane.

Fluorescence imaging suffers the low temporal resolution because of photo bleaching of fluorophores.

Here I used the RBL-2H3, a rat basophilic leukemia cell line as the model system to study degranulation process. I report an observation of mechanical deformation of cell plasma membrane during the granule exocytosis triggered by antigen and IgE interactions, and demonstrate a capability of real time analysis of granule release by tracking the cell edge and the deformation propagation from the granule release location to cell edge. I have directly observed the plasma membrane mechanical response after degranulation is activated. Using this capability, I have monitored the granule release and mapped the cell membrane deformation caused by the granule fusion. The cell membrane deformation has been confirmed to be related by granule release by simultaneous fluorescence recording. Temporal and spatial correlation of membrane deformation has been carefully analyzed. The delay between membrane deformation and fluorescence signal has been observed and explained. Granules diameters were calculated based on the measured cell edge expansion to be from 100 nm to 200 nm. This imaging capability allows me to analyze the spatial distribution of cell membrane deformation.

5.2 Materials and Methods

RBL-2H3, a basophilic leukemia cell line isolated and cloned from Wistar rat basophilic cells, has been used as a model system to study the IgE mediated degranulation of mast cells. RBL-2H3 cells were purchased from American Type Culture Collection (ATCC). RBL-2H3 cells were cultured in a humidity incubator at 37˚C with 5% CO_2 and 70% relative humidity. Eagle's Minimum Essential Medium (EMEM, ATCC 30-2003) with 15% heat inactivated Fetal Bovine Serum (FBS, Life Technologies, Carlsbad, CA)

and penicillin-streptomycin (BioWhittaker, Basel, Switzerland) were used as culture medium. RBL-2H3 cells were cultured in 25 cm^2 flask until approximately 80% confluence was reached for passage. 0.05% trypsin-EDTA (Life Technologies, Carlsbad, CA) was used for cell passage.

For experiment, cells were cultured overnight in 35 mm diameter tissue culture petri dish (Corning Inc., Corning, NY). The complete culture medium mentioned above together with 200 μM serotonin (Sigma-Aldrich, St. Louis, MO), 0.5 μg/ml monoclonal anti-Dinitrophenyl (anti-DNP) IgE (Sigma-Aldrich, St. Louis, MO) and 1 mg/ml fluorescein isothiocyanate-dextran (FITC-dextran, molecular weight 150,000, Sigma-Aldrich, St. Louis, MO) were used for culturing. Serotonin was used to increase the size of granule [115]. High affinity IgE receptors (FcεRI) are expressed on the cell surface to which anti-DNP IgE binds to. When the antigen, 2,4-dinitrophenylated albumin from bovine serum (DNP-BSA, Life Technologies, Carlsbad, CA) was added, the binding of DNP-BSA to anti-DNP IgE will make the cross-linking of FcεRI which initiates a signaling cascade leading to degranulation of the cells and release of chemical mediators. FITC-dextran accumulates inside the granules and are quenched by the weak acidic granule luminal solution. When degranulation is activated, the FITC-dextran is exposed to the neutral pH extracellular solution along with the released chemicals and thus the quenching is relieved giving a bright spot as fluorescence signal. Before measurement, the cells were rinsed three times with 0.1% BSA in extracellular buffer (135 mM NaCl, 5 mM KCl, 20 mM HEPES, 1.8 mM $CaCl_2$, 1 mM $MgCl_2$, 5.6 mM glucose, pH = 7.4) for three times to block the surface followed by another three times wash with extracellular buffer only. The petri dish with cells in 1 ml extracellular buffer was moved on the microscope for imaging. Recording

of both phase contrast and fluorescent images was right after addition of 1 ml 5 μg/ml DNP-BSA into the petri dish.

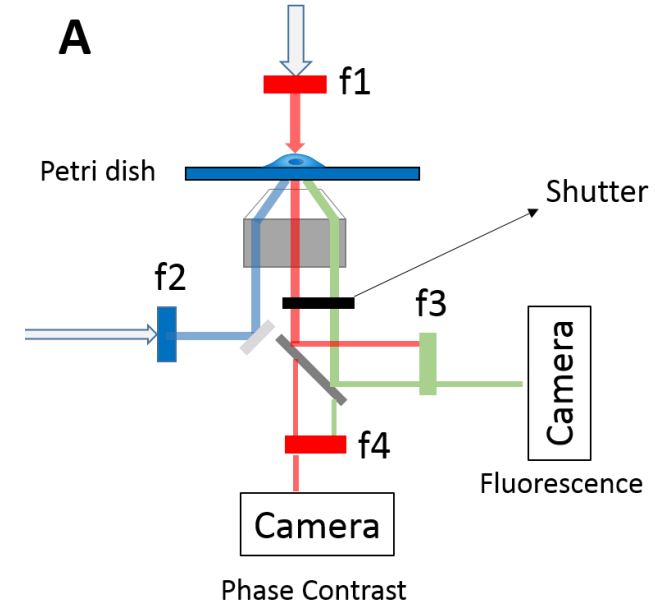

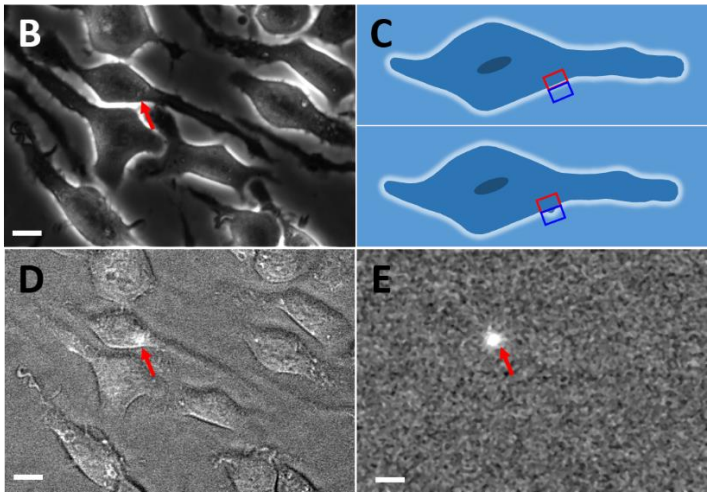

Figure 5. 1 Detection principle of granule release by tracking the edge deformation of cells. (A) Schematic illumination of the imaging setup based on an inverted phase contrast microscope with 40X phase 2 objective. A top light passes through a long pass filter with 600 nm cut-on wavelength (f1) and illuminates on sample cells. Phase contrast images are

recorded by a camera after another long pass filter with 600 nm cut-on wavelength (f4). A set of optical filters (excitation 420 nm – 480 nm (f2), emission 515 nm (f3)) is used for fluorescence imaging. A shutter is used to block both phase contrast and fluorescence light for synchronization. (B) Phase contrast image of RBL-2H3 cells. The red arrow marks the position where there is a granule release. (C) Illustration of cell edge changes during the granule release, measured by differential detection method. Red and blue rectangles are the region of interest for differential detection. (D) Fluorescence image of RBL-2H3 cells at the same location shown in (B). The bright spot pointed by the red arrow is due to the fluorescence from granule release. (E) The fluorescence image after the background subtraction. The bright spot pointed by the red arrow is due to a granule release. Scale bar: 10 μm.

An inverted microscope (Olympus IX81) equipped with a phase 2 condenser and phase 2 40X objective was used with illumination from the top of the sample cells (Figure 5.1A). Top illumination light pass through a long pass filter with 600 nm cut-on wavelength before illuminating on cell sample. The phase contrast image was recorded by a Hamamatsu camera with frame rate of up to 400 fps after another long pass filter with 600 nm cut-on wavelength. A set of optical filters (Ex420-480/Em515) was used for the fluorescence imaging and another Hamamatsu camera was used for recording with frame rate of 8 fps.

5.3 Phase Contrast and Fluorescence Simultaneous Recording and Optical Differential Detection

To investigate the plasma membrane behavior during the granules release, as well as to validate the release by fluorescence, the experimental setup based on an inverted optical

microscope was used (Figure 5.1A). Top illumination light pass through a long pass filter with 600 nm cut-on wavelength before illuminating on cell sample to avoid lighting up the fluorescence background. The phase contrast image was recorded after another long pass filter with 600 nm cut-on wavelength in order to eliminate the fluorescent signal in phase contrast image. A set of optical filters (Ex420-480/Em515) was used for the fluorescence imaging. With the modification of the microscope, the phase contrast image and fluorescence image are able to be obtained simultaneously of the same location. FITC-dextran was used as a reporter to validate the granule release. Figures 5.1 B and D show the phase contrast image and the corresponding fluorescence image at the same location, respectively. The edge of the cells can be clearly resolved with conventional phase contrast image (Figure 5.1B). To track the edge deformation, a rectangular region of interest (ROI) is defined such that the edge of a cell passes through the center of the rectangle. The rectangular ROI is divided into two equal halves, with one half inside of the cell and the other half outside of the cell (Figure 5.1C). We donate the intensities of the two halves as A and B. If the cell plasma membrane deforms (for example expanding) when granule releases, A will decrease, while B will increase (Figure 5.1C). The difference between A and B, (A-B)/(A+B), is used to determine the movement of the cell edge at each location. The calibration between (A-B)/(A+B) and the cell edge movement is determined experimentally. We refer to this method of detecting edge movement as differential optical detection. The differential detection rejects the common noise in optical system, thus providing high detection limit. The red arrows in both Figures 5.1 B and D point out the location where there is a granule release. The bright spot in Figure 5.1D is due to that the

elevated pH relieves low-pH quenched FITC in secretory granule when granule fuses with the cell plasma membrane during exocytosis.

To synchronize the phase contrast image and fluorescent image recording, a shutter is used to cut off the light path to black out both images (Figure 5.1A). By carefully aligning the intensity plots of fluorescent and phase contrast images, the two recordings are synchronized (Figure 5.2).

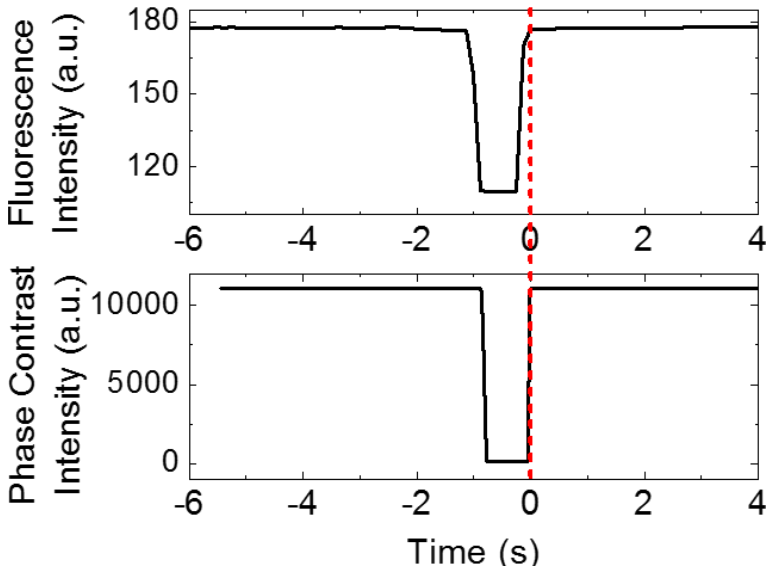

Figure 5.2 Synchronization between phase contrast and fluorescence recording. The shutter is used to block the light path of both fluorescence and phase contrast imaging. The time is aligned and synchronized when the shutter is removed.

5.4 Granule Release Measured By Tracking Cell Edge Deformation

To demonstrate the capability of tracking the cell plasma membrane deformation during granule exocytosis, the cells were first labeled by FITC-dextran and the release was triggered by DNP binding to anti-DNP IgE on cell surface. Figure 5.3A plots the edge deformation at the location marked by the black arrows in Figures 5.3 B to E, which are a

sequence of phase contrast images of the cell corresponding to the time marked by B, C, D and E in Figure 5.3A respectively. The cell edge expands very quickly and which shows a stepwise increase in edge tracking plot in Figure 5.3A. The total time for the cell plasma membrane expansion of ~ 18 nm is 0.18 s. Figure 5.3B shows the fluorescence intensity over time and the insert shows the cell fluorescent image with the bright spot marked by the white arrow which is due to the granule release. The fluorescent intensity increases sharply within 0.125 s because the granule fuses with the cell plasma membrane and thus the low-pH quenched FITC is exposed to the neutral pH extracellular medium which dequenches the dye. The gradual decrease in fluorescent intensity is due to the diffusion of FITC. Figures 5.3 G to J shows the fluorescent images after background subtraction before granule and plasma membrane fusion (Figure 5.3G), during fusion (Figure 5.3H), and the diffusion of FITC (Figures 5.3 I and J). Note that the time of the fluorescent signal peak is a little ahead of the plasma membrane expansion, we will come back to discuss this later.

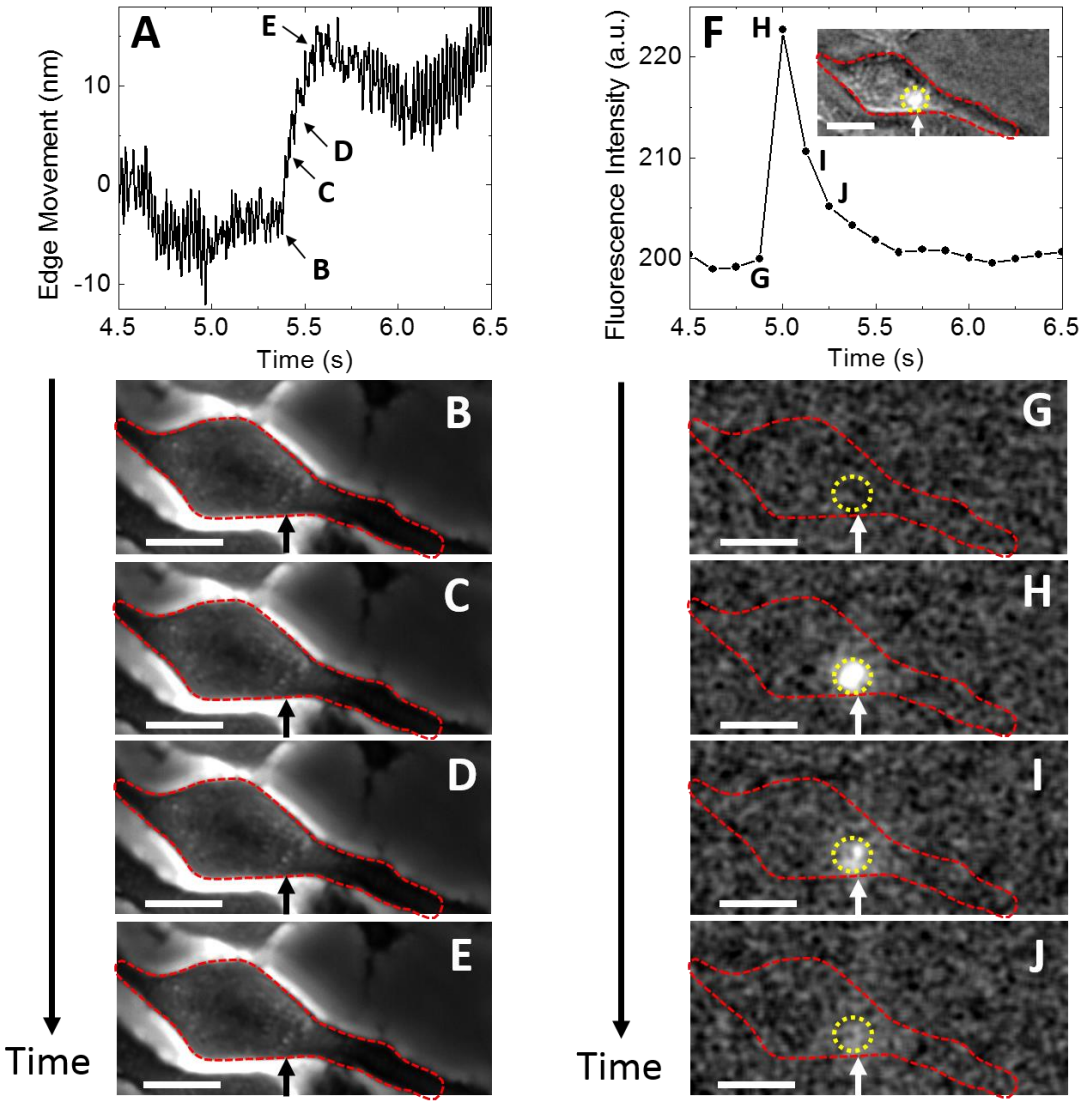

Figure 5.3 Principle demonstration: granule release measured by edge tracking and validated by fluorescence imaging. (A) Cell edge deformation over time at the location marked with the black arrows in (B-E) and white arrows in (G-J). (B-E) Snapshots of phase contrast images at the times marked by the letters B, C, D and E in figure (A), respectively. The red dashed lines depict the cell contour. (F) Fluorescence intensity within the region marked with yellow dashed circle in the inset and figures (G-J) is plotted over time. Inset: fluorescence image of the cell and the cell edge is depicted by red dashed line. The white

arrows in figures G-J and the black arrows in figures B-E are pointed to the same location of the cell. (G-J) Snapshots of fluorescence images of the cell after subtracting the background. The time of those images are marked by letters G, H, I and J in figure F, respectively. The red dashed lines depict the cell contour. Scale bar: 10 μm.

To confirm the observed membrane expansion is related to the granule release, we examined the membrane deformation at other locations along the cell edge during the same time period. Figure 5.4A shows the phase contrast image of the cell where B, C and D marks the location shown in Figure 5.4 B, C and D respectively. Only at the location where there shows the fluorescent signal the cell membrane expands (Figure 5.4C).

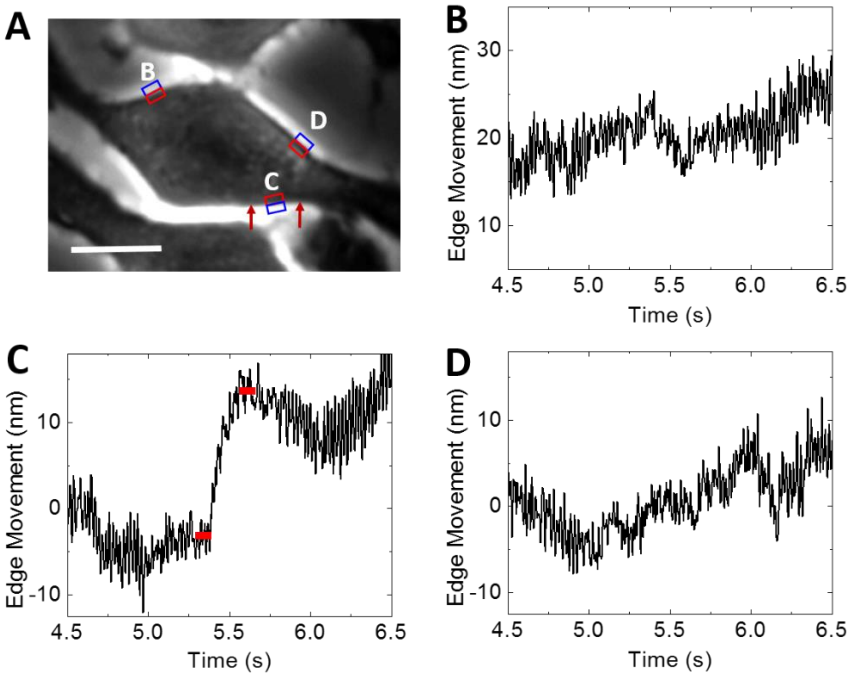

Figure 5.4 Cell edge movement tracking at different locations along the cell edge. (A) Phase contrast image of a RBL-2H3 cell. The blue and red rectangles are regions of interest (ROI) that mark the locations labeled by letter B, C, and D. (B-D) Cell edge movement at the locations marked by B, C and D, respectively. Scale bar: 10 μm.

5.5 Localized Cell Membrane Deformation Due to Granule Release

The image capability allows us to examine the how localized the cell membrane deformation is. Cell membrane expansion amounts from 5.25 s to 5.75 s (Figure 5.4C, difference between the two red lines) at different locations are calculated. Figure 5.5A is the phase contrast image of the cell under analysis. Figure 5.5B shows the deformation at different locations along the cell edge and the color represents the deformation in nm. The cell edge expands most at the location where there shows the fluorescent signal of granule release (bright spot in Figure 5.5C). To take a close look, the cell edge movement at locations between the two red arrows along the cell edge in Figure 5.5A are plotted in Figure 5.5C. The cell membrane expands differently with the variation of locations. Figure 5.5D plots the amount of stepwise membrane deformation along the cell edge marked by red arrows in Figure 5.5B. The location marked by the right red arrow is set to be zero shown in Figure 5.5D. The cell membrane expansion is distributed as that the larger responses are at the locations closer to the fluorescent signal (bright spot) and decays with the distance between the cell edge and fluorescent bright spot. The stepwise cell membrane expansion is localized to the cell edge closest to the fluorescent signal due to granule release, which supports the plasma membrane expands when the granules fuse with plasma membrane.

A sequence of snapshots of cell phase contrast images as well as the membrane deformation along the cell edge (represented by color) are shown in Figure 5.5 A. The cell edge deformation is compared to the original status set at time = 4.5 s. The membrane doesn't show clear deformation until time = 5.250 s. An expansion at the cell edge pointed by black arrow begins to show at time = 5.375 s and quickly become very obvious within

a short period of time (0.125 s). This expansion stays there though the total expansion region shrinks (time = 5.750 s and 6.000 s). Figures 5.6 B and C are the 3D and 2D plots respectively, showing the cell membrane deformation from time = 4.5 s to 6.3 s along the edge from red arrow to blue arrow pointing locations. The color in both figures represents the deformation in nm. At around 5.5 s, a reddish region appears which means the cell edge expands. Later on, the color becomes yellow which means the cell edge goes back a little but not completely to the baseline. Note that the reddish region also becomes narrow over time, which matches the observation that the expansion region shrinks.

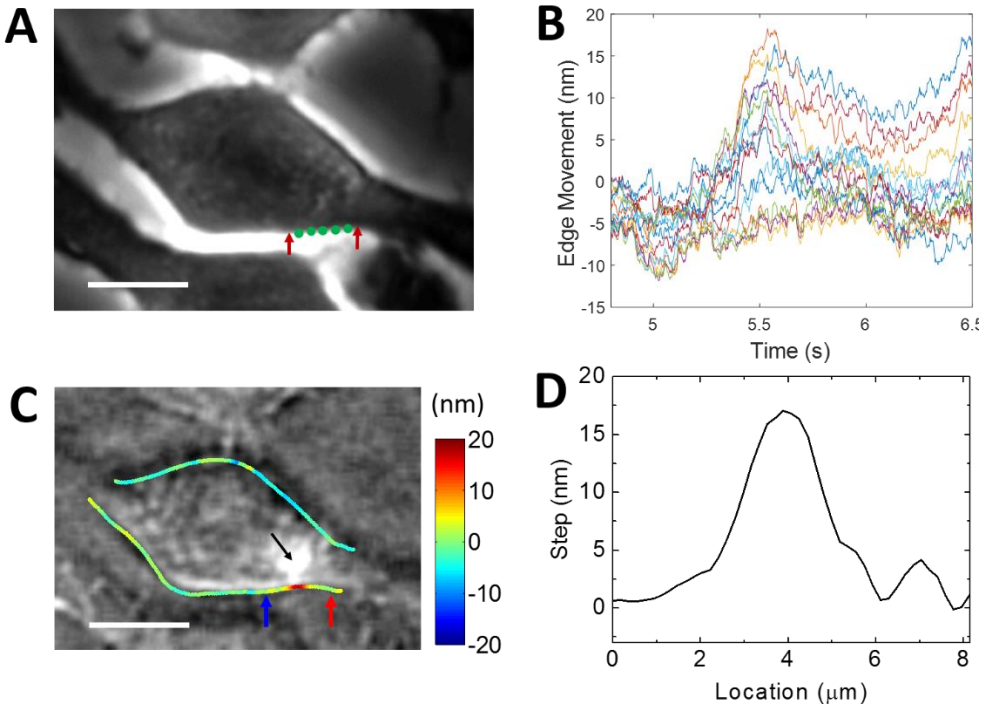

Figure 5.5 Local cell edge deformation caused by granule release. (A) Phase contrast image of RBL-2H3 cells. (B) The cell edge movement at different locations marked with green dots between two red arrows in figure (A). (C) Fluorescence image of granule release (location is pointed by the black arrow) in RBL-2H3 cell overlapped with corresponded local edge movement. The color represents the maximum amount of cell membrane edge

deformation in nm. (D) The cell membrane edge deformation in the region between the red and blue arrows in figure (C). Scale bar: 10 μm.

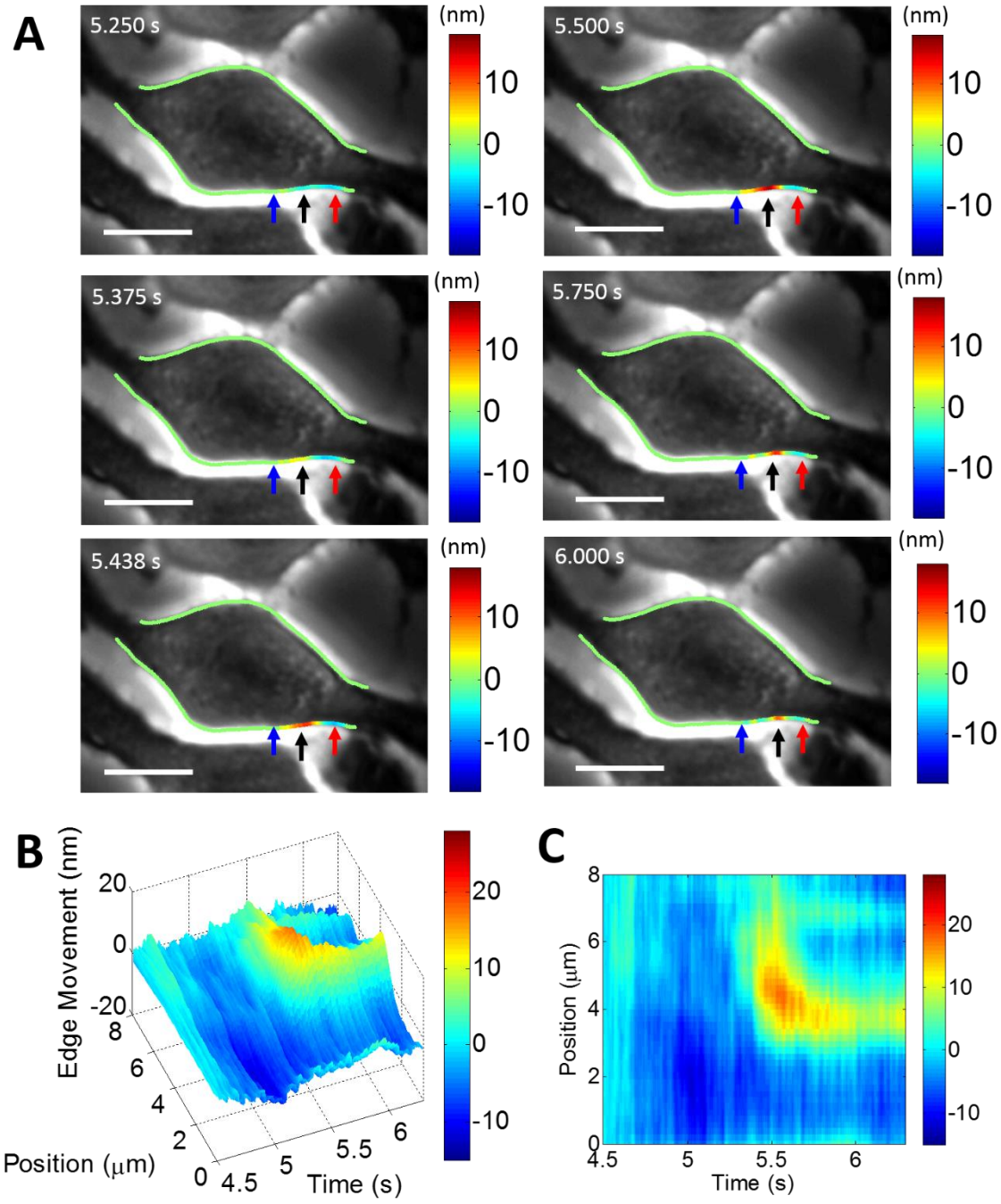

Figure 5.6 Real time cell membrane deformation distribution. (A) Phase contrast images of RBL-2H3 cell at different time overlapped with the cell membrane movement at

different locations. The color represents the amount of cell membrane deformation in nm. Black arrow indicates the location where the cell membrane shows most obvious change over time. (B) 3D plot of cell edge movement over time in the region marked between red and blue arrows in figure (A). The color represents the cell edge movement in nm. (C) 2D plot of cell edge movement with x axis in time, y axis in position corresponding to (B). The region are between the cell edges indicated by the red and blue arrows in (A). The color represents the cell edge change in nm. Scale bar: 10 μm.

5.6 Granule Release Location Dependent Time Delay

The simultaneous recording of phase contrast and fluorescent images allows us to examine the temporal relation between the cell membrane deformation and fluorescence signal. Figure 5.7 shows the cell membrane deformation and corresponding fluorescence signal of four different cells on different chips. Figures 5.7 E to H are the phase contrast images of the cells. Among these four cells, the cell membrane all expanded during the granule exocytosis and showed the stepwise increase in the cell edge tracking plot (Figures 5.7 A to D). The color in Figures 5.7 E to L represents the amount of stepwise increase along the edge in nm. The red color regions showing the expansion of the cell edge are localized to the bright spots of fluorescence signal (Figures 5.7 I to L). Note that the fluorescence peaks are always ahead of the plasma membrane expansion, however the ahead time varies among different cells. Figure 5.7A shows the longest time difference between the fluorescence signal peak and stepwise increase in edge deformation among the four cells, while Figure 5.7D shows the shortest time difference. Comparing the distances between the fluorescence bright spot center and maximum expansion location along the cell edge in Figures 5.7 I and L, it shows the longer distance in Figure 5.7 I gives

longer time difference in Figure 5.7A. To further investigate the distance dependent time delay, I plotted the time delay of membrane expansion to the fluorescence signal peak versus the distance between the fluorescence bright spot center and the largest expansion location along the cell edge (Figure 5.8). It shows very good linear relationship which confirms that the time delay is due the propagation of the effect of vesicle fusion to the cell edge.

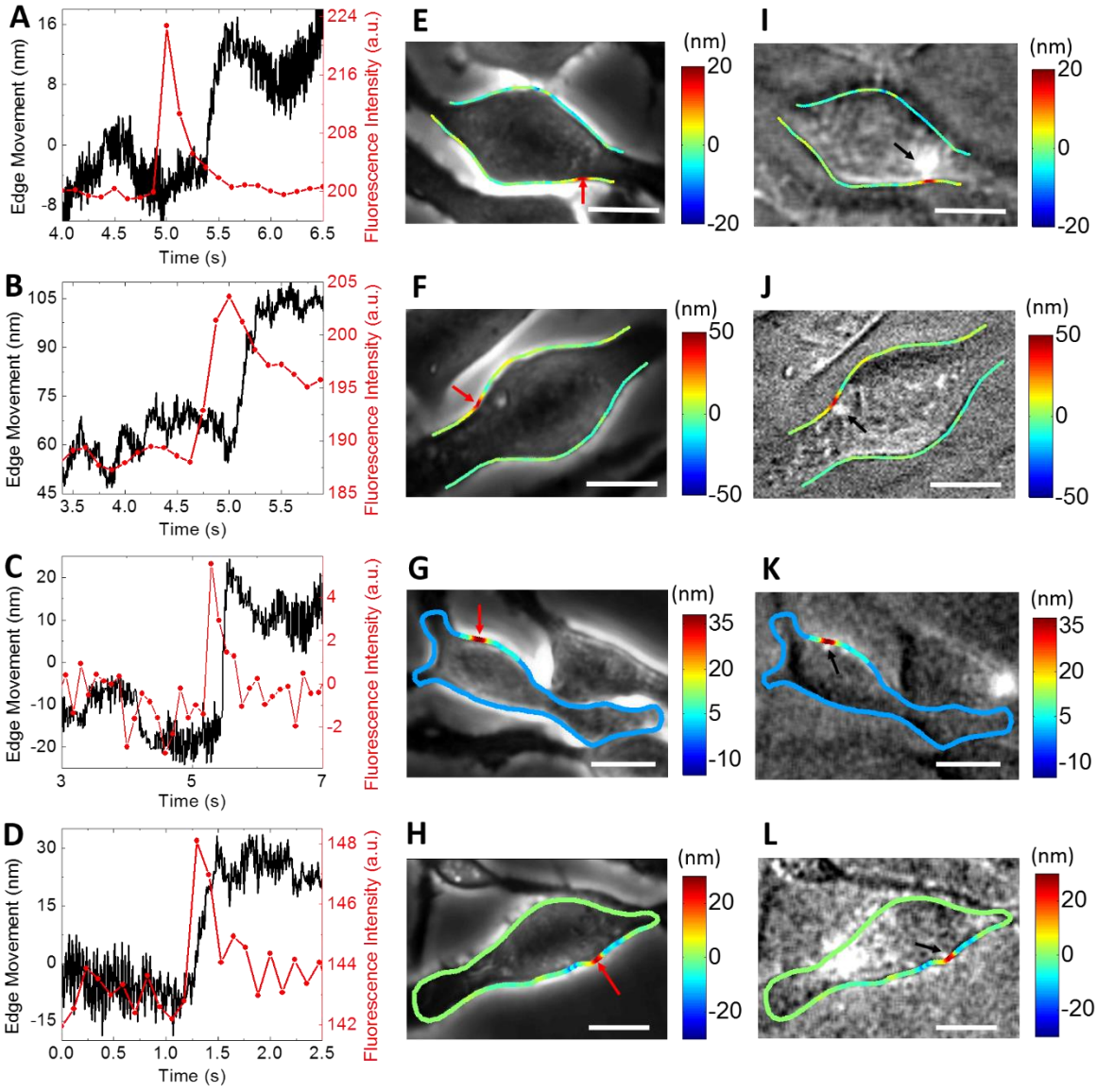

Figure 5.7 Cell edge deformation and corresponded fluorescence signal on different cells. (A-D) The cell edge movements and corresponded fluorescence signals caused by granule release from different RBL-2H3 cells. The corresponded phase contrast and fluorescence images are shown in E/I, F/J, G/K, and H/L, respectively. The red arrows in E-H indicate the locations of the edge movement plotted in A-D respectively. (E-H) Phase contrast images of RBL-2H3 cells overlap with corresponded local edge movement. The color represents the amount of cell membrane edge deformation at different locations in nm. (I-L) Fluorescence images of RBL-2H3 cells overlap with corresponded local edge movement. The color represents the amount of cell membrane edge deformation in nm. The granule release location is pointed out by black arrows in I-L. Scale bar: 10 μm.

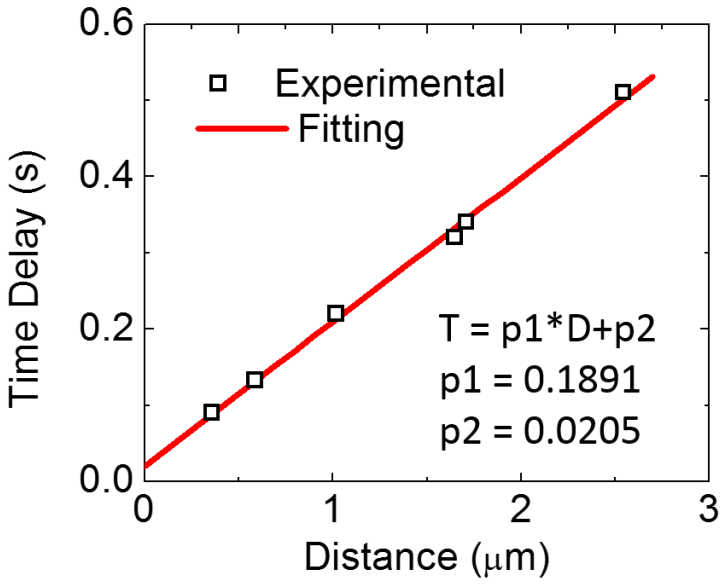

Figure 5.8 Granule release location vs. time delay. The locations of different granule release events are pin pointed from the fluorescence image (pointed by the black arrows in Fig. 5.7 I-L). Time delays between fluorescence signal and edge movement are measured from Fig. 5.7 A-D. The time delay linearly increases with the distance between granule

release location and cell edge. Squares are the experimental data and red line is the linear fitting.

5.7 Granule Release and Plasma Membrane Deformation

According to capacitance measurements, the cell membrane area increases due to the fusion of granule with cell plasma membrane [116]. A model has been built to explain the process during vesicle exocytosis in full fusion mode [117, 118]. A secretory vesicle docks at the plasma membrane and then an initial fusion pore forms. The vesicle luminal chemicals diffuse outside to the extracellular solution, and thus the surface tension at two connected membranes builds up. When the energy at the edge of the initially formed pore is overloaded, the initial fusion pore expands. Chemical messengers stored inside the vesicle are released to the extracellular solution and the vesicle membrane is incorporated with cell plasma membrane and thus losing its identity. The incorporation of the vesicle into the cell increases the cell plasma membrane which results in the expansion of cell edge. By tracking the cell edge, we can directly observe the cell deformation due to the granule membrane fused into the plasma membrane. I did observe the edge expansion as the model predicted. Figure 5.9 illustrates the membrane expansion during the granule fusion. Initially the secretory granule docks at the plasma membrane (Figure 5.9A). After degranulation is triggered by IgE antibody dimerization due to antigen binding to IgE on the cell surface, an initial fusion pore appears and the granule begins to fuse with plasma membrane more and more, thus increasing the area of plasma membrane leading to the expansion at the cell edge (Figures 5.9 B and C). When the granule is completely fused with plasma membrane, the cell edge expands to maximum (Figure 5.9D). This explains

the cell edge expansion and also predicts the delay of membrane edge expansion due to the propagation from the granule docking location to the membrane edge.

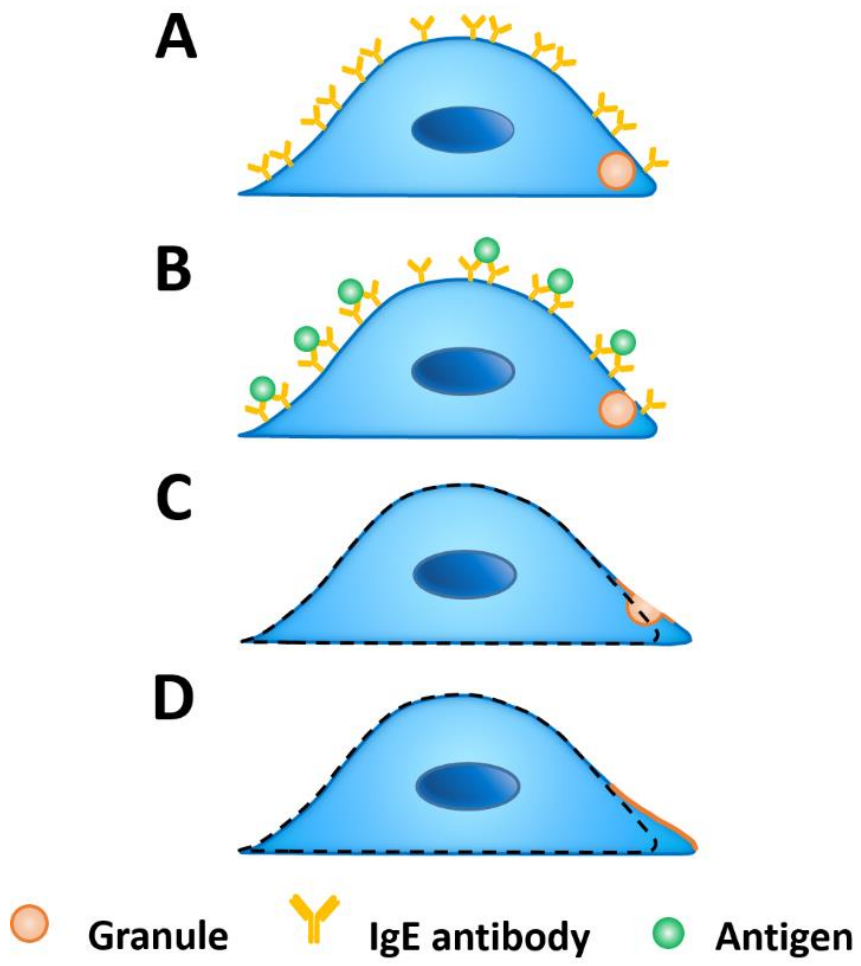

Figure 5.9 Schematic illumination of a granule release process and the corresponded plasma membrane expansion at different stages. (A) A granule docks at the plasma membrane. (B) An initial pore forms after the degranulation is triggered. (C) The initial pore expands and results in the cell membrane expansion because the extra membrane of granule immerges into cell plasma membrane. (D) The final cell shape after full fusion completes and the plasma membrane expands to maximum. Note that the membrane of and

from granule is showing with yellow color, and the dashed line in figure C and D indicates the original cell membrane position.

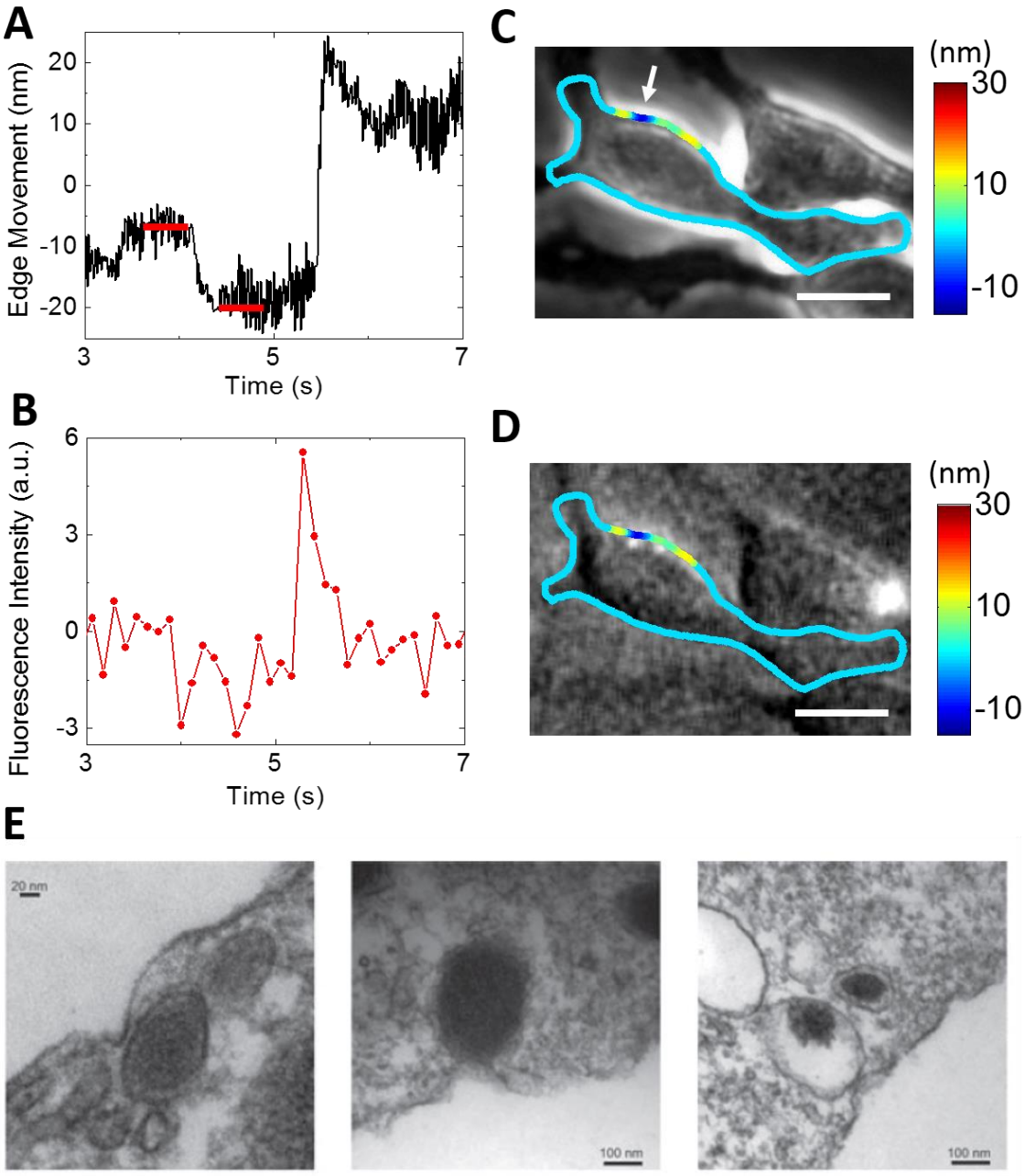

Figure 5.10 Plasma membrane indentation before granule fusion. (A) Cell Membrane edge moves over time. The white arrow in figure (C) indicates the location analyzed for the plot. A decrease in edge movement marked by two red lines is just ahead of granule

fusion. (B) Corresponded fluorescence signal of figure (A). (C) Phase contrast image of RBL-2H3 cell overlaps with the corresponded local edge movement. The color represents the membrane deformation amplitude between time t1 = 4 s and t2 = 4.5 s. (D) Fluorescence image of the same RBL-2H3 cell in (C). The color represents the membrane deformation amplitude between time t1 = 4 s and t2 = 4.5 s. (E) The SEM images show the plasma membrane indents when a granule comes to dock there. Figure E is from [119]. Scale bar: 10 μm.

I also observed that before the expansion of cell membrane, there is a decrease in cell edge deformation which means the indentation of cell membrane. The stepwise decrease along the cell edge is plotted in Figures 5.10 C and D, and color presents the cell membrane indentation in nm. Note that the indentation of cell edge is also localized to the location closest to the fluorescent signal of granule release (bright spot in Figure 5.10D). This phenomenon was also observed by SEM (Figure 5.10E [119]) that when granules are transported to dock at the plasma membrane, the cell membrane sometimes will dent. However this rarely happens and the mechanism is not clearly known.

5.8 Granule Size

The expanded edge is due to the granule membrane fusing with cell plasma membrane. To calculate the increased area, the maximum cell edge expansion was integrated along the cell edge. Also the volume of the granule was estimated by integrating the corresponding fluorescence signal over time. Granule area is proportional to r^2, and granule volume is proportional to r^3, where r is the granule radius. Figure 5.11A shows the $\sqrt{increased\ area}$ calculated from edge tracking in the relation of $\sqrt[3]{secretory\ volume}$ estimated by fluorescence signal, and it is fitted with linear relation. The diameter also

shows good linear relationship with $\sqrt[3]{secretory\ volume}$ (Figure 5.11B). The calculated diameters ranges between 100 nm to 250 nm which is slightly smaller than the literature reporting 500 nm [120]. This could be due to that the edge expansion calculated is from the 2D cell image projected from 3D cell.

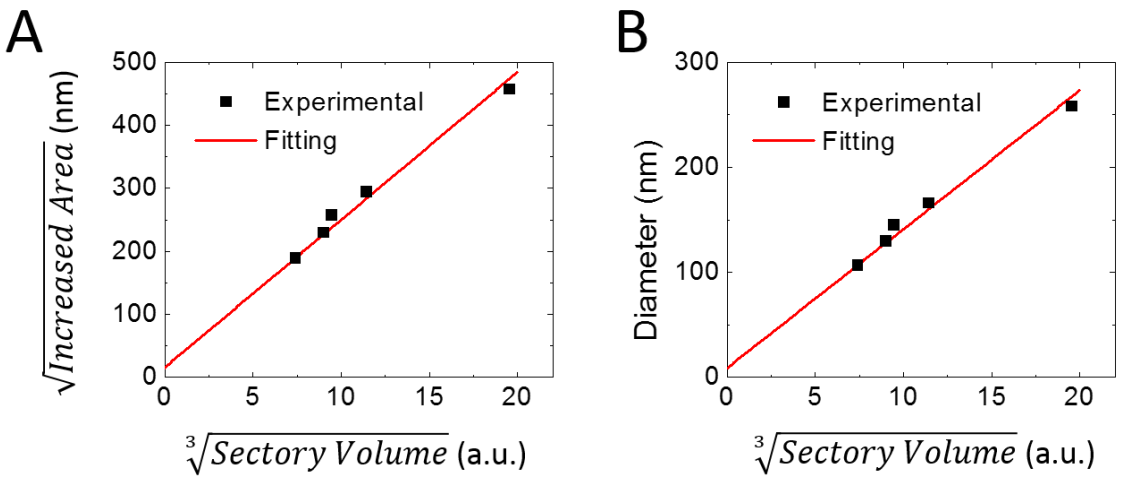

Figure 5.11 Correlation between edge expansion amplitude and fluorescence. (A) Square root of increase area calculated form edge tracking vs cube root of secretory volume estimated from fluorescence signal. Black square: experimental data. Red line: linear fitting. (B) Calculated granule diameter from edge tracking vs cube root of secretory volume estimated from fluorescence signal. Black square: experimental data. Red line: linear fitting.

5.9 Conclusion

I have demonstrated that by tracking the cell edge membrane deformation, I observed single granules release in single cells. Unlike fluorescence, amperometric and capacitance measurements, I directly observe the plasma membrane response to the granule fusion in real time with 2.5 ms time resolution and nm sensitivity. The pre-fusion indentation of plasma membrane when granule is transported to the membrane is also able to be imaged. With this edge tracking method, I can measure the membrane deformation distribution

along the cell edge which is due to the granule secretory. The time delay between fluorescence and cell edge deformation has been observed, which shows the membrane deformation propagation from the granule release location to the cell edge. The granules size is also estimated from the edge tracking signal.

This method provides a simple, label free way to monitor the exocytosis process. Focusing on plasma membrane mechanical deformation help understanding some basic characteristics of exocytosis besides the molecular study. This method is not limited to the cell types and is promising for label free study of synaptic vesicle release.

CHAPTER 6

CONCLUSIONS AND PERSPECTIVE

For the charge sensitive optical detection (CSOD), I have built the microscope based platform and demonstrated the capability of detection small molecules and proteins interactions. The next step is to realize the high-throughput capability of this method. CSOD is designed for high-throughput detection as it is compatible with microplate, which benefits the sample handling a lot. In order to achieve it, we are building a setup based on position sensitive diodes (PSD) to detect the optical fiber tip oscillation. By doing this, we can have 8 optical fibers as detection probes simultaneously detecting molecular interactions.

I have successfully detected small molecules interacting with membrane proteins by tracking cell membrane deformation. To our knowledge, it is the first time to real-time detect small molecule binding to membrane proteins *in situ*. Now the experiments were executed on fixed cells. The next step, first is to apply this method to live cells and even tissues. It is important because live cells and tissues are closer to the *in vivo* situation. Second, facing the situation that thousands or even hundreds of thousands chemical structures need to be screened in one day, it is essential to have high-throughput capability. Though now this image based method allows some throughput, it is not enough. To combine this method with flow cytometry will have large impact on both increasing throughput of this method and adding an extra parameter in flow cytometry measurement. Third, the accurate differential edge tracking method can be used to monitoring cell membrane deformation caused by other cellular activities, for example, exocytosis. When cells secrete vesicles, the vesicle membrane interacts with the cell plasma membrane, for

example, full fusion or kiss-and-run. These activities result in cell plasma membrane deformation. By tracking the plasma membrane change, we can detect the secretory process without labeling. Therefore we can detect the events with fast sampling rate without fluorescence limitation. The direct measurement of cell plasma membrane provides further understanding of cell exocytosis process.

I have demonstrated by tracking the cell plasma membrane deformation, I successfully observed the granule release from the cell. The pre-fusion indentation of plasma membrane when granule is transported to the membrane is also able to be imaged. With this edge tracking method, I can measure the membrane deformation distribution along the cell edge which is due to the granule secretory. The time delay between fluorescence and cell edge deformation has been observed, which shows the membrane deformation propagation from the granule release location to the cell edge. The size of the vesicle is also estimated from the edge tracking measurement. This is a label free imaging method, and the cell activities won't be affected by label molecules or extra perturbation. This method could be applied to detect the synaptic vesicle release in neural network.

REFERENCES

[1] M. R. Arkin and J. A. Wells, "Small-molecule inhibitors of protein-protein interactions: progressing towards the dream," *Nat Rev Drug Discov,* vol. 3, pp. 301-17, Apr 2004.

[2] M. A. Fabian, W. H. Biggs, 3rd, D. K. Treiber, C. E. Atteridge, M. D. Azimioara, M. G. Benedetti, *et al.*, "A small molecule-kinase interaction map for clinical kinase inhibitors," *Nat Biotechnol,* vol. 23, pp. 329-36, Mar 2005.

[3] J. P. Overington, B. Al-Lazikani, and A. L. Hopkins, "How many drug targets are there?," *Nat Rev Drug Discov,* vol. 5, pp. 993-996, 12//print 2006.

[4] A. Dove, "Drug screening[mdash]beyond the bottleneck," *Nat Biotech,* vol. 17, pp. 859-863, 09//print 1999.

[5] R. Macarron, M. N. Banks, D. Bojanic, D. J. Burns, D. A. Cirovic, T. Garyantes, *et al.*, "Impact of high-throughput screening in biomedical research," *Nat Rev Drug Discov,* vol. 10, pp. 188-95, Mar 2011.

[6] A. C. Pan, D. W. Borhani, R. O. Dror, and D. E. Shaw, "Molecular determinants of drug-receptor binding kinetics," *Drug Discov Today,* vol. 18, pp. 667-73, Jul 2013.

[7] R. A. Copeland, D. L. Pompliano, and T. D. Meek, "Drug-target residence time and its implications for lead optimization," *Nat Rev Drug Discov,* vol. 5, pp. 730-739, 09//print 2006.

[8] M. A. Cooper, "Label-free screening of bio-molecular interactions," *Anal Bioanal Chem,* vol. 377, pp. 834-42, Nov 2003.

[9] S. D. Gan and K. R. Patel, "Enzyme immunoassay and enzyme-linked immunosorbent assay," *J Invest Dermatol,* vol. 133, p. e12, Sep 2013.

[10] J. R. Heath and M. E. Davis, "Nanotechnology and Cancer," *Annual review of medicine,* vol. 59, pp. 251-265, 2008.

[11] L. Chen, H. Yin, B. Farooqi, S. Sebti, A. D. Hamilton, and J. Chen, "p53 α-Helix mimetics antagonize p53/MDM2 interaction and activate p53," *Molecular Cancer Therapeutics,* vol. 4, pp. 1019-1025, June 1, 2005 2005.

[12] Y. S. N. Day, C. L. Baird, R. L. Rich, and D. G. Myszka, "Direct comparison of binding equilibrium, thermodynamic, and rate constants determined by surface- and solution-based biophysical methods," *Protein Science,* vol. 11, pp. 1017-1025, 2002.

[13] J. Homola, "Surface Plasmon Resonance Sensors for Detection of Chemical and Biological Species," *Chemical Reviews,* vol. 108, pp. 462-493, 2008/02/01 2008.

[14] M. A. Cooper, "Optical biosensors in drug discovery," *Nat Rev Drug Discov,* vol. 1, pp. 515-528, 07//print 2002.

[15] X. D. Fan, I. M. White, S. I. Shopova, H. Y. Zhu, J. D. Suter, and Y. Z. Sun, "Sensitive optical biosensors for unlabeled targets: A review," *Analytica Chimica Acta,* vol. 620, pp. 8-26, Jul 2008.

[16] N. J. Tao, S. Boussaad, W. L. Huang, R. A. Arechabaleta, and J. D'Agnese, "High resolution surface plasmon resonance spectroscopy," *Review of Scientific Instruments,* vol. 70, pp. 4656-4660, 1999.

[17] R. Karlsson, M. Kullman-Magnusson, M. D. Hamalainen, A. Remaeus, K. Andersson, P. Borg, *et al.*, "Biosensor analysis of drug-target interactions: direct and competitive binding assays for investigation of interactions between thrombin and thrombin inhibitors," *Anal Biochem,* vol. 278, pp. 1-13, Feb 1 2000.

[18] P. O. Markgren, M. Hamalainen, and U. H. Danielson, "Screening of compounds interacting with HIV-1 proteinase using optical biosensor technology," *Analytical Biochemistry,* vol. 265, pp. 340-350, Dec 1998.

[19] H. Nordin, M. Jungnelius, R. Karlsson, and O. P. Karlsson, "Kinetic studies of small molecule interactions with protein kinases using biosensor technology," *Analytical Biochemistry,* vol. 340, pp. 359-368, May 2005.

[20] Z. R. Zhu and J. Cuozzo, "High-Throughput Affinity-Based Technologies for Small-Molecule Drug Discovery," *Journal of Biomolecular Screening,* vol. 14, pp. 1157-1164, Dec 2009.

[21] F. Touil, S. Pratt, R. Mutter, and B. N. Chen, "Screening a library of potential prion therapeutics against cellular prion proteins and insights into their mode of biological activities by surface plasmon resonance," *Journal of Pharmaceutical and Biomedical Analysis,* vol. 40, pp. 822-832, Mar 2006.

[22] S. Perspicace, D. Banner, J. Benz, F. Muller, D. Schlatter, and W. Huber, "Fragment-Based Screening Using Surface Plasmon Resonance Technology," *Journal of Biomolecular Screening,* vol. 14, pp. 337-349, Apr 2009.

[23] Y. T. Yang, C. Callegari, X. L. Feng, K. L. Ekinci, and M. L. Roukes, "Zeptogram-scale nanomechanical mass sensing," *Nano Letters,* vol. 6, pp. 583-586, Apr 2006.

[24] T. Braun, M. K. Ghatkesar, N. Backmann, W. Grange, P. Boulanger, L. Letellier, *et al.*, "Quantitative time-resolved measurement of membrane protein-ligand interactions using microcantilever array sensors," *Nature Nanotechnology,* vol. 4, pp. 179-185, Mar 2009.

[25] G. H. Wu, R. H. Datar, K. M. Hansen, T. Thundat, R. J. Cote, and A. Majumdar, "Bioassay of prostate-specific antigen (PSA) using microcantilevers," *Nature Biotechnology,* vol. 19, pp. 856-860, Sep 2001.

[26] J. Mertens, C. Rogero, M. Calleja, D. Ramos, J. A. Martin-Gago, C. Briones, *et al.*, "Label-free detection of DNA hybridization based on hydration-induced tension in nucleic acid films," *Nature Nanotechnology,* vol. 3, pp. 301-307, May 2008.

[27] J. Zhang, H. P. Lang, F. Huber, A. Bietsch, W. Grange, U. Certa, *et al.*, "Rapid and label-free nanomechanical detection of biomarker transcripts in human RNA," *Nature Nanotechnology,* vol. 1, pp. 214-220, Dec 2006.

[28] J. W. Ndieyira, M. Watari, A. D. Barrera, D. Zhou, M. Vogtli, M. Batchelor, *et al.*, "Nanomechanical detection of antibiotic mucopeptide binding in a model for superbug drug resistance," *Nature Nanotechnology,* vol. 3, pp. 691-696, Nov 2008.

[29] T. P. Burg, M. Godin, S. M. Knudsen, W. Shen, G. Carlson, J. S. Foster, *et al.*, "Weighing of biomolecules, single cells and single nanoparticles in fluid," *Nature,* vol. 446, pp. 1066-1069, Apr 2007.

[30] K. S. Novoselov, A. K. Geim, S. V. Morozov, D. Jiang, Y. Zhang, S. V. Dubonos, *et al.*, "Electric Field Effect in Atomically Thin Carbon Films," *Science,* vol. 306, pp. 666-669, October 22, 2004 2004.

[31] S. Roddaro, P. Pingue, V. Piazza, V. Pellegrini, and F. Beltram, "The Optical Visibility of Graphene: Interference Colors of Ultrathin Graphite on SiO2," *Nano Letters,* vol. 7, pp. 2707-2710, 2007/09/01 2007.

[32] P. Blake, E. W. Hill, A. H. Castro Neto, K. S. Novoselov, D. Jiang, R. Yang, *et al.*, "Making graphene visible," *Applied Physics Letters,* vol. 91, p. 063124, 2007.

[33] S. C. Gopinath and P. K. Kumar, "Biomolecular discrimination analyses by surface plasmon resonance," *Analyst,* vol. 139, pp. 2678-82, Jun 7 2014.

[34] C. Debouck and P. N. Goodfellow, "DNA microarrays in drug discovery and development," *Nat Genet*.

[35] B. Huang, M. Bates, and X. Zhuang, "Super resolution fluorescence microscopy," *Annual review of biochemistry,* vol. 78, pp. 993-1016, 2009.

[36] X. Shan, I. Diez-Perez, L. Wang, P. Wiktor, Y. Gu, L. Zhang, *et al.*, "Imaging the electrocatalytic activity of single nanoparticles," *Nat Nano,* vol. 7, pp. 668-672, 10//print 2012.

[37] J. A. Seibert, J. M. Boone, and K. K. Lindfors, "Flat-field correction technique for digital detectors," 1998, pp. 348-354.

[38] S. J. L. Gary P. Emerson, "Flat-Fielding for CCDs in AAVSO Observations, I," *JAAVSO,* vol. 27, p. 6, 1999.

[39] S. P. Wang, X. N. Shan, U. Patel, X. P. Huang, J. Lu, J. H. Li, *et al.*, "Label-free imaging, detection, and mass measurement of single viruses by surface plasmon resonance," *Proceedings of the National Academy of Sciences of the United States of America,* vol. 107, pp. 16028-16032, Sep 2010.

[40] X. N. Shan, K. J. Foley, and N. J. Tao, "A label-free optical detection method for biosensors and microfluidics," *Applied Physics Letters,* vol. 92, p. 3, Mar 2008.

[41] X. N. Shan, X. P. Huang, K. J. Foley, P. M. Zhang, K. P. Chen, S. P. Wang, *et al.*, "Measuring Surface Charge Density and Particle Height Using Surface Plasmon Resonance Technique," *Analytical Chemistry,* vol. 82, pp. 234-240, Jan 2010.

[42] T. Braun, M. K. Ghatkesar, N. Backmann, W. Grange, P. Boulanger, L. Letellier, *et al.*, "Quantitative time-resolved measurement of membrane protein-ligand interactions using microcantilever array sensors," *Nat Nanotechnol,* vol. 4, pp. 179-85, Mar 2009.

[43] A. K. Naik, M. S. Hanay, W. K. Hiebert, X. L. Feng, and M. L. Roukes, "Towards single-molecule nanomechanical mass spectrometry," *Nat Nanotechnol,* vol. 4, pp. 445-50, Jul 2009.

[44] S. H. Guan and R. B. Nielsen, "Rapid scan Fourier transform detection of a frequency encoded quartz crystal microbalance array," *Review of Scientific Instruments,* vol. 74, pp. 5241-5248, Dec 2003.

[45] J. Inglese, R. L. Johnson, A. Simeonov, M. Xia, W. Zheng, C. P. Austin, *et al.*, "High-throughput screening assays for the identification of chemical probes," *Nat Chem Biol,* vol. 3, pp. 466-79, Aug 2007.

[46] J. S. Daniels and N. Pourmand, "Label-Free Impedance Biosensors: Opportunities and Challenges," *Electroanalysis,* vol. 19, pp. 1239-1257, May 16 2007.

[47] K. J. Foley, X. Shan, and N. J. Tao, "Surface Impedance Imaging Technique," *Analytical Chemistry,* vol. 80, pp. 5146-5151, 2008/07/01 2008.

[48] J. Lu, W. Wang, S. Wang, X. Shan, J. Li, and N. Tao, "Plasmonic-based electrochemical impedance spectroscopy: application to molecular binding," *Anal Chem,* vol. 84, pp. 327-33, Jan 3 2012.

[49] X. Shan, U. Patel, S. Wang, R. Iglesias, and N. Tao, "Imaging Local Electrochemical Current via Surface Plasmon Resonance," *Science,* vol. 327, pp. 1363-1366, March 12, 2010 2010.

[50] F. Yan and O. A. Sadik, "Enzyme-Modulated Cleavage of dsDNA for Studying Interfacial Biomolecular Interactions," *Journal of the American Chemical Society*, vol. 123, pp. 11335-11340, 2001/11/01 2001.

[51] I. Bontidean, C. Berggren, G. Johansson, E. Csöregi, B. Mattiasson, J. R. Lloyd, *et al.*, "Detection of Heavy Metal Ions at Femtomolar Levels Using Protein-Based Biosensors," *Analytical Chemistry*, vol. 70, pp. 4162-4169, 1998/10/01 1998.

[52] S.-H. Chen, H.-N. Lin, and P.-M. Ong, "Spring constant measurement of a bent near-field optical fiber probe," *Review of Scientific Instruments*, vol. 71, p. 3788, 2000.

[53] M. Wilchek and E. A. Bayer, "INTRODUCTION TO AVIDIN-BIOTIN TECHNOLOGY," *Methods in Enzymology*, vol. 184, pp. 5-13, 1990.

[54] U. Böhme and U. Scheler, "Effective charge of bovine serum albumin determined by electrophoresis NMR," *Chemical Physics Letters*, vol. 435, pp. 342-345, 2007.

[55] M. Kneba, G. Krieger, A. Kehl, I. Bause, and G. A. Nagel, "CHROMATOFOCUSING COMBINED WITH THE ELISA TECHNIQUE - A SENSITIVE METHOD FOR THE ANALYSIS OF IMMUNE-COMPLEXES," *Journal of Immunological Methods*, vol. 61, pp. 233-243, 1983.

[56] R. Plattner, L. Kadlec, K. A. DeMali, A. Kazlauskas, and A. M. Pendergast, "c-Abl is activated by growth factors and Src family kinases and has a role in the cellular response to PDGF," *Genes & Development*, vol. 13, pp. 2400-2411, Sep 1999.

[57] B. J. Druker, M. Talpaz, D. J. Resta, B. Peng, E. Buchdunger, J. M. Ford, *et al.*, "Efficacy and safety of a specific inhibitor of the BCR-ABL tyrosine kinase in chronic myeloid leukemia," *New England Journal of Medicine*, vol. 344, pp. 1031-1037, Apr 2001.

[58] A. T. van Oosterom, I. Judson, J. Verweij, S. Stroobants, E. D. di Paola, S. Dimitrijevic, *et al.*, "Safety and efficacy of imatinib (ST1571) in metastatic gastrointestinal stromal tumours: a phase I study," *Lancet*, vol. 358, pp. 1421-1423, Oct 2001.

[59] R. J. Chen, H. C. Choi, S. Bangsaruntip, E. Yenilmez, X. W. Tang, Q. Wang, *et al.*, "An investigation of the mechanisms of electronic sensing of protein adsorption on carbon nanotube devices," *Journal of the American Chemical Society*, vol. 126, pp. 1563-1568, Feb 2004.

[60] P. G. Collins, K. Bradley, M. Ishigami, and A. Zettl, "Extreme oxygen sensitivity of electronic properties of carbon nanotubes," *Science*, vol. 287, pp. 1801-1804, Mar 2000.

[61] J. Kong, N. R. Franklin, C. W. Zhou, M. G. Chapline, S. Peng, K. J. Cho, *et al.*, "Nanotube molecular wires as chemical sensors," *Science,* vol. 287, pp. 622-625, Jan 2000.

[62] Y. Cui, Q. Q. Wei, H. K. Park, and C. M. Lieber, "Nanowire nanosensors for highly sensitive and selective detection of biological and chemical species," *Science,* vol. 293, pp. 1289-1292, Aug 2001.

[63] G. Zheng, F. Patolsky, Y. Cui, W. U. Wang, and C. M. Lieber, "Multiplexed electrical detection of cancer markers with nanowire sensor arrays," *Nat Biotechnol,* vol. 23, pp. 1294-301, Oct 2005.

[64] W. U. Wang, C. Chen, K. H. Lin, Y. Fang, and C. M. Lieber, "Label-free detection of small-molecule-protein interactions by using nanowire nanosensors," *Proc Natl Acad Sci U S A,* vol. 102, pp. 3208-12, Mar 1 2005.

[65] M. V. Salapaka, H. S. Bergh, J. Lai, A. Majumdar, and E. McFarland, "Multi-mode noise analysis of cantilevers for scanning probe microscopy," *Journal of Applied Physics,* vol. 81, p. 2480, 1997.

[66] X. Shan, S. Wang, and N. Tao, "Study of single particle charge and Brownian motions with surface plasmon resonance," *Appl Phys Lett,* vol. 97, p. 223703, Nov 29 2010.

[67] S. H. White, "Biophysical dissection of membrane proteins," *Nature,* vol. 459, pp. 344-346, 05/21/print 2009.

[68] P. Ehrlich, "Address in pathology on chemotherapeutics : Scientific principles, methods, and results," *Lancet,* vol. 2, pp. 445-451, 1913.

[69] A. L. Hopkins and C. R. Groom, "The druggable genome," *Nature Reviews Drug Discovery,* vol. 1, pp. 727-730, 2002.

[70] R. A. Copeland, D. L. Pompliano, and T. D. Meek, "Opinion - Drug-target residence time and its implications for lead optimization," *Nature Reviews Drug Discovery,* vol. 5, pp. 730-739, 2006.

[71] D. C. Swinney, "The role of binding kinetics in therapeutically useful drug action," *Current Opinion in Drug Discovery & Development,* vol. 12, pp. 31-39, 2009.

[72] R. E. Ernst, K. N. High, T. R. Glass, and Q. Zhao, "Determination of Equilibrium Dissociation Constants," in *Therapeutic Monoclonal Antibodies: From Bench to Clinic,* Z. An, Ed., ed Hoboken, NJ, USA: John Wiley & Sons, Inc., 2009.

[73] J. P. Changeux, "50 years of allosteric interactions: the twists and turns of the models," *Nat Rev Mol Cell Biol,* vol. 14, pp. 819-29, Dec 2013.

[74] V. Almendro, A. Marusyk, and K. Polyak, "Cellular heterogeneity and molecular evolution in cancer," *Annu Rev Pathol,* vol. 8, pp. 277-302, Jan 24 2013.

[75] C. E. Meacham and S. J. Morrison, "Tumour heterogeneity and cancer cell plasticity," *Nature,* vol. 501, pp. 328-37, Sep 19 2013.

[76] W. Wang, Y. Yang, S. Wang, V. J. Nagaraj, Q. Liu, J. Wu, *et al.*, "Label-free measuring and mapping of binding kinetics of membrane proteins in single living cells," *Nat Chem,* vol. 4, pp. 846-53, Oct 2012.

[77] H. Im, N. J. Wittenberg, A. Lesuffleur, N. C. Lindquist, and S. H. Oh, "Membrane protein biosensing with plasmonic nanopore arrays and pore-spanning lipid membranes," *Chem Sci,* vol. 1, pp. 688-696, Jan 1 2010.

[78] J. A. Maynard, N. C. Lindquist, J. N. Sutherland, A. Lesuffleur, A. E. Warrington, M. Rodriguez, *et al.*, "Surface plasmon resonance for high-throughput ligand screening of membrane-bound proteins," *Biotechnol J,* vol. 4, pp. 1542-58, Nov 2009.

[79] G. H. Wu, H. F. Ji, K. Hansen, T. Thundat, R. Datar, R. Cote, *et al.*, "Origin of nanomechanical cantilever motion generated from biomolecular interactions.," *Proc. Natl. Acad. Sci. USA,* vol. 98, pp. 1560-1564, 2001.

[80] S. E. Cross, Y. S. Jin, J. Rao, and J. K. Gimzewski, "Nanomechanical analysis of cells from cancer patients," *Nat Nanotechnol,* vol. 2, pp. 780-3, Dec 2007.

[81] V. Lulevich, C. C. Zimmer, H. S. Hong, L. W. Jin, and G. Y. Liu, "Single-cell mechanics provides a sensitive and quantitative means for probing amyloid-beta peptide and neuronal cell interactions," *Proc Natl Acad Sci U S A,* vol. 107, pp. 13872-7, Aug 3 2010.

[82] Y. Guan, X. Shan, S. Wang, P. Zhang, and N. Tao, "Detection of molecular binding via charge-induced mechanical response of optical fibers," *Chem Sci,* vol. 5, pp. 4375-4381, 2014.

[83] A. Dell and H. R. Morris, "Glycoprotein structure determination mass spectrometry," *Science,* vol. 291, pp. 2351-2356, 2001.

[84] Y. Zhou, A. L. Goenaga, B. D. Harms, H. Zou, J. Lou, F. Conrad, *et al.*, "Impact of intrinsic affinity on functional binding and biological activity of EGFR antibodies," *Mol Cancer Ther,* vol. 11, pp. 1467-76, Jul 2012.

[85] H. M. Schuller, "Is cancer triggered by altered signalling of nicotinic acetylcholine receptors?," *Nat Rev Cancer,* vol. 9, pp. 195-205, Mar 2009.

[86] A. Taly, P. J. Corringer, D. Guedin, P. Lestage, and J. P. Changeux, "Nicotinic receptors: allosteric transitions and therapeutic targets in the nervous system," *Nat Rev Drug Discov,* vol. 8, pp. 733-50, Sep 2009.

[87] E. X. Albuquerque, E. F. R. Pereira, M. Alkondon, and S. W. Rogers, "Mammalian nicotinic acetylcholine receptors: From structure to function," *Physiological Reviews,* vol. 89, pp. 73-120, 2009.

[88] J. B. Eaton, J. H. Peng, K. M. Schroeder, A. A. George, J. D. Fryer, C. Krishnan, *et al.*, "Characterization of human alpha 4 beta 2-nicotinic acetylcholine receptors stably and heterologously expressed in native nicotinic receptor-null SH-EP1 human epithelial cells," *Molecular Pharmacology,* vol. 64, pp. 1283-1294, Dec 2003.

[89] A. A. Jensen, I. Mikkelsen, B. Frolund, H. Brauner-Osborne, E. Falch, and P. Krogsgaard-Larsen, "Carbamoylcholine homologs: Novel and potent agonists at neuronal nicotinic acetylcholine receptors," *Molecular Pharmacology,* vol. 64, pp. 865-875, Oct 2003.

[90] Z. C. Pei, J. Saint-Guirons, C. Kack, B. Ingemarsson, and T. Aastrup, "Real-time analysis of the carbohydrates on cell surfaces using a QCM biosensor: a lectin-based approach," *Biosensors & Bioelectronics,* vol. 35, pp. 200-205, May 2012.

[91] T. C. Sudhof, "The synaptic vesicle cycle," *Annu Rev Neurosci,* vol. 27, pp. 509-47, 2004.

[92] B. Katz, *The release of neural transmitter substances*. Springfield, Ill.: Thomas, 1969.

[93] T. C. Sudhof and J. Rizo, "Synaptic vesicle exocytosis," *Cold Spring Harb Perspect Biol,* vol. 3, Dec 2011.

[94] J. E. Heuser and T. S. Reese, "EVIDENCE FOR RECYCLING OF SYNAPTIC VESICLE MEMBRANE DURING TRANSMITTER RELEASE AT THE FROG NEUROMUSCULAR JUNCTION," *The Journal of Cell Biology,* vol. 57, pp. 315-344, 1973.

[95] Q. Zhang, Y. Li, and R. W. Tsien, "The Dynamic Control of Kiss-And-Run and Vesicular Reuse Probed with Single Nanoparticles," *Science,* vol. 323, pp. 1448-1453, March 13, 2009 2009.

[96] L. He and L. G. Wu, "The debate on the kiss-and-run fusion at synapses," *Trends Neurosci,* vol. 30, pp. 447-55, Sep 2007.

[97] P. D. Robbins and A. E. Morelli, "Regulation of immune responses by extracellular vesicles," *Nat Rev Immunol,* vol. 14, pp. 195-208, Mar 2014.

[98] S. Wernersson and G. Pejler, "Mast cell secretory granules: armed for battle," *Nat Rev Immunol,* vol. 14, pp. 478-94, Jul 2014.

[99] K. D. Stone, C. Prussin, and D. D. Metcalfe, "IgE, Mast Cells, Basophils, and Eosinophils," *The Journal of allergy and clinical immunology,* vol. 125, pp. S73-S80, 2010.

[100] J. P. Kinet, "The high-affinity IgE receptor (Fc epsilon RI): From physiology to pathology," *Annual Review of Immunology,* vol. 17, pp. 931-972, 1999.

[101] J. K. Angleson and W. J. Betz, "Monitoring secretion in real time: Capacitance, amperometry and fluorescence compared," *Trends in Neurosciences,* vol. 20, pp. 281-287, Jul 1997.

[102] W. J. Tyler and V. N. Murthy, "Synaptic vesicles," *Curr Biol,* vol. 14, pp. R294-7, Apr 20 2004.

[103] R. E. Thompson, M. Lindau, and W. W. Webb, "Robust, high-resolution, whole cell patch-clamp capacitance measurements using square wave stimulation," *Biophysical Journal,* vol. 81, pp. 937-948, 2001.

[104] B. Rituper, A. Gucek, J. Jorgacevski, A. Flasker, M. Kreft, and R. Zorec, "High-resolution membrane capacitance measurements for the study of exocytosis and endocytosis," *Nat Protoc,* vol. 8, pp. 1169-83, Jun 2013.

[105] W.-Z. Wu, W.-H. Huang, W. Wang, Z.-L. Wang, J.-K. Cheng, T. Xu, *et al.*, "Monitoring Dopamine Release from Single Living Vesicles with Nanoelectrodes," *Journal of the American Chemical Society,* vol. 127, pp. 8914-8915, 2005/06/01 2005.

[106] C. T. Wang, R. Grishanin, C. A. Earles, P. Y. Chang, T. F. Martin, E. R. Chapman, *et al.*, "Synaptotagmin modulation of fusion pore kinetics in regulated exocytosis of dense-core vesicles," *Science,* vol. 294, pp. 1111-5, Nov 2 2001.

[107] B. Zhang, M. Heien, M. F. Santillo, L. Mellander, and A. G. Ewing, "Temporal Resolution in Electrochemical Imaging on Single PC12 Cells Using Amperometry and Voltammetry at Microelectrode Arrays," *Analytical Chemistry,* vol. 83, pp. 571-577, Jan 2011.

[108] K. L. Adams, B. K. Jena, S. J. Percival, and B. Zhang, "Highly sensitive detection of exocytotic dopamine release using a gold-nanoparticle-network microelectrode," *Anal Chem,* vol. 83, pp. 920-7, Feb 1 2011.

[109] W. J. Betz, F. Mao, and C. B. Smith, "Imaging exocytosis and endocytosis," *Current Opinion in Neurobiology,* vol. 6, pp. 365-371, Jun 1996.

[110] Y. Kawasaki, T. Saitoh, T. Okabe, K. Kumakura, and M. Oharaimaizumi, "VISUALIZATION OF EXOCYTOTIC SECRETORY PROCESSES OF MAST-CELLS BY FLUORESCENCE TECHNIQUES," *Biochimica Et Biophysica Acta*, vol. 1067, pp. 71-80, Aug 5 1991.

[111] R. M. Williams and W. W. Webb, "Single granule pH cycling in antigen-induced mast cell secretion," *Journal of Cell Science*, vol. 113, pp. 3839-3850, 2000.

[112] R. Cohen, K. Corwith, D. Holowka, and B. Baird, "Spatiotemporal resolution of mast cell granule exocytosis reveals correlation with Ca2+ wave initiation," *J Cell Sci*, vol. 125, pp. 2986-94, Jun 15 2012.

[113] D. Zenisek, J. A. Steyer, and W. Almers, "Transport, capture and exocytosis of single synaptic vesicles at active zones," *Nature*, vol. 406, pp. 849-854, 08/24/print 2000.

[114] M. A. Gaffield and W. J. Betz, "Imaging synaptic vesicle exocytosis and endocytosis with FM dyes," *Nat Protoc*, vol. 1, pp. 2916-21, 2006.

[115] D. F. Steinbrenner and J. C. Behrends, "Serotonin-Loading Increases Granule Size and Prolongs Fusion Pore Formation in Two Types of Rat Basophilic Leukaemia (RBL) Mast Cell Analogs," *Biophysical Journal*, vol. 104, pp. 620a-621a.

[116] G. Alvarez De Toledo, R. Fernandez-Chacon, and J. M. Fernandez, "Release of secretory products during transient vesicle fusion," *Nature (London)*, vol. 363, pp. 554-558, 1993 1993.

[117] C. Amatore, Y. Bouret, E. R. Travis, and R. M. Wightman, "Interplay between membrane dynamics, diffusion and swelling pressure governs individual vesicular exocytotic events during release of adrenaline by chromaffin cells," *Biochimie*, vol. 82, pp. 481-496, May 2000.

[118] C. Amatore, A. I. Oleinick, and I. Svir, "Reconstruction of aperture functions during full fusion in vesicular exocytosis of neurotransmitters," *Chemphyschem*, vol. 11, pp. 159-74, Jan 18 2010.

[119] A. Anantharam, D. Axelrod, and R. W. Holz, "Real-time imaging of plasma membrane deformations reveals pre-fusion membrane curvature changes and a role for dynamin in the regulation of fusion pore expansion," *J Neurochem*, vol. 122, pp. 661-71, Aug 2012.

[120] C. M. Marchini-Alves, L. M. Nicoletti, V. M. Mazucato, L. B. de Souza, T. Hitomi, P. Alves Cde, *et al.*, "Phospholipase D2: a pivotal player modulating RBL-2H3 mast cell structure," *J Histochem Cytochem*, vol. 60, pp. 386-96, May 2012.